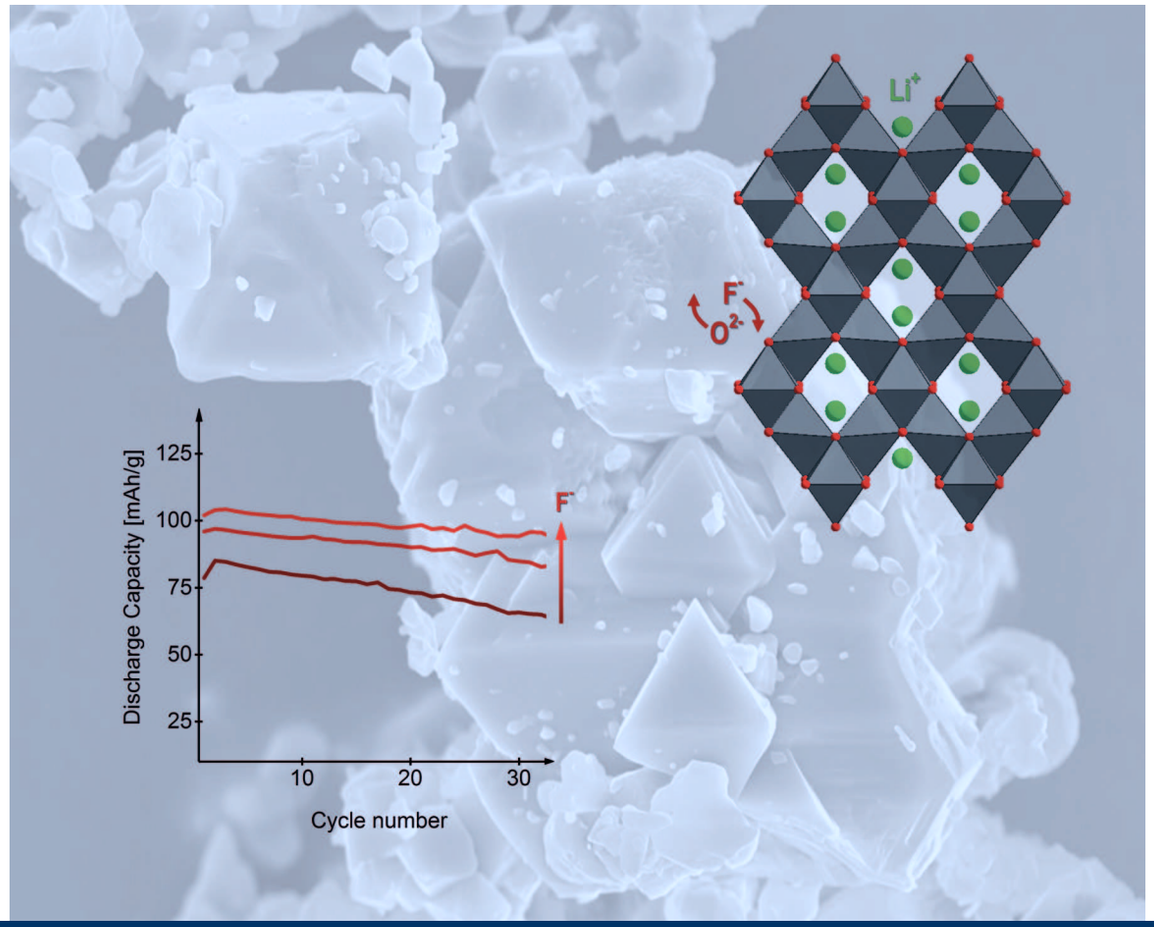

Synthesis and Analysis of Spinel Cathode Materials for High Voltage Solid-State Lithium Batteries

Anna Windmüller

Energie & Umwelt / Energy & Environment
Band / Volume 458
ISBN 978-3-95806-396-9

Mitglied der Helmholtz-Gemeinschaft

JÜLICH
Forschungszentrum

Schriften des Forschungszentrums Jülich
Reihe Energie & Umwelt / Energy & Environment Band / Volume 458

Forschungszentrum Jülich GmbH
Institut für Energie- und Klimaforschung
Werkstoffsynthese und Herstellungsverfahren (IEK-1)

Synthesis and Analysis of Spinel Cathode Materials for High Voltage Solid-State Lithium Batteries

Anna Windmüller

Schriften des Forschungszentrums Jülich
Reihe Energie & Umwelt / Energy & Environment Band / Volume 458

ISSN 1866-1793 ISBN 978-3-95806-396-9

Bibliografische Information der Deutschen Nationalbibliothek.
Die Deutsche Nationalbibliothek verzeichnet diese Publikation in der Deutschen Nationalbibliografie; detaillierte Bibliografische Daten sind im Internet über http://dnb.d-nb.de abrufbar.

Herausgeber und Vertrieb: Forschungszentrum Jülich GmbH
Zentralbibliothek, Verlag
52425 Jülich
Tel.: +49 2461 61-5368
Fax: +49 2461 61-6103
zb-publikation@fz-juelich.de
www.fz-juelich.de/zb

Umschlaggestaltung: Grafische Medien, Forschungszentrum Jülich GmbH

Druck: Grafische Medien, Forschungszentrum Jülich GmbH

Schriften des Forschungszentrums Jülich
Reihe Energie & Umwelt / Energy & Environment, Band / Volume 458

D 82 (Diss., RWTH Aachen University, 2018)

ISSN 1866-1793
ISBN 978-3-95806-396-9

Vollständig frei verfügbar über das Publikationsportal des Forschungszentrums Jülich (JuSER) unter www.fz-juelich.de/zb/openaccess.

Content

List of abbreviations iv

1 Introduction and objectives 1

2 Literature overview 6

2.1 Lithium-ion batteries and cathode materials 6

2.2 Spinels: structure and properties 7

2.3 $LiMn_2O_4$ spinel and the discovery of high voltage spinel cathodes 10

2.3.1 $LiNi_{0.5}Mn_{1.5}O_4$ high voltage spinel 12

2.3.2 $LiFe_{0.5}Mn_{1.5}O_4$ high voltage spinel 14

2.3.3 $LiCoMnO_4$ high voltage spinel 15

2.4 Solid-state lithium batteries 16

3 Materials and methods 19

3.1 Synthesis and processing 19

3.1.1 Pechini synthesis 19

3.1.2 Solid-state reaction synthesis 20

3.1.3 Mixtures of spinels and solid electrolytes 21

3.1.4 Processing of $LiCoMnO_4$ pellets as cathodes 22

3.2 Materials characterization 23

3.2.1 X-ray powder diffraction 23

3.2.2 Scanning electron microscopy 24

3.2.3 Chemical analysis 24

3.2.4 Thermal analysis 26

3.2.5 In-situ high temperature X-ray powder diffraction 26

3.2.6 Raman spectroscopy 27

3.2.7 Neutron and synchrotron powder diffraction 28

3.3 Electrochemical characterization 30

4 Experimental results.....31

4.1 Part I: Synthesis and analysis of $LiNi_{0.5}Mn_{1.5}O_4$, $LiFe_{0.5}Mn_{1.5}O_4$, $LiCoMnO_4$ 31

4.1.1 Structural and microstructural properties 31

4.1.2 Electrochemical activity.....37

4.1.3 Thermal reactions 39

4.2 Part II: Compatibility of $LiNi_{0.5}Mn_{1.5}O_4$, $LiFe_{0.5}Mn_{1.5}O_4$ and $LiCoMnO_4$ with solid electrolytes.....41

4.2.1 Thermal reactions of spinels in mixture with electrolytes 41

4.2.2 Co-sintering of spinels and solid electrolytes at various temperatures43

4.2.3 Phase evolution as a function of temperature.....48

4.3 Part III: Densification of $LiCoMnO_4$ with LiF additive 51

4.3.1 Densification behavior and phase content 51

4.3.2 Identifying optimal sintering conditions and resulting microstructure ..53

4.3.3 Sample chemistry as a function of temperature.....57

4.3.4 In-situ phase evolution as a function of temperature.....59

4.3.5 Electrochemical activity.....61

4.4 Part IV: Synthesis and characterization of fluorinated $LiCoMnO_4$.....63

4.4.1 Structure and chemistry of fluorinated $LiCoMnO_4$.....63

4.4.2 Crystallography and crystal chemistry of fluorinated $LiCoMnO_4$ 65

4.4.3 Microstructural properties 75

4.4.4 Electrochemical properties.....76

5 Discussion.....86

5.1 Part I: $LiNi_{0.5}Mn_{1.5}O_4$, $LiFe_{0.5}Mn_{1.5}O_4$ and $LiCoMnO_4$ single materials properties 86

5.1.1 Structural and electrochemical aspects 86

5.1.2 Thermal decomposition behavior.....89

5.2 Part II: Compatibility of $LiNi_{0.5}Mn_{1.5}O_4$, $LiFe_{0.5}Mn_{1.5}O_4$ and $LiCoMnO_4$ with solid electrolytes 91

5.3 Part III: Densification of $LiCoMnO_4$ with LiF as sintering additive 93

5.4 Part IV: Impact of fluorination on properties of $LiCoMnO_4$ 98

5.4.1 Chemistry, structure and crystal chemistry of $LiCoMnO_{4-\delta}F_x$ 98

5.4.2 Local chemical order 101

5.4.3 Microstructure and electrochemical performance 102

6 Summary and outlook 108

Acknowledgement 112

List of figures 115

List of tables 121

References 122

Abstract 138

Kurzfassung 140

List of abbreviations

CHDC	Galvanostatic charge-discharge measurement
CV	Cyclic voltammetry
DEC	Diethyl carbonate
DMC	Dimethyl carbonate
DTA/TG	Differential thermo-analysis and thermogravimetry
EC	Ethylene carbonate
ICP-OES	Inductively coupled plasma optical emission spectroscopy
ICSD	Inorganic crystal structure database
IFA	Inert gas fusion analysis
LATP	$Li_{1.5}Al_{0.5}Ti_{1.5}(PO_4)_3$
LiPON	Lithium phosphorus oxynitride
LLZ	$Li_{6.6}La_3Zr_{1.6}Ta_{0.4}O_{12}$
NRA	Nuclear reaction analysis
PDF	Powder diffraction file
PVdF	Polyvinylidene fluoride
SEM	Scanning electron microscopy
XRD	X-ray Powder Diffraction

1 Introduction and objectives

One of the most challenging issues in our modern society is the problem of energy storage. Energy storage systems are needed for the storage of energy produced by wind or solar energies especially, which are essential to reduce the environmental impact from the utilization of fossil fuels, such as air pollution and global warming. Furthermore, the flourishing development of portable systems including smart phones, computers and powered tools demand small and compact energy storage systems to prolong their working hours and to minimize the overall device volume. Similarly, the demand for electric vehicles, for the reduction of petroleum consumption, requires efficient and compact storage systems with high energy densities. Among the energy storage systems, lithium-ion batteries offer the highest energy density and the highest coulombic efficiency. Lithium-ion batteries have been the most popular energy storage system for portable, computing and communication technologies since their commercialization in 1991 [1]. To cope with the demand for electric mobility, researchers in the sectors of academia and industry are working on a further development of the lithium-ion battery technology. However, for practical travelling distances, the electric mobility technologies require even higher energy densities and higher powder densities than achieved by the state of the art battery technologies [2,3].

To increase the overall energy density of a battery, materials scientists focus on the development of new active battery materials that allow for higher energy densities. From an electrochemical point of view, there are two possibilities to improve the energy density of a lithium-ion battery based on the active materials used: a) to develop active materials with a higher specific capacity, which means a higher number of Li-ions for electrochemical insertion and extraction is provided within one gram of active material; and/or b) to develop active materials with a higher operational voltage. While a) usually requires the design of completely new materials [4,5], b) can be achieved by slight modification from already known materials. This modification is achieved by substitution of the electrochemical active cations with other cations that provide higher electrochemical potentials, as is possible within the spinel type cathodes, based on $LiMn_2O_4$ [6,7]. Spinel cathodes, with cobalt or iron substitutions for manganese, allow for redox potentials of up to 5.2 V vs. Li/Li^+,

which is around 30 % higher than the potential of $LiMn_2O_4$ and of commercial cathode materials, such as $LiCoO_2$ [1]. Since the energy density is the integral of the potential over the capacity, the higher potentials lead theoretically to an overall increase in energy density of 30 %, if the capacities are identical (Figure 1.1).

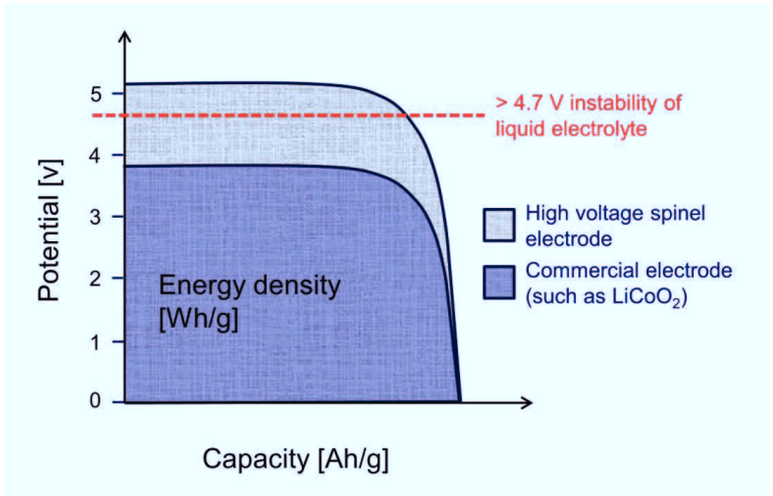

Figure 1.1: Schematic representation of potential, capacity and energy density relations between commercial and high voltage cathode materials in lithium-ion batteries.

Although the spinel cathodes offer promising high redox potentials, these high potentials are the major challenge for the realization of high voltage battery concepts. Generally, the liquid electrolytes used in lithium-ion batteries are organic carbonate-ester solutions, which do not offer the required stability at potentials higher than 4.7 V vs. Li/Li^+ [8,9] (Figure 1.1). The spinel cathodes, with their redox potentials above 4.7 V vs. Li/Li^+, require new types of electrolytes that are stable up to 5.5 V vs. Li/Li^+ so that the battery can be cycled with high coulombic efficiency and long-term stability. One promising solution is to equip the high voltage cathode with a stable solid-state electrolyte ceramic, such as amorphous lithium phosphorus oxynitride (LiPON), which is stable up to 5.5 V vs. Li/Li^+, or garnet structured $Li_7La_3Zr_2O_{12}$, which is stable up to 6 V vs. Li/Li^+, to build up a so called all solid-state battery [10,11].

The integration of a cathode into an all solid-state battery comes along with new requirements to the cathode active material itself. In liquid electrolyte based lithium-ion batteries, powdered cathodes are used to establish an optimized surface area

between the solid active material particles and the liquid electrolyte for optimal lithium-ion transport to the active material and full utilization of the active material itself. In absence of any liquid electrolyte in solid state batteries, the microstructural properties of the cathode need to be adjusted to mimic the conditions of the cathodes of lithium-ion batteries using liquid electrolyte. That is to say, in solid-state batteries lithium-ion diffusion paths for optimal lithium-ion transport to the active material in the cathode need to be provided by a network of solid electrolyte material throughout the cathode layer. This kind of cathode design could be called ‘mixed cathode’, since it consists of both phases, i.e. the active material and a solid electrolyte material. Figure 1.2 illustrates the desired microstructure of a mixed cathode. This kind of microstructural design can be approached by co-sintering of the active material and the solid electrolyte powder at elevated temperatures. However, this processing route requires the chemical compatibility of the two materials at/near the sintering temperature.

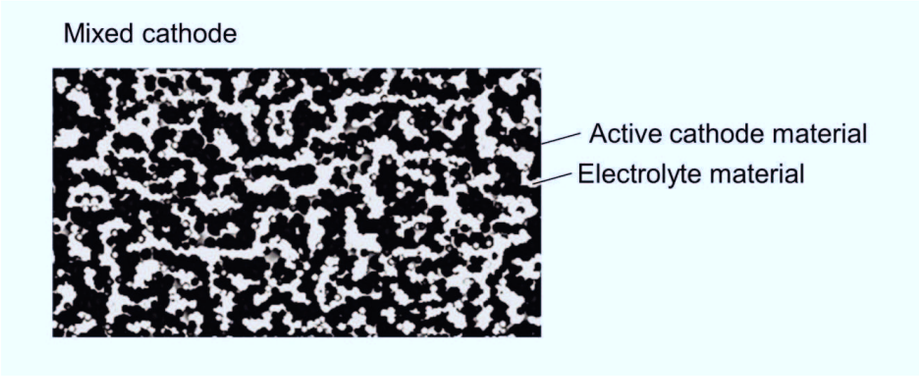

Figure 1.2: Scheme of the desired microstructure for a mixed cathode for solid-state lithium batteries.

While the mixed cathode approach is the first choice to target the fabrication of a solid-state lithium battery, a solid electrolyte, which is chemically compatible to the active material at elevated temperatures, may not be available up to now. Under this situation, a self-supported cathode pellet made from active material only can be used to proof the concept of a high voltage solid-state lithium battery. Since the active material itself only offers partial lithium-ion and electronic conductivity, the self-supported cathode would be chosen as thin as possible, but thick enough to be

self-standing and support an electrolyte which separates the cathode from the anode.

Both approaches, the mixed cathode approach and the self-supported thin cathode approach, would require the sinterability of the active material to high relative densities. In conventional lithium-ion batteries using liquid electrolyte, the electron conductive pathways within the cathode are provided by additional carbon powder in the cathode. Since carbon is a good electronic conductor, it establishes the electronic conducting paths via carbon particles for the active material in the cathode. In a solid-state battery with a mixed cathode or a self-supported thin cathode, as described above, the electronic conducting pathways need to be established by the active material itself, if no extra electronically conductive additive is added. This requires the particles in the cathode to be in close contact with each other, which can be achieved by densification via sintering.

High relative densities are also necessary to gain sufficient volumetric energy densities of the cathode. Furthermore, for satisfactory gravimetric and volumetric energy density of the whole cell, a dense thin-film electrolyte, which separates the anode from the cathode is required. The thinner the solid electrolyte the higher the gravimetric and volumetric energy density of the cell. For the deposition of a thin film electrolyte by thin film methods such as physical vapor deposition, a dense and smooth surface of the cathode as a substrate is an important requirement.

The motivation for this dissertation is to develop spinel materials for high voltage solid-state batteries and their evaluation based on the two concepts given above. The whole dissertation can be subdivided into four parts:

I) The first step is the synthesis and characterization of high voltage spinel cathodes based on $LiMn_2O_4$ spinel with different substitutions of Mn, namely $LiNi_{0.5}Mn_{1.5}O_4$, with a redox centre at 4.7 V vs. Li/Li^+, $LiFe_{0.5}Mn_{1.5}O_4$, with a redox center at 4.0 and 5.1 V vs. Li/Li^+ and $LiCoMnO_4$, with redox centres at 5.0 to 5.2 V vs. Li/Li^+.

II) To prepare solid-state batteries based on a mixed cathode, the chemical compatibilities of the synthesized spinels with two solid electrolytes, $Li_{1.5}Al_{0.5}Ti_{1.5}(PO_4)_3$ (LATP) [12] and $Li_{6.6}La_3Zr_{1.6}Ta_{0.4}O_{12}$ (LLZ) [13], were evaluated to identify possible combinations that are suitable for the pro-

cessing of mixed high voltage cathodes. However, the results showed that none of the combinations provide sufficient chemical stability at the sintering temperatures. Therefore, the approach was changed to using active material only to target the concept of a self-supported cathode.

III) For using only active material to process a self-supported cathode, $LiCoMnO_4$ was chosen, which offers the highest potential among the synthesized materials. Lithium-manganese spinels are known to be unstable at higher temperatures and tend to release lithium and oxygen from their lattice with increasing temperatures [14,15], which usually was found to leave a porous structure after high temperature heat treatment and complicates the densification process. Therefore, LiF was studied as a sintering additive to better densify $LiCoMnO_4$ cathodes.

IV) Using LiF as sintering additive raises the question whether and how fluorination of $LiCoMnO_4$ would impact its electrochemical performance. Therefore, an investigation of fluorinated $LiCoMnO_4$ was carried out. This includes the synthesis of fluorinated $LiCoMnO_4$ powders, as well as their detailed analysis to answer the question if fluorine is incorporated into the spinel lattice and how the fluorine incorporation affects the performance of $LiCoMnO_4$ cathodes.

2 Literature overview

2.1 Lithium-ion batteries and cathode materials

Lithium-ion batteries are secondary electrochemical cells, in which chemical energy is converted into electrical energy during discharging and electrical energy into chemical energy during charging, with charge carriers being lithium-ions and electrons. Lithium-ion batteries consist of two electrodes, which are separated by a separator, and an electrolyte, which penetrates the electrodes and the separator. The electrolyte is electronically insulating but allows for the diffusion of lithium-ions from one electrode to the other. For secondary batteries, anode and cathode are conventionally named after the processes during the discharge process. Hence, during discharge, the negative electrode, where the oxidation takes place, is called anode and the positive electrode, where the oxidation takes place is called cathode. During charging, the reduction takes place in the anode and the oxidation in the cathode. (Figure 2.1). The voltage of the lithium-ion battery results from the potential difference between the anode and the cathode [16,17].

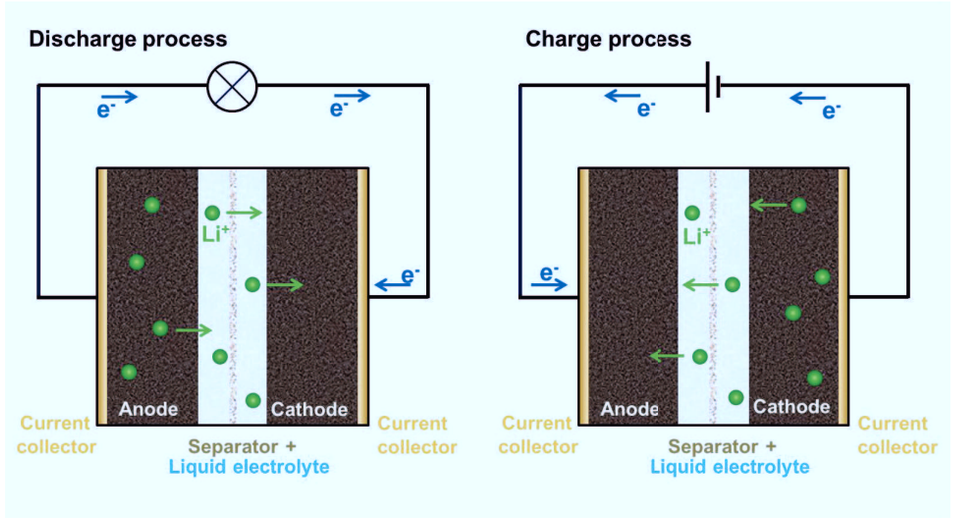

Figure 2.1: Schematic representation of a lithium-ion battery and the processes during discharge and charge.

Lithium-ion batteries were first commercialized by Sony in 1991. The cathode material used was $LiCoO_2$, which has been the most common cathode material ever since [1]. Other common commercial cathode materials are lithium intercalation materials with layered, spinel or olivine structure [18] (Table 2.1). Layered structured cathode materials that are derived from $LiCoO_2$ by substitution of Co by certain elements, such as Ni, Al and Mn, provide an improved specific capacity compared to $LiCoO_2$ [1]. $LiMn_2O_4$ spinel was commercialized by NEC in 1996 for a limited market and offered the highest potential against Li/Li^+ in commercial cells at that time [1,19]. In contrast to the cathode materials with a layered structure, the spinel structure permits three-dimensional diffusion paths for the lithium-ions, which allow for high rate capabilities. Moreover, the spinels provide access to the $Mn^{3+/4+}$ redox couple at around 4.0 V vs. Li/Li^+ and make access to even higher voltages possible by substitution of manganese by high voltage redox couples, such as Ni, Fe or Co [6,7,19,20].

Table 2.1: Properties of commercial lithium-ion batteries [21,22].

Cathode material	Chemistry	Structure type	Potential vs. Li/Li^+ [V]	Spec. Capacity [$mAhg^{-1}$]
Lithium cobalt oxide	$LiCoO_2$	layered	3.9	140
Nickel cobalt aluminum oxide	$LiNi_{0.8}Co_{0.15}Al_{0.05}O_2$	layered	3.8	180-200
Nickel manganese cobalt oxide	$LiNi_{1-x-y}Mn_xCo_yO_2$	layered	3.8	160-170
Lithium manganese oxide	$LiMn_2O_4$	spinel	4.1	100-120
Lithium iron phosphate	$LiFePO_4$	olivine	3.5	150-170

2.2 Spinels: structure and properties

Spinels are metal oxides with the general formula AB_2O_4. They show a large chemical variety with A and B being mono- to tetra- or hexavalent alkali, alkaline earth or transition metal cations. The spinel group materials are named after the mineral spinel, which is a magnesium aluminum oxide, $MgAl_2O_4$ [23].

The group members are isomorphous to the mineral spinel $MgAl_2O_4$ and crystallize in the space group *Fd-3m* [24]. One unit cell contains eight formula units of AB_2O_4. The lattice parameter of the unit cell is 8 to 9 Å large [23]. The *Fd-3m* space group

has 9 Wyckoff positions [25] of which three are occupied in spinel [24]. If the origin of the unit cell chosen is at *-3m*, the *8a* Wyckoff position, at *1/8, 1/8, 1/8,* is a tetrahedrally coordinated cationic site, while *8b* is a tetrahedral vacant site. Similarly, the octahedrally coordinated *16d* site, at *1/2, 1/2, 1/2*, is occupied, while the *16c* site, at *0, 0, 0* is vacant [24,25]. The *32e* Wyckoff position, at *x, x, x,* is an anionic site. In the ideal case of $x = 0.25$, the anion sublattice is cubic closed packed. x depends on the sizes of the tetrahedrally and octahedrally coordinated cations and lies within the range of $x = 0.235$ to $x = 0.275$ [24].

The occupation of the tetrahedral and octahedral sites with A- or B-cations depends on the cationic properties, i.e. their valences and sizes and their octahedral or tetrahedral site preference [26]. This leads to the so called normal and inverse spinel type materials [24]. In normal spinels, the *8a* tetrahedral site is occupied by A-cations and the *16d* octahedral site by B-cations: $A^{8a}[B_2]^{16d}O_4$. In the inverse spinel structure, the *8a* tetrahedral sites are occupied by type B-cations, while the *16d* octahedral site is occupied half by A- and B-cations: $B^{8a}[AB]^{16d}O_4$. Mixing between both structure types is possible, depending on the stoichiometry of the spinel phase [23,24,26].

Both, inverse and normal type spinel materials can be designed as cathodes. However, normal type spinel cathodes are far more popular due to their superior lithium-ion diffusion properties [20]. In normal type spinel cathodes, lithium occupies the *8a* tetrahedral site, while usually manganese and/or another transition metal (M) of the fourth period occupy the octahedral *16d* site. Figure 2.2 visualizes the $Li^{8a}(M,Mn)_2{}^{16d}O_4$ cathode in *Fd-3m* spinel structure. This figure also illustrates the three-dimensional pathways in between the *8a* tetrahedral sites and vacant *16c* octahedral sites through which lithium-ions can be extracted and inserted reversibly in normal type spinel cathodes [27].

During lithium insertion or extraction, charge neutrality is guaranteed by oxidation or reduction of the transition metal ions. Thus, for each inserted lithium-ion, one electron is taken up by a transition metal ion. Conversely, extraction of lithium-ions causes the release of electrons by the transition metal ions. Accordingly, the extraction of one mole lithium-ions from $Li(M,Mn)_2O_4$ yields a theoretical specific capacity of around 145 mAh per gram of $Li(M,Mn)_2O_4$.

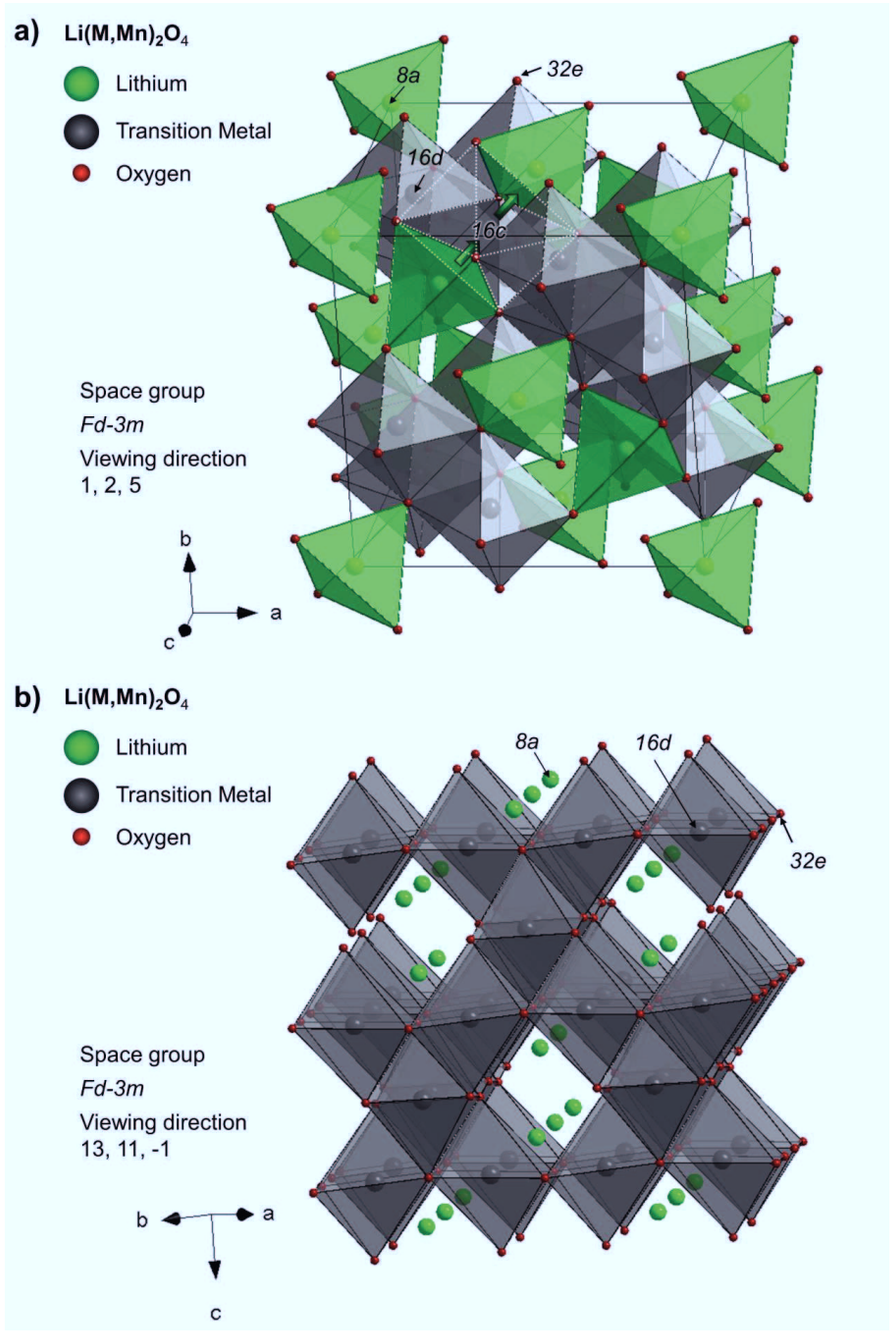

Figure 2.2: Visualization of the $Li(M,Mn)_2O_4$ cathode in *Fd-3m* spinel structure with indication of Wyckoff positions from two different viewing directions: a) 1, 2, 5 viewing direction and representation of the lithium-ion diffusion path (green arrows) in between the *8a* and *16d* sites; b) 13, 11, -1 viewing direction to visualize the three dimensional channels for lithium-ion diffusion.

Lithium-ion diffusion takes place via site hopping along the *8a* and empty *16c* sites. The shared face in between *8a* and *16c* sites is a triangle (Figure 2.2a, green triangle with white dashed lines), spanned by three oxygen atoms. The dimension of this triangle influences the activation energy for the lithium-ion hoping mechanism. Additionally, the activation energy is controlled by electrostatic repulsion of nearest cationic neighbors on tetrahedral and octahedral sites, i.e. lithium and transition metal ions [28]. Hence, lithium-ion diffusion can be controlled by the crystal chemistry of the spinel, such as lattice dimensions and positions of oxygen atoms, as well as valences, ionic radii and bond lengths of cationic species and their distribution and ordering on tetrahedral and octahedral sites [28–31].

2.3 $LiMn_2O_4$ spinel and the discovery of high voltage spinel cathodes

The first known spinel cathode was $LiMn_2O_4$, which was developed by Thackeray *et al*. in 1983 and has been commercialized for a limited market [22,32]. As is typical for the spinel-type materials, $LiMn_2O_4$ crystallizes in the space group *Fd-3m*. Since lithium-ions occupy the *8a* site and manganese ions the *16d* site, the cationic order corresponds to that of the normal spinel, i.e $Li^{8a}[Mn_2]^{16d}O_4$ [33]. $LiMn^{3+}Mn^{4+}O_4$ contains one mole of Mn^{3+} ions, which are electrochemically active at 4.0 V vs. Li/Li^+. The electrochemical reaction for the insertion/extraction of one mole lithium-ions has a theoretical capacity of 148 $mAhg^{-1}$ and can be described as in Equation 2.1:

$$LiMn^{3+}Mn^{4+}O_4 \leftrightarrow Li_{1-x}Mn^{3+}_{1-x}Mn^{4+}_{1+x}O_4 + xLi^+ + xe^- ;\ for\ 0 \le x \le 1 \qquad (2.1)$$

The $LiMn_2O_4$ cathode shows fast capacity fading during cycling, which is a major drawback in the practical use of this material. Reasons for the capacity fading are (i) the Jahn-Teller distortion of the Mn^{3+} ion, which leads to structural transitions during cycling, (ii) manganese dissolution into the liquid electrolyte, and (iii) formation of oxygen vacancies [20,34–36]. To overcome the drawback of the poor cycling stability, cationic substitutions of manganese in $LiMn_2O_4$ have been studied intensively [37–42]. Besides the substitution of manganese by transition metal ions from the fourth period, with a valance equal to or lower than 3+, such as Ti^{3+} [43–45], Cr^{3+} [45–48], Fe^{3+} [45,47,49,50], Co^{3+} [50–54], Ni^{2+} [49,51,55], Cu^{2+} [45,56,57], Zn^{2+} [45,51,58], other non-electrochemical active ions such as, Mg^{2+}

[59,60], B^{3+} [61], and Al^{3+} [44,61,62], were discussed as possible substituents to enhance oxygen stoichiometry and to suppress the Jahn-Teller effect.

During the course of studies on manganese substitutions in $LiMn_2O_4$, it was found that transition metal substituents, such as Cr^{3+} [43,46–48,63,64], Fe^{3+} [45,47,49,64–66], Co^{3+} [6,47,53,61,62,64,67,68], Ni^{2+} [69–72] or Cu^{2+} [56,57] lead to additional redox activity above 4.5 V vs. Li/Li^+. This discovery gave rise to an intensive materials research for high voltage spinels, which are active around 5 V vs. Li/Li^+ and for which at least 0.5 mol manganese per formula unit of $Li(M,Mn)_2O_4$ is substituted by a high voltage redox couple to give a sufficient capacity in the 5 V range [7,20,73,74].

Table 2.2: Examples of high voltage spinel cathodes as known from literature.

Material	High voltage redox couple	Potential of high voltage redox center vs. Li/Li^+ [V]	References
$LiNi_{0.5}Mn_{1.5}O_4$	$Ni^{2+/4+}$	4.7	[6,55,71,75,76]
$LiCr_{0.5}Mn_{1.5}O_4$	$Cr^{3+/4+}$	4.8	[6,48,63]
$LiCrMnO_4$	$Cr^{3+/4+}$	4.8	[6,43,45,48]
$LiCu_{0.5}Mn_{1.5}O_4$	$Cu^{2+/3+}$	4.9	[6,47,57]
$LiFe_{0.5}Mn_{1.5}O_4$	$Fe^{3+/4+}$	5.1	[6,45,64,65]
$LiCo_{0.5}Mn_{1.5}O_4$	$Co^{3+/4+}$	5.2	[6,45,53,67]
$LiCoMnO_4$	$Co^{3+/4+}$	5.2	[6,68,77]

Table 2.2 lists examples of high voltage spinel cathodes $Li(M,Mn)_2O_4$, with M = Ni, Cr, Cu, Fe and Co. The substitution of Mn by one of these transition metal ions does not compromise the spinel structure and the conditions for lithium-ion diffusion through the *8a-16c* channels are maintained, as predicted by theory [78]. However, the electronic properties of the material are modified significantly and cause the additional activity in the high voltage range, above 4.5 V vs. Li/Li^+ [7,78]. The unique electronic structure of high voltage spinels becomes obvious in comparing the $LiCoO_2$ and the $LiCo_xMn_{1-x}O_4$ cathodes. Both cathodes host the redox couple $Co^{3+/4+}$. In $LiCoO_2$ this gives rise to an electrochemical activity at 3.9 vs. Li/Li^+ [1], while in $LiCo_xMn_{1-x}O_4$ it gives rise to an activity centered at 5.0 and 5.2 V vs. Li/Li^+ [77]. In both phases, the $Co^{3+/4+}$ ions are coordinated by oxygen atoms in a 6-fold

symmetry and both phases also share a similar cubic closed packed oxygen sublattice [1]. The differences in the redox potentials between $LiCoO_2$ and $LiCo_xMn_{1-x}O_4$ are caused by the neighboring octahedrally coordinated manganese ions in $LiCo_xMn_{1-x}O_4$, which alter the electronic structure and lead to the high redox potential of the high voltage spinels [20,79].

2.3.1 $LiNi_{0.5}Mn_{1.5}O_4$ high voltage spinel

The most popular and most intensively investigated member of the high voltage spinels is $LiNi^{2+}{}_{0.5}Mn^{4+}{}_{1.5}O_4$. The $Ni^{2+/4+}$ redox couple provides a two-electron redox process, enabling the extraction and insertion, respectively, of one mole lithium-ions at 4.7 V vs. Li/Li^+ (Equation 2.2 and 2.3). Since this process remains below 5 V vs. Li/Li^+, $LiNi_{0.5}Mn_{1.5}O_4$ is still applicable with commonly used liquid electrolytes - as they are used with the $LiCoO_2$ cathode - while providing 20 % higher energy density [8,71,76], which is the major reason for its popularity.

$$LiNi^{2+}_{0.5}Mn^{4+}_{1.5}O_4 \leftrightarrow Li_{1-x}Ni^{2+}_{0.5-x}Ni^{3+}_{x}Mn^{4+}_{1.5}O_4 + xLi^+ + xe^- \text{ ; for } 0 \leq x \leq 0.5 \quad (2.2)$$

$$Li_{0.5}Ni^{3+}_{0.5}Mn^{4+}_{1.5}O_4 \leftrightarrow Li_{1-x}Ni^{3+}_{1-x}Ni^{4+}_{x-0.5}Mn^{4+}_{1.5}O_4 + xLi^+ + xe^- \text{ ; for } 0.5 \leq x \leq 1 \quad (2.3)$$

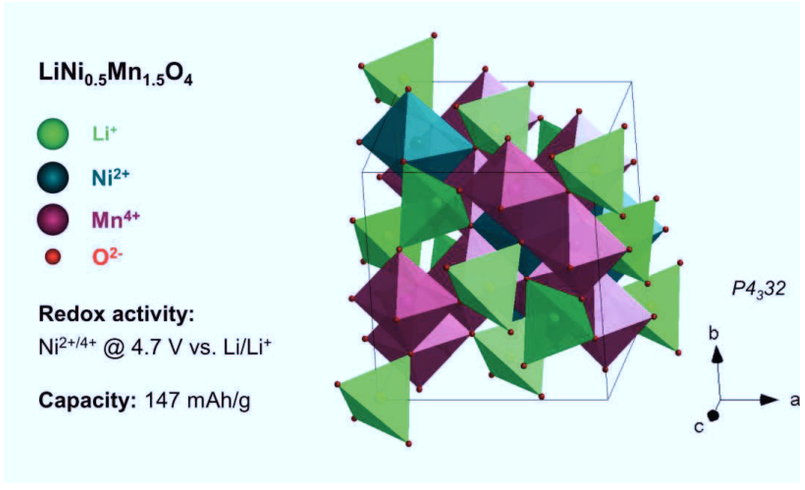

Figure 2.3: Properties of the $LiNi_{0.5}Mn_{1.5}O_4$ high voltage cathode.

Stoichiometric $LiNi_{0.5}Mn_{1.5}O_4$ crystallizes in space group *$P4_332$* (Figure 2.3), which is a superstructure of the *Fd-3m* spinel structure and can be distinguished from *Fd-3m* in X-ray diffraction by the appearance of weak superstructure reflections

belonging to the primitive superstructure cell [80]. The superstructure is caused by long range ordering of Ni^{2+} and Mn^{4+} on the octahedral sites [81]. If Mn^{4+} is partially reduced to Mn^{3+}, due to oxygen loss during synthesis at temperatures higher than 700 °C, the cation order at octahedral sites breaks down and the cation order becomes statistical. Accordingly, non-stoichiometric $LiNi_{0.5}Mn_{1.5}O_{4-\delta}$, also called “disordered spinel”, crystallizes in the *Fd-3m* structure [81,82]. Although the occurrence of Mn^{3+} in non-stoichiometric $LiNi_{0.5}Mn_{1.5}O_{4-\delta}$ lowers the operational voltage, the performance of non-stoichiometric $LiNi_{0.5}Mn_{1.5}O_{4-\delta}$ is improved with respect to rate capability and cycling stability compared to stochiometric $LiNi_{0.5}Mn_{1.5}O_4$. This is most likely an effect of improved lithium-ion diffusion paths in the ordered structure. [28,76].

The theoretical specific capacity of $LiNi_{0.5}Mn_{1.5}O_4$ is 147 $mAhg^{-1}$. Experimentally, discharge capacities of 130 to 140 $mAhg^{-1}$ have been found [71,72,76]. Furthermore, for practical use, the $LiNi_{0.5}Mn_{1.5}O_4$ cathode lacks the required cycling stability - especially at high rates. The degradation is not fully understood but is most likely a combination of structural transformations during cycling, Mn dissolution and/or electrode-electrolyte interactions [72,76,83]. The further improvement of the $LiNi_{0.5}Mn_{1.5}O_4$ properties by optimizing the synthesis routes and by doping is the motivation of various studies [72,80,84,85].

Recent studies showed that fluorination has a positive effect on the cycling stability of $LiNi_{0.5}Mn_{1.5}O_4$ [86–91], due to a stabilization of the spinel lattice [92,93]. It was also shown that discharge capacities were improved by controlled fluorination of around 0.1 mol fluorine per $LiNi_{0.5}Mn_{1.5}O_4$ formula unit [86,89]. Fluorination was usually carried out by post-synthesis at lower temperature using NH_4HF_2 [88,92,94] or fluorine-enriched atmospheres [90]. High-temperature fluorination at 800 °C was reported to be unsuccessful for lithium manganese spinels, because fluorine evaporates from the structure at this temperature [95,96]. Nevertheless, studies of fluorinated $LiNi_{0.5}Mn_{1.5}O_4$ synthesized at 700 °C to 900 °C were also reported, which displayed a positive impact of fluorination on the electrochemical properties of $LiNi_{0.5}Mn_{1.5}O_4$ [86,89,91,97].

2.3.2 $LiFe_{0.5}Mn_{1.5}O_4$ high voltage spinel

$LiFe_{0.5}Mn_{1.5}O_4$ belongs to the group of high voltage spinels generally written as $LiM^{3+}{}_{0.5}Mn^{3+}{}_{0.5}Mn^{4+}O_4$. Besides M = Fe, high voltage activities have been reported for M = Co or Cr [6,7,20] (Table 2.2). The reaction of $Cr^{3+/4+}$, $Fe^{3+/4+}$ or $Co^{3+/4+}$ takes place between 4.8, 5.1 and 5.2 V vs. Li/Li^+, respectively, in a one-electron redox process. $LiM^{3+}{}_{0.5}Mn^{3+}{}_{0.5}Mn^{4+}O_4$ contains 0.5 mol of the high-voltage redox couple. Accordingly, for the extraction of one mole of lithium-ions, only half of the theoretical capacity is available in the high voltage range, whereas the other half is available at 4.0 V vs. Li/Li^+ due to the $Mn^{3+/4+}$ reaction (Equation 2.4 and 2.5). Therefore, the capacity improvement in comparison to $LiCoO_2$ is only 15 %.

$$LiM^{3+}_{0.5}Mn^{3+}_{0.5}Mn^{4+}O_4 \leftrightarrow Li_{1-x}M^{3+}_{0.5}Mn^{3+}_{0.5-x}Mn^{4+}_{1+x}O_4 + xLi^+ + xe^- ;\ for\ 0 \le x \le 0.5 \qquad (2.4)$$

$$Li_{0.5}M^{3+}_{0.5}Mn^{4+}_{1.5}O_4 \leftrightarrow Li_{1-x}M^{3+}_{1-x}M^{4+}_{x-0.5}Mn^{4+}_{1.5}O_4 + xLi^+ + xe^- ;\ for\ 0.5 \le x \le 1 \qquad (2.5)$$

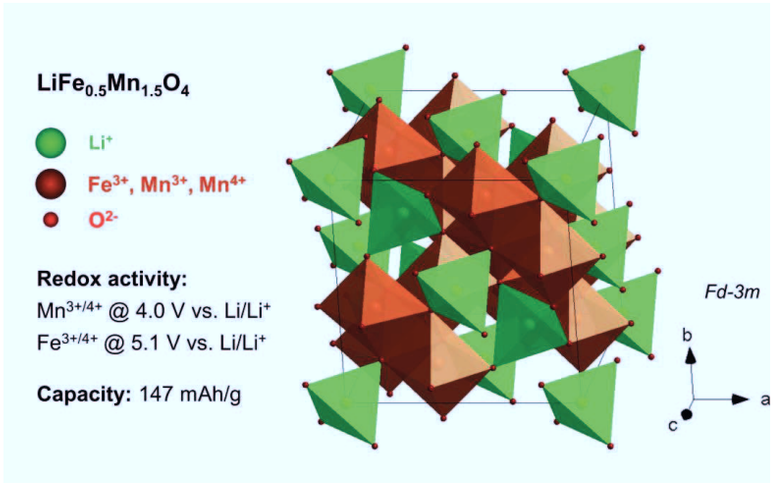

Figure 2.4: Properties of the $LiFe_{0.5}Mn_{1.5}O_4$ high voltage cathode.

Among the $LiM^{3+}{}_{0.5}Mn^{3+}{}_{0.5}Mn^{4+}O_4$ cathodes, $LiFe_{0.5}Mn_{1.5}O_4$ (Figure 2.4) displays the most promising behavior and its raw materials are cheaper and less toxic than for M = Co, Cr or Ni [45,65,98]. The theoretical capacity of $LiFe_{0.5}Mn_{1.5}O_4$ is 148 $mAhg^{-1}$, of which only 74 $mAhg^{-1}$ are available at 5.1 V vs. Li/Li^+. Studies, which aimed to increase the capacity in the high voltage region by further substitution of Fe^{3+} for Mn^{3+} found that the electrochemical activity of $LiFe_xMn_{1-x}O_4$ breaks down for $x > 0.5$. For $x = 1$, where the full capacity should be gained in the high voltage

region theoretically, no electrochemical activity can be actually measured [64]. The reason for this behavior is the electronic structure of the Fe^{3+} ion. Fe^{3+} has no site preference for the octahedral coordination, which is why for $x > 0.5$ the spinel becomes partially inverse [26,64], i.e. Fe-ions start to occupy the tetrahedral *8a* site. The occupation of the tetrahedral site by Fe-ions and displacement of Li-ions to the octahedral *16d* site causes a breakdown of the electrochemical activity for $x > 0.5$ since *8a-16c* channels are blocked and lithium-ion diffusion is suppressed. For $x = 1$, the *8a* sites are occupied by Fe-ions completely, thus Li-ion diffusion through *8a-16c* channels is impossible.

2.3.3 $LiCoMnO_4$ high voltage spinel

$LiCo^{3+}Mn^{4+}O_4$ (Figure 2.5) belongs to the group of $LiM^{3+}Mn^{4+}O_4$ high voltage spinels, which provide the full capacity for the extraction of one mole of lithium-ions at the potential of the $M^{3+/4+}$ redox couple. The $Co^{3+/4+}$ redox couple activity is centered at 5 and 5.2 V vs. Li/Li^+ (Equation 2.6) [68]. $LiCoMnO_4$ is the member of the high voltage spinels with the highest energy density (Table 2.2). Its energy density is 10 % higher than that of the popular $LiNi_{0.5}Mn_{1.5}O_4$ spinel and around 25 % higher than that of the conventional $LiCoO_2$ cathode [6,99].

$$LiCo^{3+}Mn^{4+}O_4 \leftrightarrow Li_{1-x}Co^{3+}_{1-x}Co^{4+}_{x}Mn^{4+}O_4 + xLi^+ + xe^- \text{ ; for } 0 \le x \le 1 \quad (2.6)$$

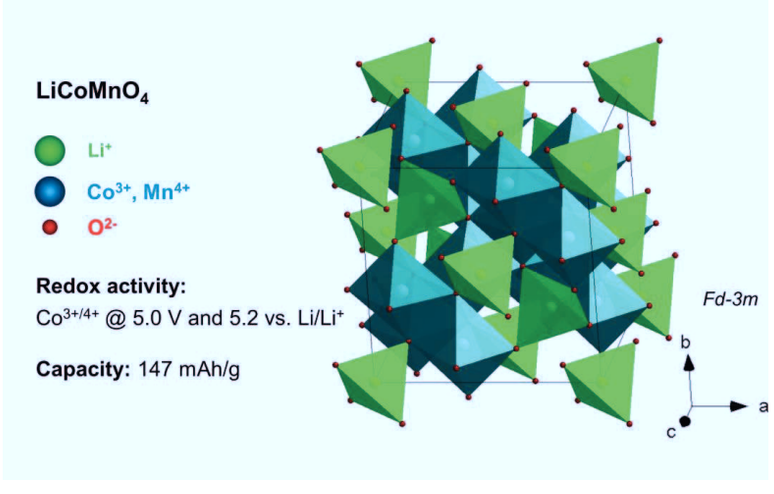

Figure 2.5. Properties of the $LiCoMnO_4$ high voltage cathode.

$LiCoMnO_4$ often contains a certain amount of Mn^{3+} ions inside its lattice, depending on the synthesis conditions. The most common explanation is that the elevated temperatures during synthesis cause oxygen loss from the spinel lattice, which is compensated by the reduction of Mn^{4+} to Mn^{3+} [15]. Mn^{3+} formation due to oxygen loss was reported to start at around 600 °C [100]. Attempts to compensate for oxygen loss by performing the synthesis in oxygen-enriched atmospheres or even pure oxygen failed to produce oxygen-stoichiometric and Mn^{3+}-free $LiCoMnO_4$ [15]. Therefore, $LiCoMnO_4$ is known to always be present in the form of an oxygen non-stoichiometric, Mn^{3+}-containing compound, if synthesized by wet-chemical or solid-state routes.

Additionally, $LiCoMnO_4$ is often reported to coexist with a Li_2MnO_3 secondary phase [15,100–102]. It is known that Li_2MnO_3 forms due to a disproportionation reaction subsequent to the loss of oxygen from $LiCoMnO_4$ [14,100,103]. It was shown that the formation of Li_2MnO_3 can be suppressed by using oxygen-enriched synthesis atmospheres [15,100] and/or by using wet-chemical synthesis routes where lower synthesis temperatures are possible [104].

Cycling of $LiCoMnO_4$ cathodes was shown to result in very low discharge capacities. In fact, the initial discharge capacities for cycling in the 5 V region hardly exceed 75 % of the theoretical capacity in liquid electrolyte cells [50,53,102,104–106] and fast capacity fading was reported (> 20 % after 20 cycles) [50,105], leading to a very low cycling stability of $LiCoMnO_4$ cathodes. One reason for the low capacity and cycling stability is the incompatibility with the liquid electrolyte in the high voltage region. Therefore, the most challenging task for research is to combine the $LiCoMnO_4$ cathode with a suitable electrolyte, which allows for an optimal performance in the high voltage region. A promising solution are ceramic electrolytes with a wider electrochemical stability window [107,108], to build a solid state battery [109,110].

2.4 Solid-state lithium batteries

Solid-state batteries are based on the same electrochemical principle than the batteries with liquid electrolytes, as introduced in section 2.1. Their basic architecture of cathode, electrolyte and anode remains the same. In solid-state lithium batteries, the liquid electrolyte and separator are replaced by a dense ceramic, which con-

ducts lithium-ions but is an electric insulator and separates the anode from the cathode (Figure 2.6).

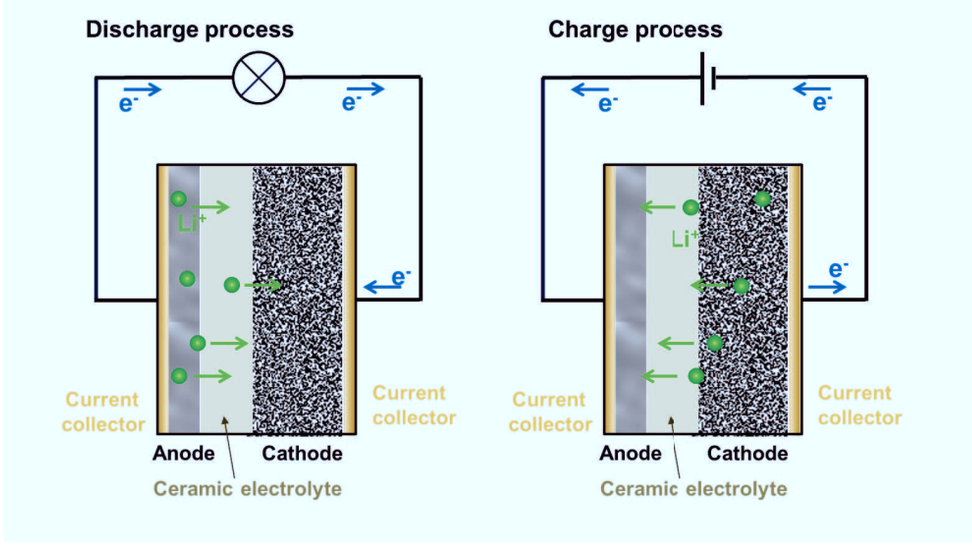

Figure 2.6: Schematic representation of a solid-state lithium battery and the processes during discharge and charge.

The advantages of solid-state lithium batteries compared to conventional lithium-ion batteries with liquid electrolyte are a higher intrinsic safety, a wider applicable temperature range and less toxicity - all because of the replacement of the flammable liquid electrolyte by a solid inflammable ceramic [111]. Another advantage is the possibility to design batteries with higher energy densities [111,112]. Higher energy densities can be achieved because ceramic electrolytes, such as the garnet structured LLZ [107,113] and the amorphous LiPON [114], are applicable with metallic lithium as anode [114,115]. Using metallic lithium as the anode improves the gravimetric and volumetric energy density of the battery. Furthermore, higher energy densities can be achieved because ceramic electrolytes, such as LLZ and LiPON exhibit wider electrochemical stability windows than the conventional carbonate ester liquid electrolytes [8,9,114,116]. This offers the opportunity to build up solid-state batteries with high voltage cathodes.

So far, solid-state lithium batteries with high voltage spinels have been developed based on a thin-film approach, using a thin-film high voltage cathode, a thin-film electrolyte and metallic lithium as anode, e.g. $LiNi_{0.5}Mn_{1.5}O_4$/LiPON/Li [110,117],

$LiFe_{0.5}Mn_{1.5}O_4$/LiPON/Li [108] and $LiCoMnO_4$/LiPON/Li [117] as well as $LiCoMnO_4/Li_3PO_4$/Li [118]. This kind of cell design proves the concept of high voltage solid-state batteries and thin-film batteries certainly are of use for special applications. However, the thin-film design lacks the required energy and power density to cope with conventional lithium-ion batteries with liquid electrolyte. For sufficient energy and power densities, thick cathodes with percolating electronic and lithium-ion diffusion paths are required, as was demonstrated for the $LiCoO_2$/LLZ/Li system [109].

.

3 Materials and methods

3.1 Synthesis and processing

3.1.1 Pechini synthesis

The Pechini synthesis is a wet chemical synthesis method for oxide materials based on the principle of complex polymerization, which starts from an initial aqueous solution of organic salts of the essential cations [119]. The Pechini synthesis is widely used if relatively low synthesis temperatures are favored [120–122]. During the Pechini synthesis the initial solution gels under evaporation of solvents and can be further calcined to achieve the desired phases. The stabilization of cations during solvent evaporation is achieved by organic networking agents. The applied starting materials and networking agents in this study (nitrates, citric acid and ethylene glycol) allow for calcination temperatures as low as 650 °C. This temperature is also suitable for the crystallization of typical spinel cathodes, because of the mixing of the reagents at the atomic level.

To synthesize $LiNi_{0.5}Mn_{1.5}O_4$, $LiFe_{0.5}Mn_{1.5}O_4$ and $LiCoMnO_4$ spinels the metal-nitrates $LiNO_3$ (99 %, Sigma Aldrich), $Ni(NO_3)_2{\cdot}6H_2O$ (99 %, Sigma Aldrich), $Fe(NO_3)_3{\cdot}9H_2O$ (98 %, Sigma Aldrich), $Co(NO_3)_2{\cdot}6H_2O$ (99-101 %, Sigma Aldrich), and $Mn(NO_3)_2{\cdot}4H_2O$ (98 %, Sigma Aldrich) were weighed corresponding to the desired stoichiometry of the spinel samples and dissolved in distilled water in a quartz glass beaker. As a next step, citric acid was added to the dilution in a molar ratio of $n_{citric\ acid}/n_{cations} = 2$. The suspensions were stirred until clear solutions were obtained. 440 wt.-% of ethylene glycol (corresponding to the final sample weight) was added to each solution. The solutions were stirred continuously and solvents were evaporated by increasing the temperature slowly to 300 °C. Afterwards, the precursors were calcined and annealed to obtain the desired phases. Figure 3.1 gives an overview of the synthesis steps: The calcination was done in two steps. The first calcination step was completed after 300 °C for 10 h and 650 °C for 5 h in an on the top open furnace. The second calcination step was completed after another 5 h at 650 °C in a muffle furnace. The phase content was analyzed by X-ray Powder Diffraction (XRD). If phase purity was not reached after calcination, the sample was ball milled in ethanol using yttria-stabilized zirconia balls for

homogenization and heat treated again at 650 °C in alumina crucibles. Table 3.1 lists the specific synthesis conditions. The samples are going to be called LNMO_pec, LFMO_pec and LCMO_pec, according to the stoichiometries $LiNi_{0.5}Mn_{1.5}O_4$, $LiFe_{0.5}Mn_{1.5}O_4$ and $LiCoMnO_4$, respectively.

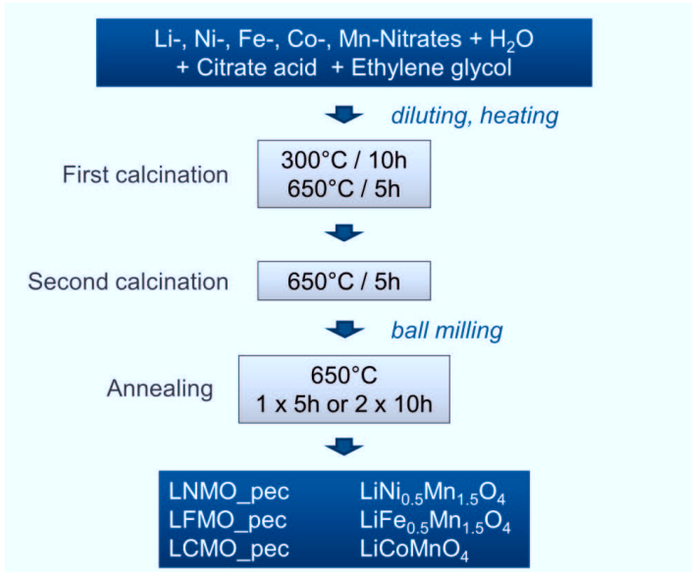

Figure 3.1: Scheme for the Pechini synthesis of $LiNi_{0.5}Mn_{1.5}O_4$, $LiFe_{0.5}Mn_{1.5}O_4$ and $LiCoMnO_4$.

Table 3.1: Synthesis conditions for $LiNi_{0.5}Mn_{1.5}O_4$, $LiFe_{0.5}Mn_{1.5}O_4$ and $LiCoMnO_4$.

Sample name	Nominal stoichiometry	Calcination	Annealing
LNMO_pec	$LiNi_{0.5}Mn_{1.5}O_4$	300 °C 10 h, 2x 650 °C 5h	2x 650 °C 10 h
LMFO_pec	$LiFe_{0.5}Mn_{1.5}O_4$	300 °C 10 h, 2x 650 °C 5h	650 °C 5h
LCMO_pec	$LiCoMnO_4$	300 °C 10 h, 2x 650 °C 5h	650 °C 5h

3.1.2 Solid-state reaction synthesis

To synthesize fluorinated $LiCoMnO_4$ spinels, with the desired stoichiometries $LiCoMnO_4$ (LCMOF00), $LiCoMnO_{3.95}F_{0.05}$ (LCMOF05) and $LiCoMnO_{3.9}F_{0.1}$ (LCMOF10), a two-step solid-state reaction was chosen. $LiOH{\cdot}H_2O$ (AppliChem, 99 %), $MnCO_3$ (Sigma-Aldrich, 99.9 %), Co_3O_4 (Alfa Aesar, 99.7 %) and LiF (Alfa Aesar, 98.5 %) were used as starting materials. The reagents were weighed and mixed in stoichiometric amounts by using an automatic grinder, equipped with

tungsten carbide mortar and pestle (Retsch RM 200) for 30 min at a rotational speed of 100 rpm. 10 mol.-% of excess lithium was added to each batch to compensate any possible lithium loss during the heat treatment processes. The mixed powders were first pressed into pellets for calcination in air at 800 °C for 10 h, followed by another 10 h dwell time at 650 °C in individual Al_2O_3 crucibles, covered with Al_2O_3 lids. After the calcination, the pellets were crushed and ground into powders for another 30 min. The powders were then annealed again at 650 °C for 72 h in air. Finally, about 100 g of powder was obtained for each batch.

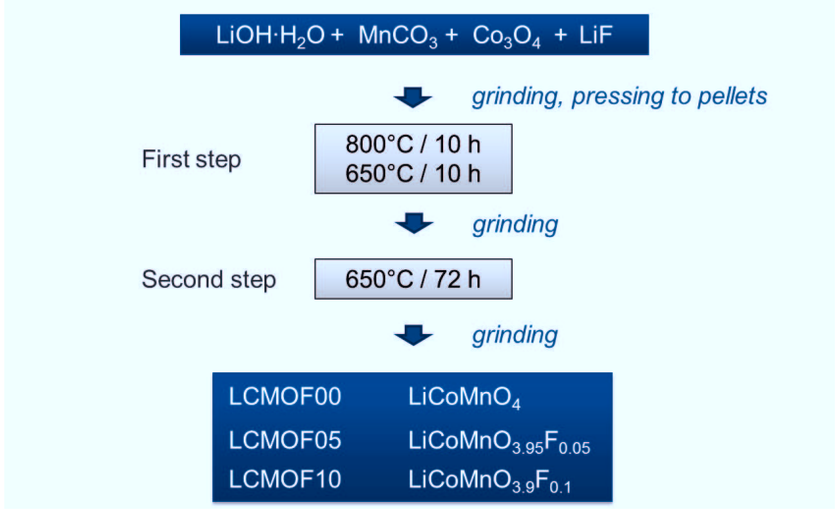

Figure 3.2: Scheme for the solid-state reaction synthesis of LCMOF00, LCMOF05 and LCMOF10.

3.1.3 Mixtures of spinels and solid electrolytes

In order to investigate the compatibility of high voltage spinels and the solid electrolytes LLZ and LATP upon heating, mixtures of spinels and LATP and LLZ respectively, were prepared and subjected to thermal analysis (Figure 3.3). The LATP and LLZ powders were synthesized by sol-gel and solid-state reactions, respectively, described elsewhere [12,13]. The samples LNMO_pec, LFMO_pec or LCMO_pec, as synthesized by Pechini synthesis, were mixed with either LATP or LLZ in a volume ratio of 1:1 using a mortar and pestle, to produce ‘spinel + electrolyte mixtures’, i.e ‘LNMO+LLZ’, ‘LFMO+LLZ’, ‘LCMO+LLZ’, ‘LNMO+LATP’, ‘LFMO+LATP’ and ‘LCMO+LATP’. The spinel + electrolyte mixtures were pressed into pellets with a pressure of 370 MPa using pressing dies with 13 mm diameter. Sintering of pel-

lets was carried out on MgO plates in alumina crucibles at 600, 700 and 800 °C for the spinel+LATP pellets and at 400, 600 and 800 °C for the spinel+LLZ pellets. Dwell time was 1 h each and the heating rate was 5 K/min.

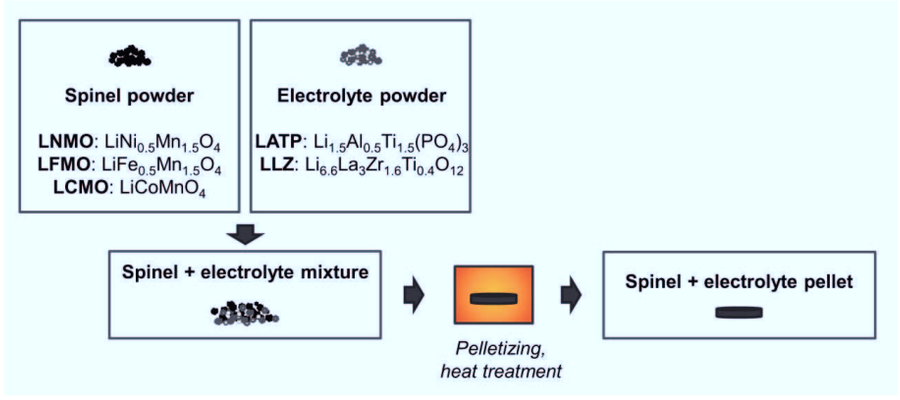

Figure 3.3: Scheme for the preparation of spinel + electrolyte mixtures and spinel + electrolyte pellets.

3.1.4 Processing of $LiCoMnO_4$ pellets as cathodes

To investigate the densification of $LiCoMnO_4$ with and without the sintering additive LiF, LCMO_pec was mixed with different amounts of LiF (0, 0.5, 1 and 1.5 wt.-% LiF) in a mortar, referred to as 'LCMOLiF' samples (Figure 3.4). The LCMOLiF powders were pressed into pellets with a pressure of 370 MPa by using pressing dies with a diameter of 13 mm. LCMOLiF pellets were placed in a powder bed of the same powder sample during sintering. Sintering was carried out in alumina crucibles with lids at different temperatures (700, 800, 850, 900, 1000 °C) in air at different dwell times (Table 3.2). Heating- and cooling rates were 5 K/min.

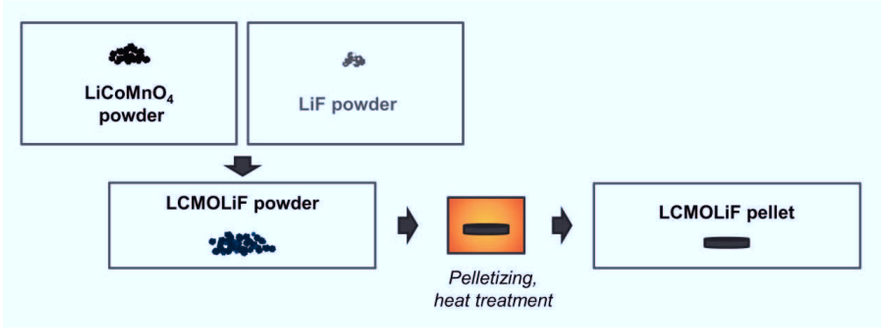

Figure 3.4: Sheme for the preparation of LCMOLiF powders and LCMOLiF pellets.

Table 3.2: Sintering conditions for different LCMOLiF pellets.

Sample	wt.-% LiF	Sintering temperature [°C]	Sintering time [h]
LCMO_800	0	800 + 650	5 + 5
LCMO_1000	0	1000 + 650	2 + 10
LCMOLiF05_800	0.5	800	3
LCMOLiF05_900	0.5	900	2
LCMOLiF05_1000	0.5	1000	2
LCMOLiF10_700	1.0	700	4
LCMOLiF10_800	1.0	800	3
LCMOLiF10_850	1.0	850	2
LCMOLiF10_900	1.0	900	2
LCMOLiF10_1000	1.0	1000	2
LCMOLiF15_900	1.5	900	2
LCMOLiF15_1000	1.5	1000	2

3.2 Materials characterization

3.2.1 X-ray powder diffraction

XRD was carried out using a D4 ENDEAVOR (Bruker AXS) with Cu-K_α radiation for qualitative and quantitative phase analysis. Table 3.3 lists the measurement conditions. The qualitative phase analysis of the diffraction patterns was carried out based on the powder diffraction file (PDF) database and the inorganic crystal structure database (ICSD) using the software package EVA (Bruker axs). Quantitative phase analysis by means of Rietveld refinements was carried out with the software package Topas 4 (Bruker AXS) [123].

Table 3.3: Parameters for the XRD measurement and analysis method.

Sample	Interval [°2θ]	Step width [°2θ]	Accumulation time [s]	Analysis
Pechini powders	10 -140	0.02	2	quantitative
LCMOF powders	10 -140	0.02	2	quantitative
Spinel + electrolyte pellets	10 - 80	0.02	0.75	qualitative
LCMOLiF pellets	10 - 80	0.02	0.75	quantitative

3.2.2 Scanning electron microscopy

Microstructural investigations of the powders was performed by scanning electron microscopy (SEM) using a Zeiss Ultra55 electron microscope with an electron beam accelerating voltage of 15 kV and a back-scattering electron detector. Prior to the SEM measurement the powders were dispersed in ethanol and dried on an aluminum sample holders. Sintered pellets were polished in order to be analyzed by SEM at a HITACHI TM3000 in back scattering mode applying a 15 kV beam accelerating voltage.

3.2.3 Chemical analysis

To quantify cation contents for the LCMOF and LCMOLiF10 samples, inductively coupled plasma optical emission spectroscopy (ICP-OES) was carried out after sample dilution. The samples were diluted in a ratio of 1:20 for measurement with a Thermo Scientific iCAP 7600 dual-view spectrometer. External calibration was performed with standards prepared by the dilution of Merck Certipur certified plasma emission standards with diluted acids. The measurements were performed by using a radio frequency power of 1150 W and a cool gas flow of 12 $l \cdot min^{-1}$, auxiliary gas flow of 0.5 $l \cdot min^{-1}$ and nebulizer gas flow of 0.55 l min^{-1} for 10 s. Each digestion was measured twice and the mean result of three emission lines per element was used for quantification.

Oxygen was measured by inert gas fusion analysis (IFA), which is based on the combustion of a given sample in a graphite crucible in helium atmosphere and determination of the oxygen content by measuring the infrared absorption of CO_2 products. A LECO TCH-600 analyzer (Leco Corporation, USA) with an infrared detection cell was employed to measure the the LCMOF and LCMOLiF10 samples.

Five replicates of approx. 14 mg each were weighed and folded into tin capsules (Leco 501-059), placed in nickel baskets (Leco 502-344) and extracted in graphite crucibles in current control mode for 50 s at 920 A. The instrument was calibrated with 10-25 mg pure ZrO_2 (Alfa Aesar Puratronic) before the measurements were performed.

For fluorine containing samples (LCMOF samples and LCMOF10_700 and LCMOLiF10_1000) the fluorine content was determined by nuclear reaction analysis (NRA). The principle of the NRA method is based on the nuclear reactions between a specimen and a proton beam. The proton beam, which is accelerated to the sample causes a nuclear reaction of the fluorine core and a proton to an instable ^{20}Ne isotope, which decays to the stable ^{16}O isotope and an alpha particle (Figure 3.4). Hence, the determination of fluorine is gained by the analysis of the alpha particle spectrum.

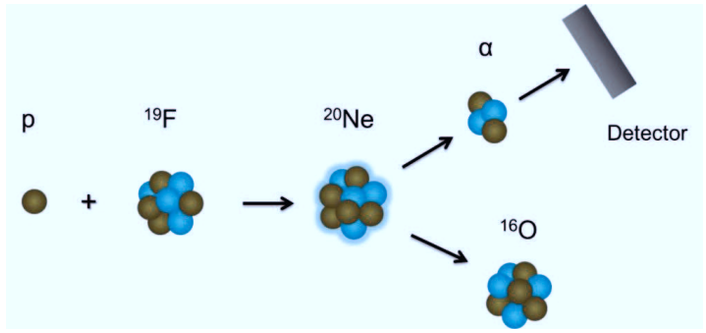

Figure 3.5: Scheme of the $^{19}F(p,\alpha_0)^{16}O$ nuclear reaction.

For the measurements, the LCMOF sample powders were pressed into pellets 13 mm in diameter and 1.5 to 2 mm in thickness, while the LCMOLiF pellets were used as prepared. The pellets were mounted on a sample holder and installed in the proton beam path. A proton beam of 3 mm in diameter was generated from a tandetron accelerator, with a beam energy of 3.24 MeV. A 50 mm^2 passivated implanted planar silicon detector with 300 µm sensitive thickness was installed in backscattering geometry at 165° and at a distance of 100 mm. To guarantee a sufficient signal to noise ratio and resolution, it was ensured that the pile-up contribution (distortion by pulse overlap) was less than 10 % by setting the proton current to ~10 nA. The collected charge was around 100 µC for each measurement. Cross-section data from Ranken *et al*. [124] were employed for fitting the experimental

results by using SIMNRA 6.06 software [125]. The cross sections of fluorine were verified by means of a LiF sample as calibration prior to the measurements.

3.2.4 Thermal analysis

Differential thermo-analysis and thermogravimetry (DTA/TG) measurements were carried out using a NETZSCH STA 449F1 in N_2/O_2 atmosphere (technical air) for all three Pechini powders and the spinel + electrolyte mixtures. These measurements should give insight into chemical reactions, like lithium loss or oxygen release and uptake, and phase transformations during heating and cooling. Dilatometry measurements for the analysis of the sintering behaviour of LCMO_pec and LCMOLiF powder were carried out at a DIL 402C dilatometer (NETZSCH). Samples were prepared by pressing the powders into pellets of 8 mm in diameter and 10 mm in height prior to the dilatometry measurement. The measurement conditions for the samples are listed in Table 3.4.

Table 3.4: Measurement conditions for DTA/TG and Dilatometry measurements of samples.

Sample / Method	Heating interval [°C]	Cooling interval [°C]	Heating/cooling rates
Pechini powders / DTA/TG	25 - 1400	1400 - 25	10 K/min
spinels + LLZ / DTA/TG	25 - 1100	1100 - 25	5 K/min
spinels + LATP / DTA/TG	25 - 1200	1200 - 25	5 K/min
LCMO_pec / Dilatometry	25 - 1100	-	5 K/min
LCMOLiF10 / Dilatometry	25 - 1100	-	5 K/min

3.2.5 In-situ high temperature X-ray powder diffraction

The phase evolution during heating was further investigated by means of in-situ high temperature XRD at an Empyrean R2020 (PANalytical) with Cu-K_α radiation. Samples of LCMO_pec powder and spinel + electrolyte powder mixtures were prepared in alumina front loading sample holders. Another sample of LCMOLiF10 was pelletized. For the pelletizing, the powder was pressed with a pressure of 370 MPa by using a pressing die with a diameter of 20 mm and mounted onto the sample holder. Diffractograms were collected at room temperature before and after each in-situ measurement. The in-situ measurements were performed for isotherms at selected temperatures starting from a minimal temperature to maximal temperature

with a step size of 50 K/step. The heating ramps in between the steps were of 5 K/min, where no scan was performed. The measurement conditions are listed in Table 3.5. The LCMO_pec and LCMOLiF samples were further investigated by Rietveld analysis within the software package Topas 4 (Bruker AXS) [123].

Table 3.5: Measurement conditions for the in-situ high temperature X-ray diffraction.

Sample	Interval [°2θ Cu-K_α]	Temperature interval [°C]	Holding time at each temperature [min]	Number of scans at each temperature
Spinel+electrolyte	13-70	300-1000	38	5
LCMO_pec	15-64	650-950-650	34	5
LCMOLiF10 (pellettised)	15-64	650-950-650	34	5

3.2.6 Raman spectroscopy

Raman spectroscopy is a powerful technique to investigate the local chemical order of a sample by analyzing its Raman active modes under laser excitation, which correspond to characteristic molecular vibrational frequencies. Raman is sensitive to bond length distributions, masses and valences of bonding partners that undergo electronic polarization due to laser excitation. All Pechini powders and all LCMOF powders are subjected to Raman spectroscopy measurements to analyze possible influences of synthesis conditions and fluorination on the local chemical order of the high voltage spinels.

Raman spectroscopy was carried out with a Renishaw inVia Raman microscope using a solid-state 532 nm excitation laser and an 1800 $L \cdot mm^{-1}$ grating. To avoid laser induced phase changes or damage to the samples, the laser power was set to 0.25 mW. To obtain an average spectrum, a line-focus lens was used and a given area of the sample was measured (Table 3.6). The collected scans were averaged, baseline corrected, normalized to their integral in between 340 to 740 cm^{-1}, and fitted in the range from 340 to 740 cm^{-1} by using Pseudo Voigt functions within the WiRE software (Renishaw). To investigate the distribution of chemical components in selected areas of a sample, high-resolution Raman mappings were carried out with a point focus lens and by applying the live track function (an auto focus software solution) within the WiRE software. The spectral acquisition time was cho-

sen for sufficiently high resolution and minimal time per spectra (Table 3.6). Afterwards the collected scans were processed and analyzed within the WiRE software, by using a statistical noise filter and a statistical component analysis algorithm.

Table 3.6: Measurement conditions for micro Raman spectroscopy.

Samples	Investigated area size [µm × µm]	Acquisition time [s]	Step size [µm]	Points per area	Lense type	Objective
Pechni powders	70 × 40	15	1.0	2800	Line-focus	50×
LCMOLiF pellet	60 × 40	2	0.3	2666	Point-focus	50×
LCMOF powders	100 × 60	30	1.0	6000	Line-focus	50×
LCMOF powders	37 × 18	3	0.3	7380	Point-focus	100×

3.2.7 Neutron and synchrotron powder diffraction

To analyze the crystallography of the fluorinated LCMOF05 and LCMOF10 samples in comparison to LCMOF00, all three samples were investigated by joint refinements of neutron and synchrotron diffraction data. The joint refinement approach allows for the determination of lithium and transition metal distributions on tetrahedral and octahedral sites of the spinel phase.

As Figure 3.6 illustrates, X-ray diffraction is based on the elastic interaction with the electrons of an element, which means the intensity of scattered X-rays depends on the electron density of the given element. On the other hand, neutron radiation interacts elastically with the atomic core. Thus, the intensity of a scattered neutron wave depends on the scattering length of the given element (Figure 3.7). Given the high contrast of electron densities for lithium and transition metals for X-rays and cobalt and manganese for neutrons, the cation distribution in the $LiCoMnO_4$ spinel phase can be determined very precisely.

Time-of-flight neutron diffraction data were collected at the POWGEN beamline at the Spallation Neutron Source, Oak Ridge National Laboratory, USA. The samples were dried at 100 °C for five hours and were prepared into Vanadium can sample holders in an Argon filled glove box. Data were collected in a Q-range from 1 to 15 $Å^{-1}$ at 300 K. For synchrotron powder diffraction measurements, the samples were prepared into Kapton cans prior to the measurements. The measurements were

performed at the beamline 11 of the Advanced Photon Source of Argonne National Laboratory at a wavelength of 0.5170 Å in a Q-range from 1 to 10.3 $Å^{-1}$ at 295 K. Data sets from neutron and synchrotron powder diffraction were refined jointly using the GSAS software package [126] in the EXPGUI user interface [127]. The starting model consisted of a $LiCoMnO_4$ phase in *Fd-3m* structure (origin at *-3m*) and a Li_2MnO_3 secondary phase in space group *C2/m* based on the structural data of Boulineau *et al*. [128].

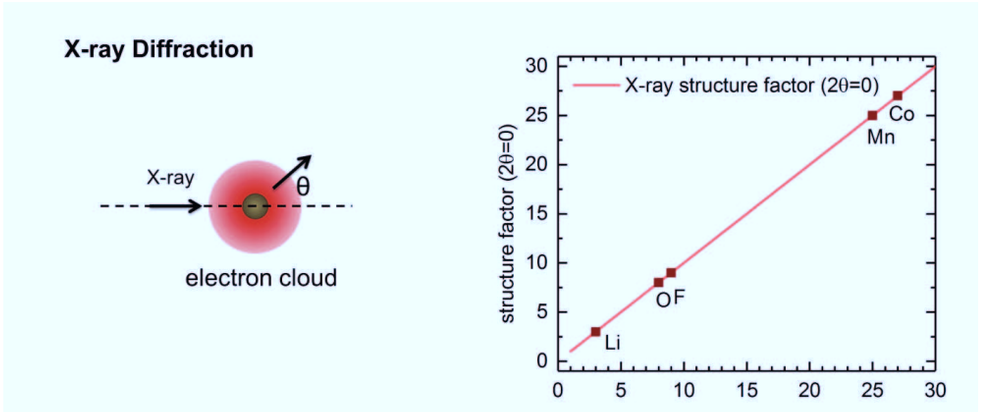

Figure 3.6:.Principle of X-ray diffraction and intensity of scattered X-rays as a function of the electron density of the given element, for a Bragg angle of 2θ = 0 (only for 2θ = 0 the structure factor equals the number electrons / atomic number of the given element) [129].

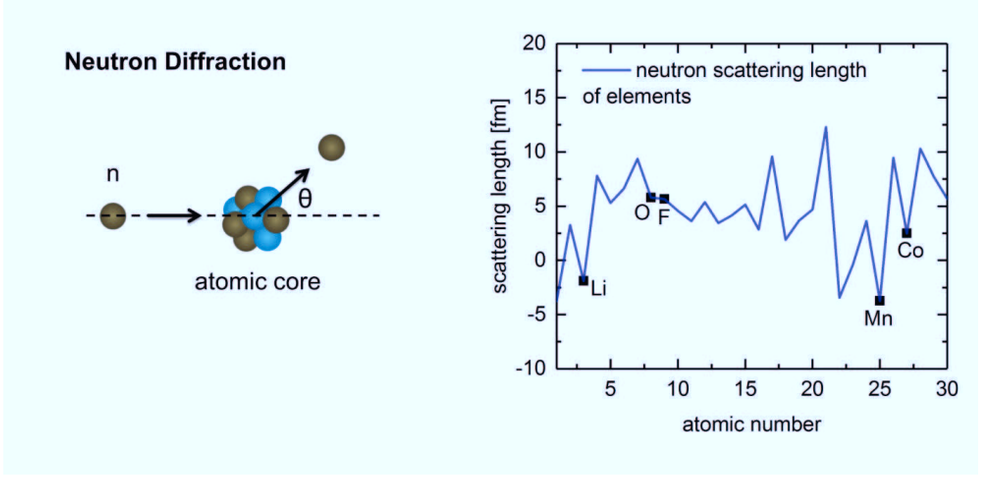

Figure 3.7: Principle of Neutron diffraction and neutron scattering length as a function of the atomic number. The scattering lengths of the elements were taken from Sears [130].

3.3 Electrochemical characterization

For the electrochemical characterizations, the powders were mixed with 10 wt.-% carbon black (BLACK PEARLS; Cabot) and 15 wt.-% polyvinylidene fluoride (PVdF) (Alpha Aesar) dissolved in N-methyl-2-pyrrolidone (Alpha Aesar) to prepare slurries. The slurries were painted on stainless steel current collectors. After drying at 80 °C for 18 h cells were assembled using lithium foil as the anode and a separator saturated with liquid electrolyte in Swagelok cells. The used electrolytes were 1M $LiPF_6$ dissolved in an ethylene carbonate (EC) and dimethyl carbonate solution (DMC), with a volume ratio of EC : DMC = 1 : 1; or 1M $LiPF_6$ dissolved in an EC and diethyl carbonate solution (DEC), with a volume ratio of EC : DEC = 1 : 1.

The electrochemical measurements were performed with a VMP-300 (Bio-Logic) for the Pechini powders and LCMOLiF powders. To verify the electrochemical activity of dense pellets sintered with LiF as sintering additive, a LCMOLiF10_900 sample was crushed and milled and prepared as cathode. Table 3.7 lists the setups and measurement conditions for cyclic voltammetry (CV) measurements, galvanostatic charge-discharge measurements (CHDC) and rate capability tests.

Table 3.7: Electrochemical measurements setup and sample systems.

Sample	Measurement setup	Liquid electrolyte	Sample mass [mg]	Voltage range [V]	C-rates / scan rate
LNMO_pec	CV	1M $LiPF_6$ in EC/DMC (1:1)	1	3.5 – 4.9	0.1 mV/s
LMFO_pec, LCMO_pec	CV	1M $LiPF_6$ in EC/DEC (1:1)	1	3.5 – 5.3	0.1 mV/s
LCMOLiF10_900*	CV	1M $LiPF_6$ in EC/DEC (1:1)	1	3.5 – 5.3	0.1 mV/s
LCMOF	CV	1M $LiPF_6$ in EC/DEC (1:1)	6	3.5 – 5.3	0.1 mV/s
LCMOF	CHDC	1M $LiPF_6$ in EC/DEC (1:1)	6	3.5 – 5.3	C/5×
LCMOF	Rate capability	1M $LiPF_6$ in EC/DEC (1:1)	6	3.5 – 5.3	C/5, C/2, 1C, 2C, C/5
LCMOF	CV	1M LiPF6 in EC/DEC (1:1)	2	3.4 – 5.3	0.1, 0.13, 0.16, 0.21, 0.4, 0.65 mV/s

*) for the electrochemical measurements, the LCMOLiF10_900 pellet was crushed and ground with mortar and pestle, before slurry preparation.

4 Experimental results

4.1 Part I: Synthesis and analysis of $LiNi_{0.5}Mn_{1.5}O_4$, $LiFe_{0.5}Mn_{1.5}O_4$, $LiCoMnO_4$

4.1.1 Structural and microstructural properties

Spinel powders are obtained from Pechini synthesis after calcination and annealing. After the calcination step at 650°C, the major phase in the powders is spinel. All samples contain impurity phases, such as Mn_2O_3 in case of LFMO_pec, $Li(Ni,Mn)O_2$ in case of LNMO_pec and Li_2MnO_3 for LCMO_pec (Figure 4.1). Subsequent homogenization and annealing at 650 °C produces phase pure $LiNi_{0.5}Mn_{1.5}O_4$, and $LiFe_{0.5}Mn_{1.5}O_4$ (Figure 4.2). With the given synthesis route, it was not possible to synthesize phase pure powder of $LiCoMnO_4$, as will be discussed later. For the LCMO_pec sample in Figure 4.2, 8 wt.-% of Li_2MnO_3 was quantified by the Rietveld method.

The prepared spinels crystallize in space group *Fd-3m* with a lattice parameter of a = 8.17 Å, a = 8.24 Å and a = 8.06 Å for LNMO_pec, LFMO_pec and LCMO_pec, respectively, consistent to the literature [6]. $LiNi_{0.5}Mn_{1.5}O_4$, $LiFe_{0.5}Mn_{1.5}O_4$ and $LiCoMnO_4$ can be considered as derivatives from $LiMn_2O_4$ spinel, where Mn-ions at the *16d* octahedral site are substituted by Ni^{2+}, Fe^{3+} or Co^{3+}. $LiMn_2O_4$ has a lattice parameter of 8.249 Å [131], which will change according to the average ionic radius of the transition metals on the *16d* site, which changes with the substituent.

Figure 4.3 displays the lattice parameter changes as a function of the average ionic radius of the transition metal cations on the octahedral site in lithium manganese based spinels. Aliovalent substitution of 0.5 mol Mn^{3+} by Ni^{2+} in $LiMn^{3+}Mn^{4+}O_4$ causes 1 mol Mn^{3+} to oxidize to Mn^{4+} to yield $LiNi_{0.5}{}^{2+}Mn_{1.5}{}^{4+}O_4$. The exchange of the relatively big Mn^{3+} (0.645 Å) for Mn^{4+} (0.53 Å) [132] results in a lower average radius of the transition metals at the *16d* site and causes a shrinkage of the lattice volume compared to $LiMn_2O_4$, i.e. a = 8.17 Å for $LiNi_{0.5}Mn_{1.5}O_4$ and a = 8.249 Å for $LiMn_2O_4$ [131].

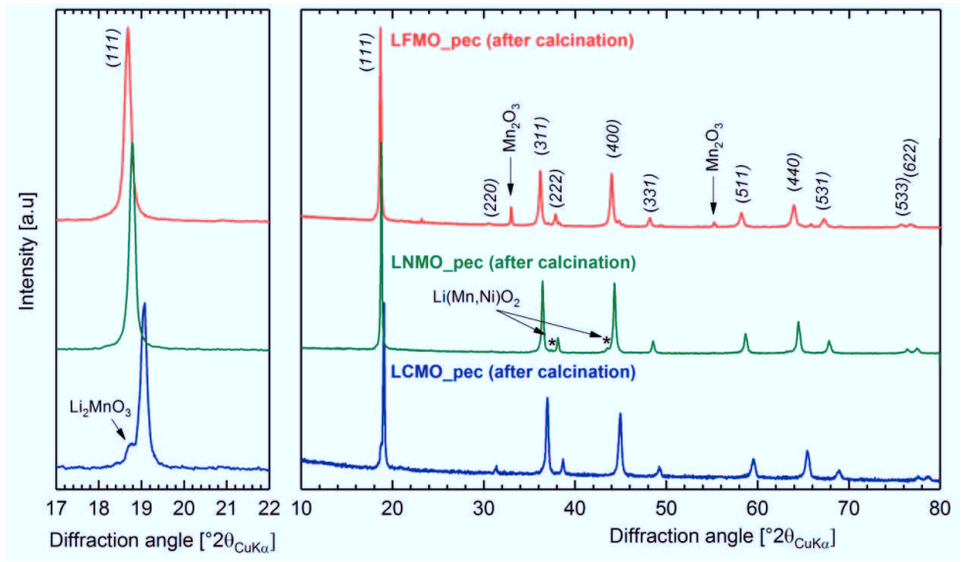

Figure 4.1: XRD patterns of LMCO_pec, LMFO_pec and LMNO_pec after calcination.

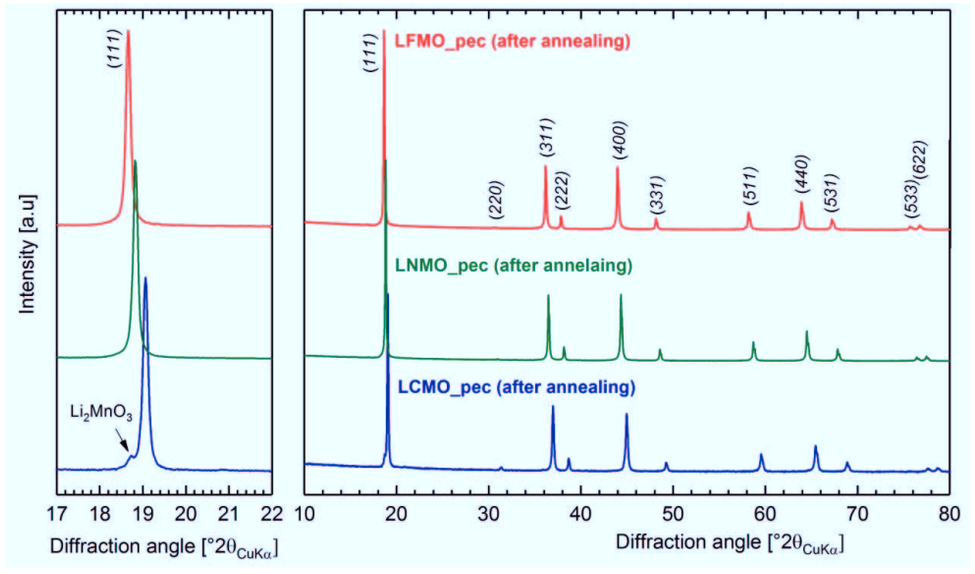

Figure 4.2: XRD patterns of LMCO_pec, LMFO_pec and LMNO_pec after annealing.

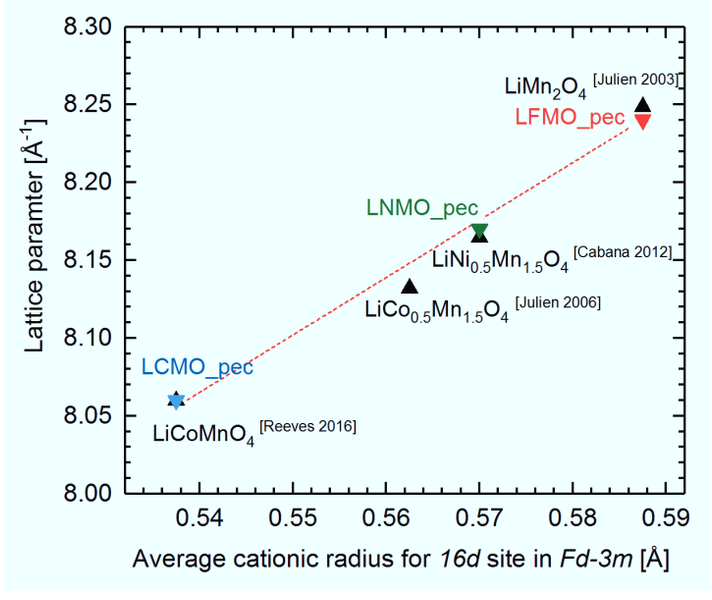

Figure 4.3: Correlation of the lattice parameter to the average ionic radius of the transition metal cations on the octahedral site in lithium manganese based spinels (space group *Fd-3m*) for LCMO_pec, LFMO_pec and LNMO_pec in comparison to literature data for $LiMn_2O_4$ [131], $LiNi_{0.5}Mn_{1.5}O_4$ [30], $LiCo_{0.5}Mn_{1.5}O_4$ [133] and $LiCoMnO_4$ [100].

For $LiFe_{0.5}Mn_{1.5}O_4$ and $LiCoMnO_4$, Mn^{3+} is substituted isovalentely by Fe^{3+} and Co^{3+}, respectively. Substitution of Mn^{3+} by Fe^{3+} results in a very similar lattice parameter for $LiMn_2O_4$ (a = 8.249 Å [131]) and $LiFe_{0.5}Mn_{1.5}O_4$ (a = 8.24 Å), because of the identical sizes of the Mn^{3+}-ion and the Fe^{3+}-ion in octahedral coordination (both 0.645 Å [132]). Co^{3+} takes up the low spin state in oxide compounds in octahedral coordination and its radius becomes relatively small (0.545 Å) [26,132], which is why the lattice parameter for LCMO_pec displays the lowest value (a = 8.06 Å). For comparison, lattice parameters from literature were inserted in Figure 4.3 for $LiCoMnO_4$ [100] and $LiNi_{0.5}Mn_{1.5}O_4$ [30], as well as for $LiMn_2O_4$ (Mn^{3+} : Mn^{4+} = 1 : 1) [131] and $LiCo_{0.5}Mn_{1.5}O_4$ (Co^{3+} : Mn^{3+} : Mn^{4+} = 0.5 : 0.5 : 1) [133]. The ionic radii were taken from Shannon [132].

Cubic spinel, in *Fd-3m* structure, possesses the O_h^7 spectroscopic symmetry and is expected to show five Raman active modes. Three modes are correlated to the vibrations of the oxygen to cation bonding of the octahedrally coordinated transition metals: one symmetric stretching mode (A_{1g}) and two asymmetric bending modes ($F_{2g}^{(1)}$, $F_{2g}^{(2)}$). The other two modes belong to the vibrations of the Li-O bonding:

one asymmetric bending mode ($F_{2g}^{(3)}$) and one symmetric stretching mode (E_g) [131].

Figure 4.4 shows the experimental and fitted Raman spectra based on the averaged and normalized data collected from a sample surface area of 70 µm × 40 µm. LCMO_pec displays a series of broad bands, with two high intensity bands at 650 and 575 cm^{-1} belonging to its A_{1g} and $F_{2g}^{(1)}$ mode, respectively. Two further characteristic bands are identified which peak at 534 and 379 cm^{-1}, belonging to the $F_{2g}^{(1)}$ and E_g mode [100]. Li_2MnO_3 usually shows a characteristic high intensity band at around 612 and 493 cm^{-1} [134]. The shoulder at the $F_{2g}^{(1)}$ mode of spinel, which is fitted with a center at 613 cm^{-1} (v_1) and the band with a center at 494 cm^{-1} (v_2) indicate the presence of Li_2MnO_3 in the sample, in coherence to the XRD results.

The spectral features of LFMO_pec are rather similar to $LiMn_2O_4$ spectral features [131], with a dominating high intense band at 625 cm^{-1} belonging to its A_{1g} mode. In $LiMn_2O_4$ Raman spectra, a shoulder appears at 580 cm^{-1} which is assigned to the $F_{2g}^{(1)}$ mode. This band has a lower intensity and is not well separated from the A_{1g} mode in $LiMn_2O_4$ samples. For the LFMO_pec sample, this band is broad but clearly separated.

LNMO_pec shows more than the expected five bands of the O_h^7 spectroscopic symmetry. $LiNi_{0.5}Mn_{1.5}O_4$ spinels are well known to show a symmetry reduction from *Fd-3m* to $P4_332$ due to cation ordering. The latter structure is represented by the O^7 spectroscopic group, with more Raman active modes due to symmetry reduction [133]. Dominant features are the A_1 mode at 638 cm^{-1}, which is the pendant to the A_{1g} mode of the O_h^7 spectroscopic symmetry, and a band at 495 cm^{-1}, corresponding to Ni^{2+}-O stretching modes, in coherence to literature [133]. The $F_{2g}^{(1)}$ modes from the O_h^7 spectroscopic symmetry are split into individual bands corresponding to the F_1 modes in the O^7 spectroscopic symmetry in between 560 to 620 cm^{-1} consistent to literature [133].

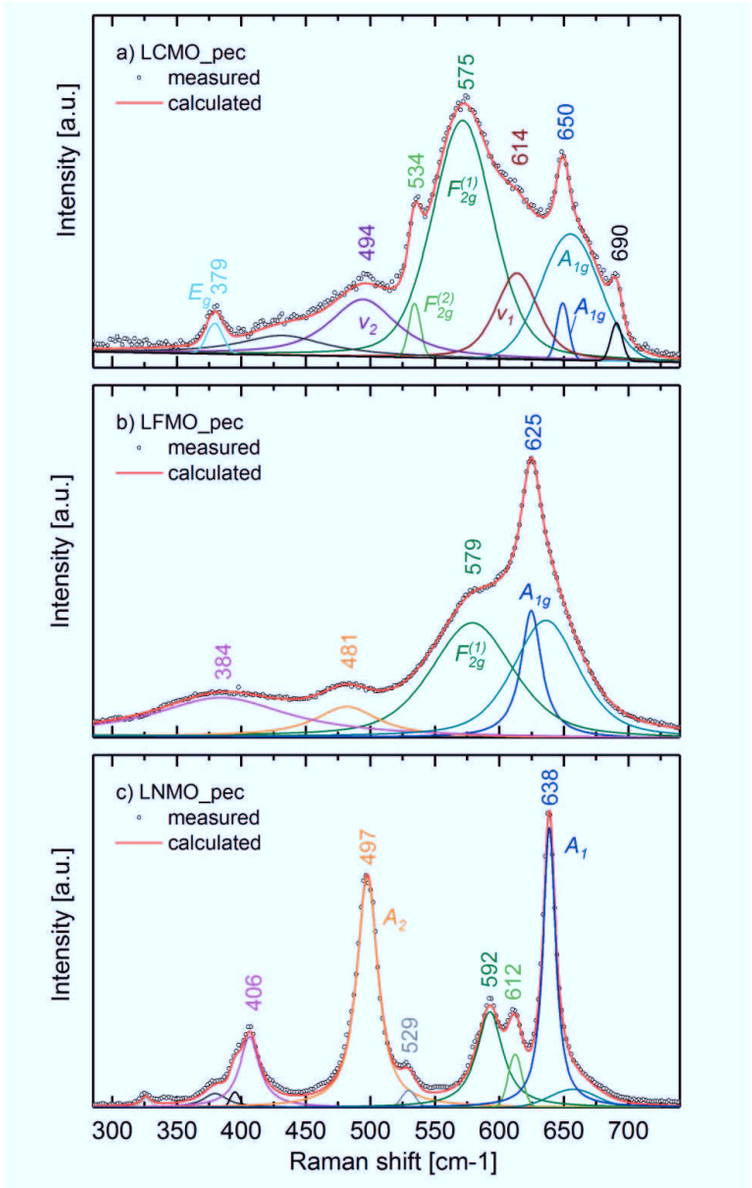

Figure 4.4: Results of the micro Raman spectroscopy from a sample surface area of 70 µm × 40 µm. Averaged and normalized data from measurement with fitted spectra for a) LCMO_pec, b) LFMO_pec and c) LNMO_pec.

The position of the bands corresponding to the A_{1g} and A_1 modes of spinel correlate with the oxygen to transition metal ion bond length in spinel, which is determined by their average ionic radius [133]. Figure 4.5 shows the band position

of A_{1g} modes of lithium manganese based spinels as a function of the average ionic radius of the octahedrally coordinated transition metals in various spinels. The average radii of the transition metals on the octahedral site are 0.57 Å for $LiNi^{2+}_{0.5}Mn^{4+}_{1.5}O_4$, 0.5875 Å for $LiFe^{3+}_{0.5}Mn^{3+}_{0.5}Mn^{4+}O_4$ and 0.5375 Å for $LiCo^{3+}Mn^{4+}O_4$. Literature data for the A_{1g} mode were added to Figure 4.5 for $LiCoMnO_4$ [100] and $LiNi_{0.5}Mn_{1.5}O_4$ [133], as well as data points for $LiMn_2O_4$ (Mn^{3+} : Mn^{4+} = 1 : 1) [134] and $LiCo_{0.5}Mn_{1.5}O_4$ (Co^{3+} : Mn^{3+} : Mn^{4+} = 0.5 : 0.5 : 1) [133]. The ionic radii were taken from Shannon [132]. Only LCMO_pec shows significant deviations from the literature data regarding the position of its A_{1g} mode, as will be discussed in section 5.1.1.

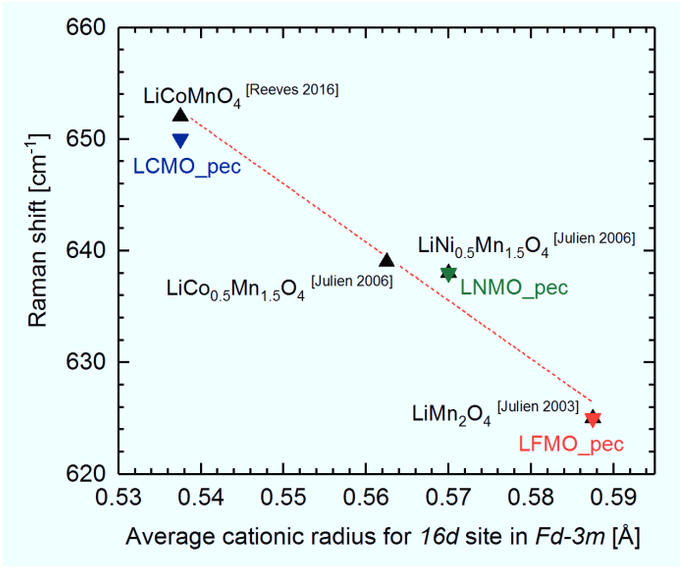

Figure 4.5: Correlation of the position of the band center of the A_{1g} mode of LCMO_pec and LFMO_pec and the A_1 mode of LNMO_pec to the average ionic radius of the transition metal cations on the octahedral site in lithium manganese based spinels and for literature data for $LiMn_2O_4$ [134], for $LiNi_{0.5}Mn_{1.5}O_4$ and for $LiCo_{0.5}Mn_{1.5}O_4$ [133] and for $LiCoMnO_4$ [100].

The particles of the Pechini powders are below 500 nm in size, showing rather low crystallinity, possibly due to the very low synthesis temperatures (Figure 4.6). Accordingly, the typical octahedral habitus of well crystallized spinel grains cannot be found. Deviations from the expected octahedral habitus of spinels are most pronounced for LNMO_pec: Due to the long calcination time at 650 °C for LNMO_pec to obtain a phase pure material, sintering of agglomerates is visible, which leads to a rounded-polygonal particle morphology.

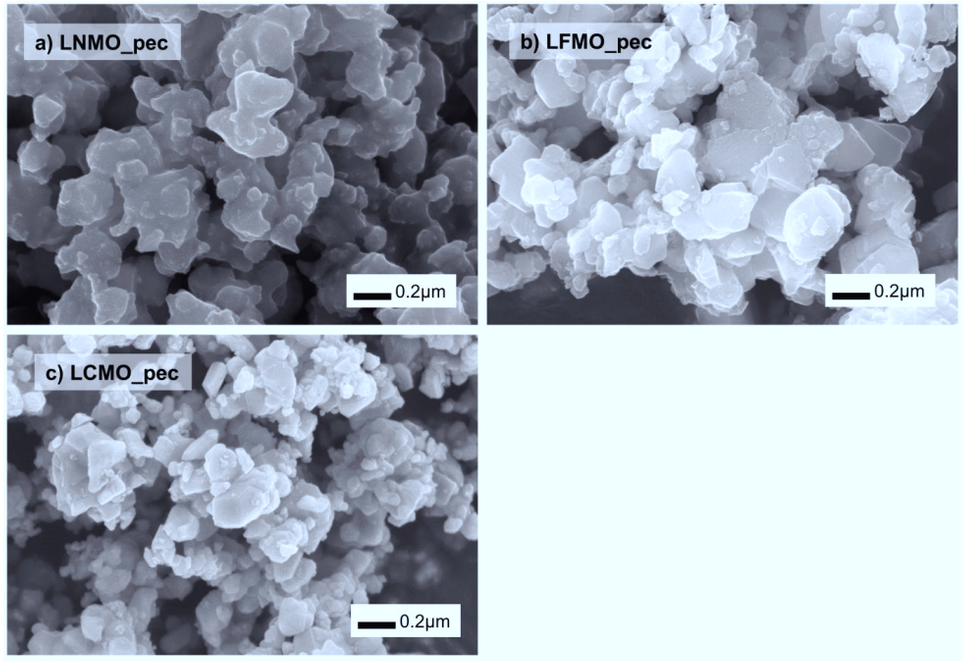

Figure 4.6: SEM images LNMO_pec, LFMO_pec and LCMO_pec.

4.1.2 Electrochemical activity

CV measurements were carried out to verify the electrochemical activities of the synthesized high voltage spinels. Figure 4.7 shows the CV diagrams for each spinel obtained from Pechini synthesis, prepared as cathodes and mounted in a Swagelok cell as described in the experimental section in 3.3. For LNMO_pec, a main oxidation reaction can be measured at 4.8 V vs. Li/Li^+ (peak current 523 mAg^{-1}) with the reverse reaction at 4.7 V vs. Li/Li^+ (-355 mAg^{-1}). This reaction belongs to the $Ni^{2+/4+}$ reaction, in consistence to literature [6]. Additionally, a small contribution (9 and -9 mAg^{-1} peak current) of an additional reaction can be monitored, centered at 4.0 V vs. Li/Li^+, which belongs to the $Mn^{3+/4+}$ reaction [33,135] and indicates the presence of Mn^{3+} induced by oxygen deficiencies in the spinel lattice [82].

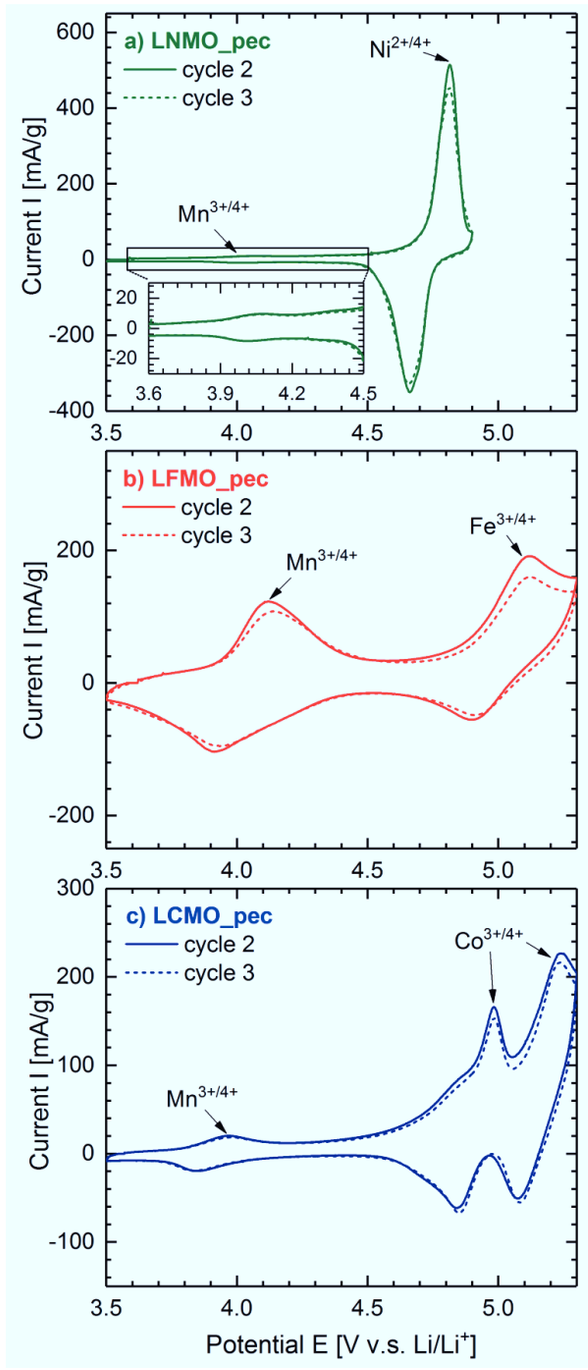

Figure 4.7: CV of the samples a) LMNO_pec, b) LMFO_pec and c) LMCO_pec.

LFMO_pec shows two oxidation and reduction reactions centered at around 4.1 and 5.1, and 3.9 and 4.9 V vs. Li/Li^+, respectively, which belong to the $Mn^{3+/4+}$ and $Fe^{3+/4+}$ reactions, as is expected for a $LiFe^{3+}_{0.5}Mn^{3+}_{0.5}Mn^{4+}O_4$ compound and is in agreement with literature [6]. Both reactions have a similar forward peak current, which is 127 and 193 $mAhg^{-1}$. The reversed reaction is symmetric for the reaction centered at 4.0 V vs. Li/Li^+ (-107 mAg^{-1}) and highly asymmetric for the reaction centered at 5.0 V vs. Li/Li^+ (-57 mAg^{-1}). This asymmetry in the high voltage region is caused by irreversible liquid electrolyte decomposition reactions, which also lead to cell degradation. As can be seen in Figure 4.7b, the 3rd cycle shows cell degradation and does no more reproduce the data from the 2nd cycle.

LCMO_pec shows a two-step redox reaction in the 5 V vs. Li/Li^+ region, which is typical for the $Co^{3+/4+}$ redox reaction in $LiCoMnO_4$ [136]. Although the underlying mechanism of the double-peaked feature for the $Co^{3+/4+}$ redox couple is not yet clear, analogies to $LiMn_2O_4$ CV characteristics suggest their association with the order-disorder phase transition of Li-ions in the *8a* sublattice [137]. The sample also shows a broader signal at around 4.8 to 4.9 V vs. Li/Li^+, which is characteristic for the redox processes of slightly non-stoichiometric $LiCoMnO_4$ [101]. Additionally, a small contribution of the $Mn^{3+/4+}$ reaction at 3.9 to 4.0 V vs. Li/Li^+ [101] was measured for LCMO_pec.

4.1.3 Thermal reactions

The thermal decomposition characteristics in air of all three investigated high voltage cathodes are comparable, as shown in Figure 4.8. After initial reactions for the desorption of surface-adsorbed H_2O below 300 °C, the TG signals remain constant and no changes in the DTA signals are observed. From T_2 = 650 °C and higher, mass loss occurs parallel to endothermic reactions in several steps, as is typical for lithium manganese spinels due to oxygen loss [14,100]. T_2 marks the beginning of oxygen loss, which eventually leads to the precipitation of an Li_2MnO_3 phase with a lower oxygen content [14,100] at T_3 = 750 °C. The endothermic reaction at T_4 marks the reaction of spinel and Li_2MnO_3 to $LiCoMnO_3$ [100]. The peak temperatures of the endothermic reactions at T_4 are slightly different for the different samples with $T_{4\_LNMO\_pec} < T_{4\_LCMO\_pec} < T_{4\_LFMO\_pec}$. During cooling, a mass uptake of around 70 to 80 wt.-% of the lost mass between T_2 and the maximum temperature

(T_{max}) is measured for all three samples. Additionally, $LiCoMnO_3$ reacts back to spinel and Li_2MnO_3 [100], which is measured as an exothermic reaction at temperature T_5.

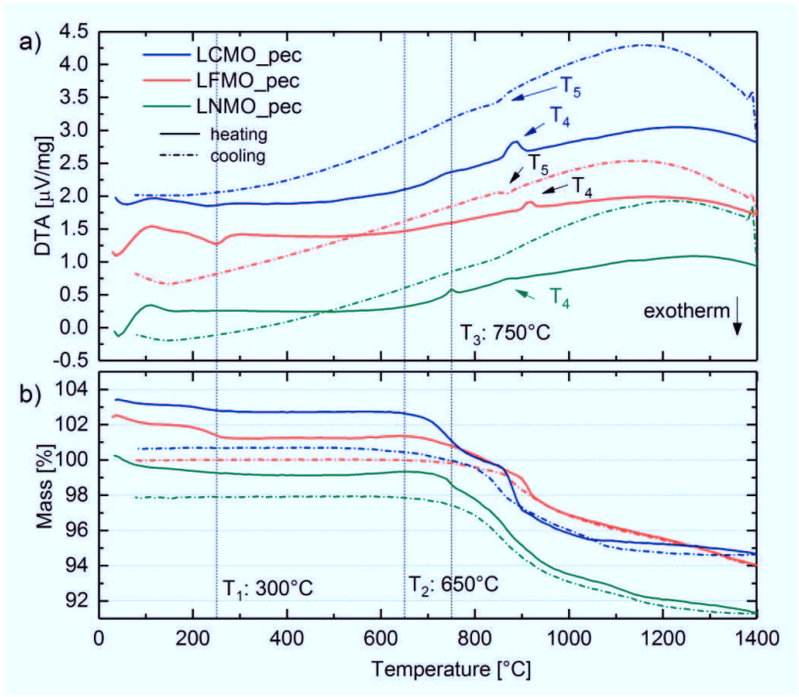

Figure 4.8: a) DTA and b) TG results of spinel powders. DTA signal offset: 1 unit (for LFMO_pec), 2 units (for LCMO_pec). TG signal offset: 2 units (for LFMO_pec) and 4 units (for LCMO_pec).

4.2 Part II: Compatibility of $LiNi_{0.5}Mn_{1.5}O_4$, $LiFe_{0.5}Mn_{1.5}O_4$ and $LiCoMnO_4$ with solid electrolytes

Processing of mixed cathodes by sintering requires the chemical stability of the cathode and the electrolyte at the sintering temperature. This section presents the experimental results of the DTA/TG, ex-situ and in-situ XRD analysis for co-sintered spinel + electrolyte mixtures.

4.2.1 Thermal reactions of spinels in mixture with electrolytes

The thermal analysis by DTA/TG of the spinel+LLZ powders reveals a comparable behavior upon heating for all three mixtures (Figure 4.9). Several sequential steps of mass loss are observed already below 500 °C, which can be assigned to the loss of CO_2 and H_2O by coupled mass spectroscopy (not shown). The loss of CO_2 and H_2O at temperatures below 600 °C is characteristic for air sensitive LLZ [138].

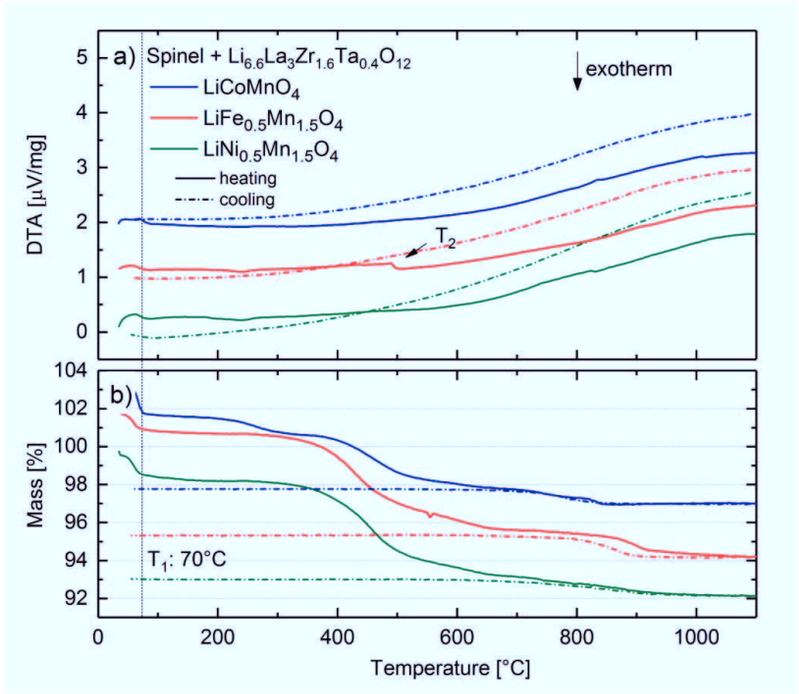

Figure 4.9: a) DTA and b) TG of spinel+LLZ powders. DTA signal offset: 1 unit (for LFMO), 2 units (for LCMO). TG signal offset: 2 units (for LFMO) and 4 units (for LCMO).

No significant endo- or exothermic reactions can be observed within the whole measured temperature range. A small endothermic signal is detected for

LFMO+LLZ at 490 °C, which could be artificial. The mass loss continues above 600 °C, which is likely due to the loss of oxygen since no elements can be detected by mass spectroscopy (not shown). Between T_1 and T_{max}, around 6.5 wt.-% mass is released from the LFMO+LLZ sample, 6.0 wt.-% from the LNMO+LLZ sample, and 4.5 wt.-% from the LMCO+LLZ sample, whereas around 13 to 17 % of this mass is taken up again during cooling.

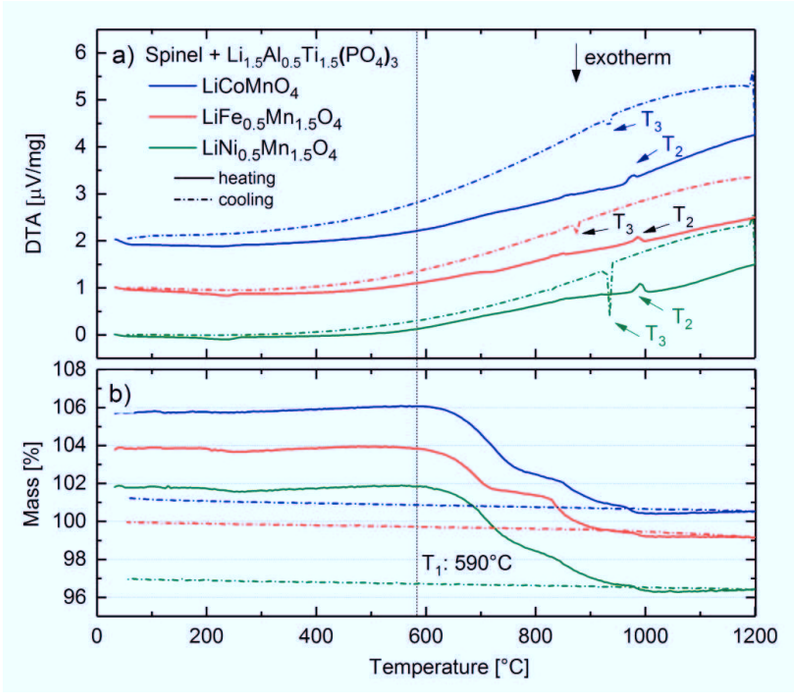

Figure 4.10: a) DTA and b) TG of spinel+LATP powders. DTA signal offset: 1 unit (for LFMO), 2 units (for LCMO). TG signal offset: 2 units (for LFMO) and 4 units (for LCMO).

Figure 4.10 shows the DTA/TG results of the spinel+LATP powders. The characteristics upon heating to 1200 °C of all three mixtures are comparable. An initial mass loss due to the releasing of surface-adsorbed H_2O and CO_2 occurs below 270 °C. A continuous mass loss starting from 590 °C can be recognized for all three mixtures, which occurs in several steps parallel to endothermic reactions at T_2, which is at 980 °C for LCMO+LATP and at 990 °C for the other two mixtures. A mass loss of around 5 to 6 wt.-% can be measured for all three samples from T_1 to T_{max}. Around 15 % of the lost mass is taken up again during cooling. Additionally, an exothermic

reaction was measured during cooling for LCMO+LATP and LFMO+LATP at around 935 °C and 930 °C, respectively, and for LNMO+LATP at around 880 °C.

4.2.2 Co-sintering of spinels and solid electrolytes at various temperatures

4.2.2.1 Spinel and LLZ

Figure 4.11, Figure 4.12, and Figure 4.13 show the XRD result of co-sintered spinel+LLZ pellets that were heat treated at 400, 600, and 800 °C for one hour. The phase contents obtained at 400 to 800 °C are comparable for all three mixtures. For the samples heat treated at 400 °C, the observed diffraction patterns are the same as the diffraction pattern of the as mixed powders – with spinel and LLZ being the only phases present in the sample.

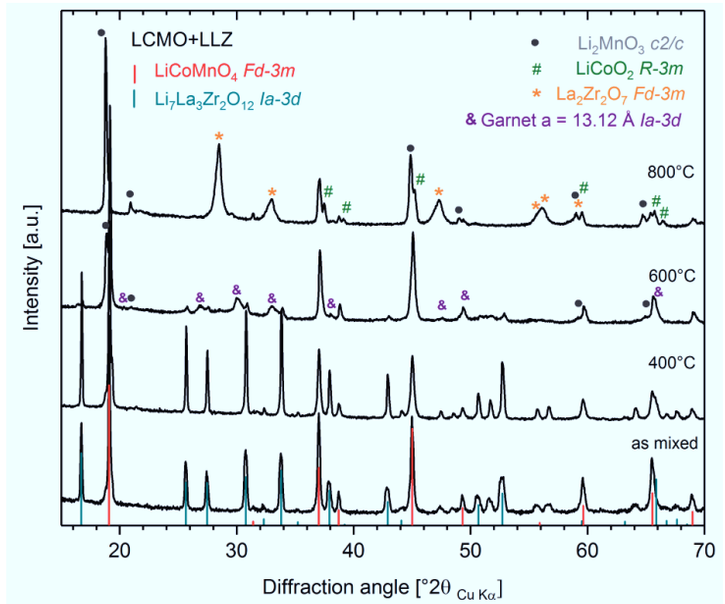

Figure 4.11: XRD patterns of LCMO+LLZ mixtures that were heat treated at 800 °C, 600 °C, 400 °C and as mixed powder.

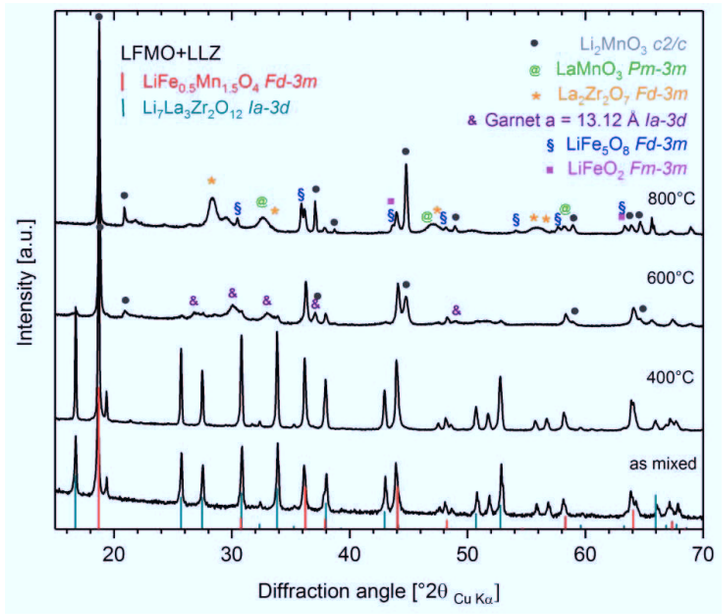

Figure 4.12: XRD patterns of LFMO+LLZ mixtures that were heat treated at 800 °C, 600 °C, 400 °C and as mixed powder.

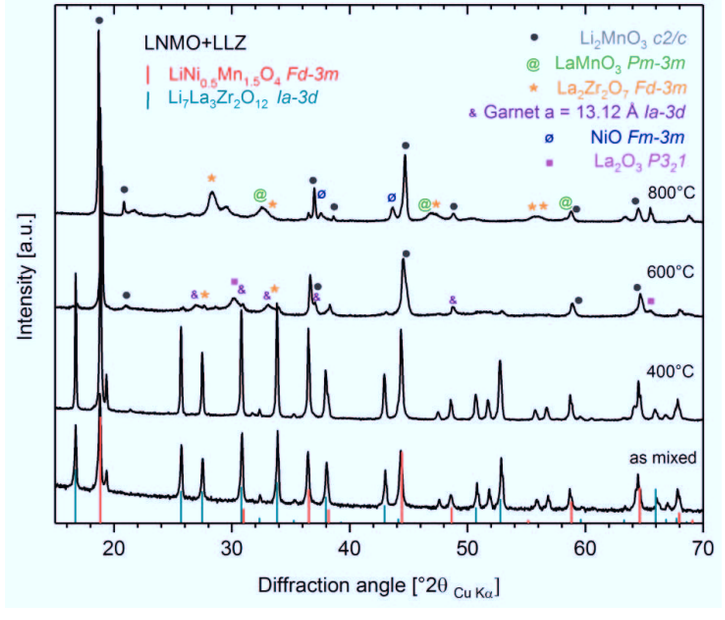

Figure 4.13: XRD patterns of LNMO+LLZ mixtures that were heat treated at 800 °C, 600 °C, 400 °C and as as-mixed powder.

First changes occur in the XRD patterns for the spinel+LLZ pellets which were heat treated at 600 °C. All diffractograms show a contribution of spinel and LLZ. However, the diffraction peak intensities of the LLZ phase decrease significantly in comparison with the diffraction pattern of the as mixed sample. Additionally, the pattern includes a secondary garnet phase and monoclinic Li_2MnO_3.

For the samples heat treated at 800 °C, the intensities of spinel phases are decreased and no more LLZ can be detected. Instead, a $La_2Zr_2O_7$ phase can be identified clearly. Additionally, for LCMO+LLZ, Li_2MnO_3 and $LiCoO_2$ are found. For the LFMO+LLZ sample, $LaMnO_3$ and $LiFe_5O_8$ are found, whereas $LaMnO_3$ and NiO are found in the LCMO+LLZ sample.

4.2.2.2 Spinel and LATP

XRD performed on LCMO+LATP pellets, which were co-sintered at 600, 700, and 800 °C, are shown in Figure 4.14. The XRD pattern of the LCMO+LATP pellet heat treated at 600 °C contains only LATP and spinel, the same as the as mixed powder. Major changes are seen at 700 °C: both educt phases were detected at their initial peak positions, but the intensities of the LATP and spinel phase are decreased significantly compared with the sample heat treated at 600 °C. Additionally, the pattern needs to be described by at least two orthorhombic phosphate phases and TiO_2, which indicates that the mixture of LATP and $LiCoMnO_4$ already undergoes serious chemical reactions at this temperature.

At 800 °C LATP is consumed completely by forming new phosphate phases in reaction with $LiCoMnO_4$. A peak shift of the spinel Bragg peaks to lower angles indicates a major change in the chemistry of the spinel phase at 800 °C. Additionally, a series of orthorhombic phosphates is necessary to describe the observed patterns completely. Furthermore, TiO_2, Mn_2O_3 and Co_3O_4 can be detected.

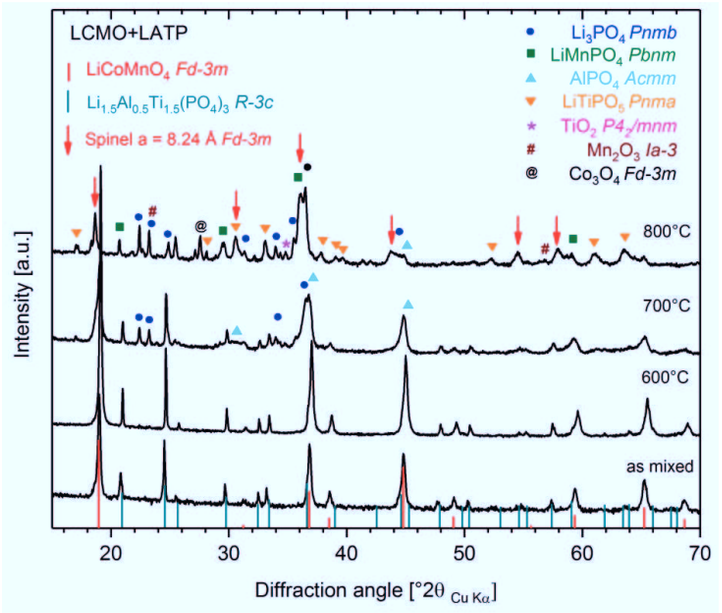

Figure 4.14: XRD patterns of LCMO+LATP mixtures that were heat treated at 800 °C, 700 °C, 600 °C and as mixed powder.

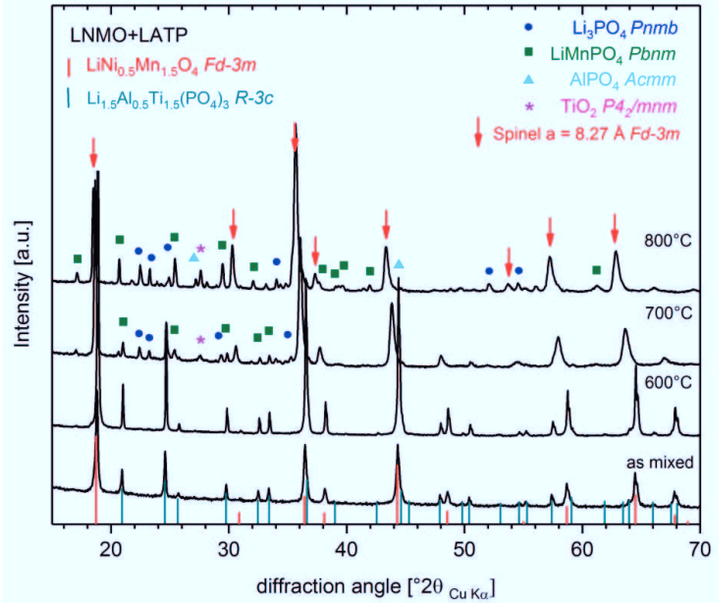

Figure 4.15: XRD patterns of LNMO+LATP mixtures that were heat treated at 800 °C, 700 °C, 600 °C and as mixed powder.

Similar observations were made for LNMO+LATP by XRD analysis as shown in Figure 4.15. The XRD pattern for the LNMO+LATP pellet heat treated at 600 °C,

shows the desired spinel and LATP phases, the same as the as mixed sample. The intensities of the LATP and spinel phases decrease significantly for the sample heat treated at 700 °C in comparison with those at 600 °C. Additionally, a tetragonal phosphate phase and rutile can be identified. Therefore, the LNMO+LATP reaction at 700 °C majorly affects the chemistry of the spinel phase, since $LiNi_{0.5}Mn_{1.5}O_4$ components react with LATP to form new phosphate phases. For the sample heat treated at 800 °C, no more LATP can be detected. The peak positions of the $LiMn_2O_4$ phase are shifted to lower angles and need to be described by another spinel phase with a lattice parameter of a = 8.27 Å. A series of tetragonal phosphates is also necessary to describe the observed diffraction pattern.

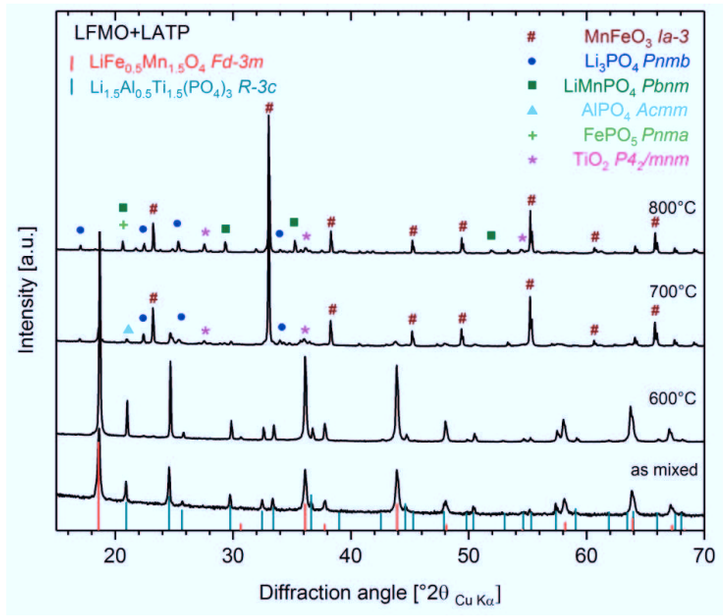

Figure 4.16: XRD patterns of LFMO+LATP mixtures that were heat treated at 800 °C, 700 °C, 600 °C and as mixed powder.

The diffraction pattern for the LFMO+LATP pellet heat treated at 600 °C shows the two phases spinel and LATP, just as the as mixed sample. For the sample heat treated at 700 °C, spinel can still be detected but intensities are decreased, whereas LATP cannot be identified. $LiFe_{0.5}Mn_{1.5}O_4$ spinel and LATP have almost completely reacted to form a $MnFeO_3$-like phase and orthorhombic phosphates. Neither $LiFe_{0.5}Mn_{1.5}O_4$ spinel nor LATP can be identified for the sample heat treated at 800 °C. Instead, at both temperatures, $MnFeO_3$ emerges as main phase and a se-

ries of secondary tetragonal phosphates are necessary to describe the pattern satisfactorily.

4.2.3 Phase evolution as a function of temperature

In Figure 4.17 and Figure 4.18 the in-situ high temperature XRD results for the spinel and electrolyte mixtures are shown to visualize the decomposition reactions as a function of temperature. For spinel+LLZ samples (Figure 4.17), the peaks of the initial spinel and electrolyte phases can be followed until 500 to 550 °C. Beyond this temperature, spinel+LLZ react to new phases, which is visible from the decreasing intensity of the main *111* spinel refection at 18°2θ and shifts of the spinel peaks to lower angles, as well as the vanishing of the electrolyte peaks. The results of the in-situ XRD measurements are in coherence to the ex-situ XRD data, where the co-sintering of spinel+LLZ showed no reaction at 400 °C but was shown to lead to the formation of new phases at 600 °C. Above 750 °C the phases La_2ZrO_7 and Li_2MnO_3 are dominant in all spinel and LLZ mixtures in the in-situ XRD, which is again in coherence to the ex-situ results, where La_2ZrO_7 and Li_2MnO_3 were found as dominating phases for the co-sintering at 800 °C.

The reaction of spinel and LATP starts at 600 °C, as can be concluded from the vanishing peak intensities of the main refection of spinel, at 18°2θ (Figure 4.18). $LiCoMnO_4$ and $LiNi_{0.5}Mn_{1.5}O_4$ with LATP react to a new spinel phase as major phase and a series of phosphates, in coherence to the ex-situ XRD results for co-sintering at 700 and 800 °C for $LiCoMnO_4$ and $LiNi_{0.5}Mn_{1.5}O_4$ with LATP. For $LiFe_{0.5}Mn_{1.5}O_4$ and LATP, $MnFeO_3$ emerges as major phase at 700 °C in the in-situ measurement. In the ex-situ measurements, $MnFeO_3$ and as series of phosphates is found for LFMO+LATP at 700 and 800 °C, which is in good coherence to the in-situ XRD results.

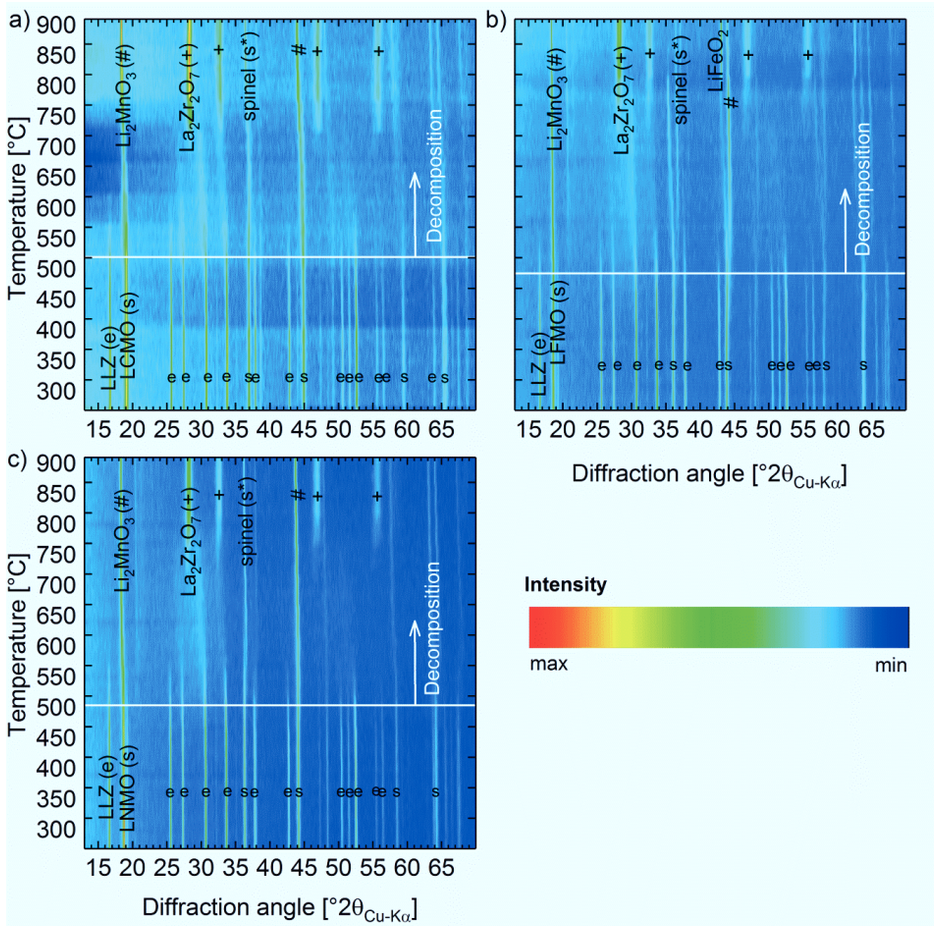

Figure 4.17: In-situ high temperature XRD of a) LCMO+LLZ, b) LFMO+LLZ, and c) LNMO+LLZ in between 300 and 900 °C in 50 K steps. At each temperature, five scans were collected.

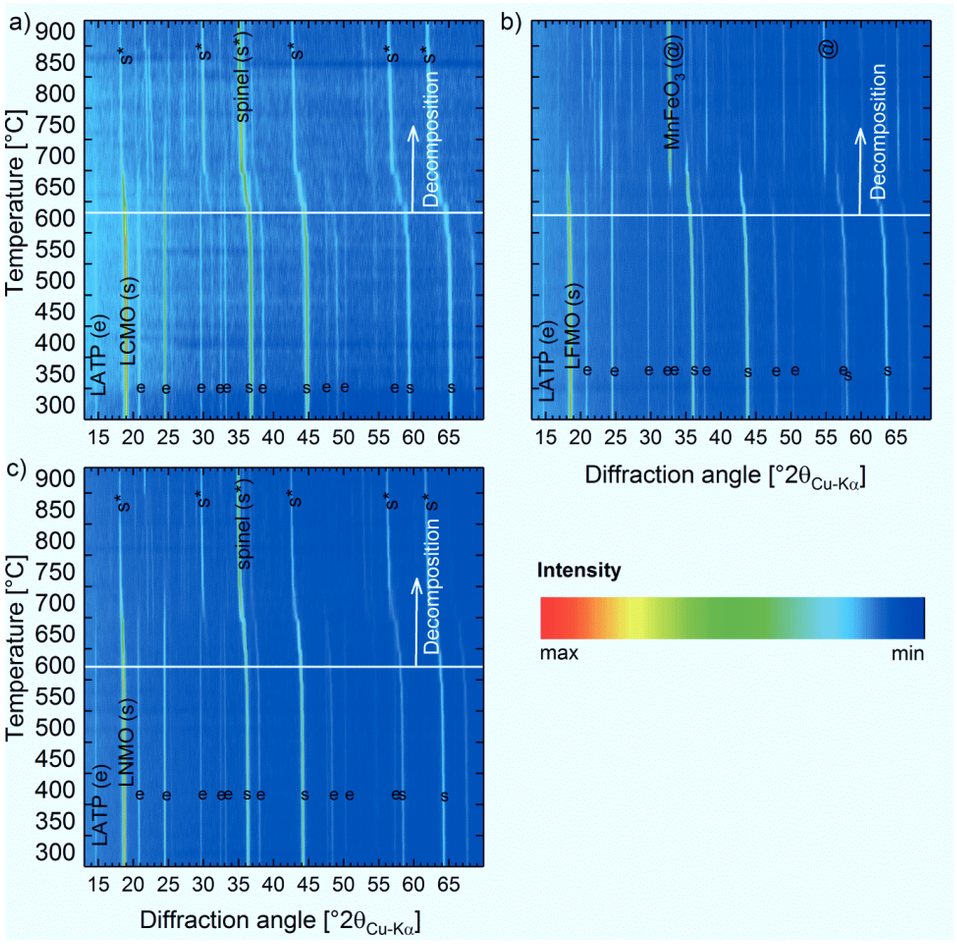

Figure 4.18: In-situ high temperature XRD of a) LCMO+LATP, b) LFMO+LATP, and c) LNMO+LATP in between 300 and 900 °C in 50 K steps. At each temperature, five scans were collected.

4.3 Part III: Densification of $LiCoMnO_4$ with LiF additive

Processing of a dense active material for either mixed cathodes or for thin self-supported cathodes by sintering (as described in section 1, *III*) requires sufficient sinterability of the material. Due to the oxygen loss of the investigated spinels, starting at an onset temperature of 650 °C and subsequent decomposition reactions as described in section 4.1.3, its densification by usual sintering in air is challenging. Since LiF is a well-known sintering additive for various oxide materials [139–141], it was investigated for the densification of $LiCoMnO_4$ spinel within this dissertation. This section presents the results of the densification of LCMO_pec with LiF as sintering additive.

4.3.1 Densification behavior and phase content

The improved sintering behavior of LCMO_pec by 1 wt.-% LiF addition is evident from the dilatometry results in in Figure 4.19. The densification process of the LCMOLiF10 sample starts at ~600 °C, reaches its maximum shrinkage rate at ~850 °C, and displays a maximum shrinkage of 17.5 % at ~950 °C. In contrast, the densification of LCMO_pec starts ~150 K higher, at ~850 °C, its maximum shrinkage rate is reached at ~900 °C, and at 1100 °C only 10 % shrinkage are achieved.

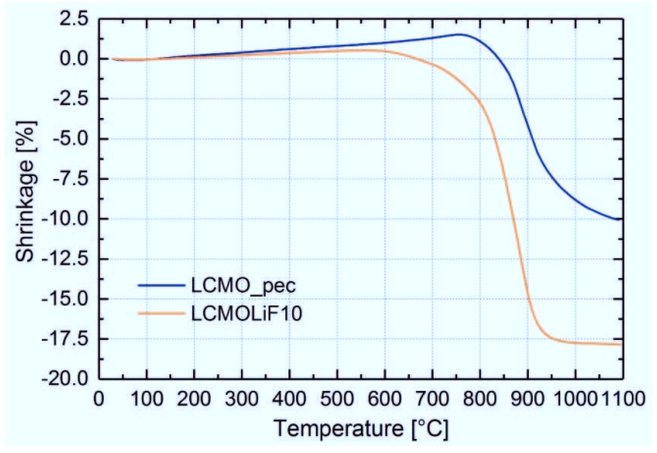

Figure 4.19: Results of dilatometry of LCMO_pec and LCMOLiF10.

Figure 4.20 shows the ex-situ XRD patterns for the LCMOLiF10 samples and LCMO_pec for comparison at different sintering temperatures. $LiCoMnO_4$ spinel,

with a = 8.06 Å [6], can be identified in all nine samples. Additionally, monoclinic Li_2MnO_3 is identified by its *001* and *020* reflections.

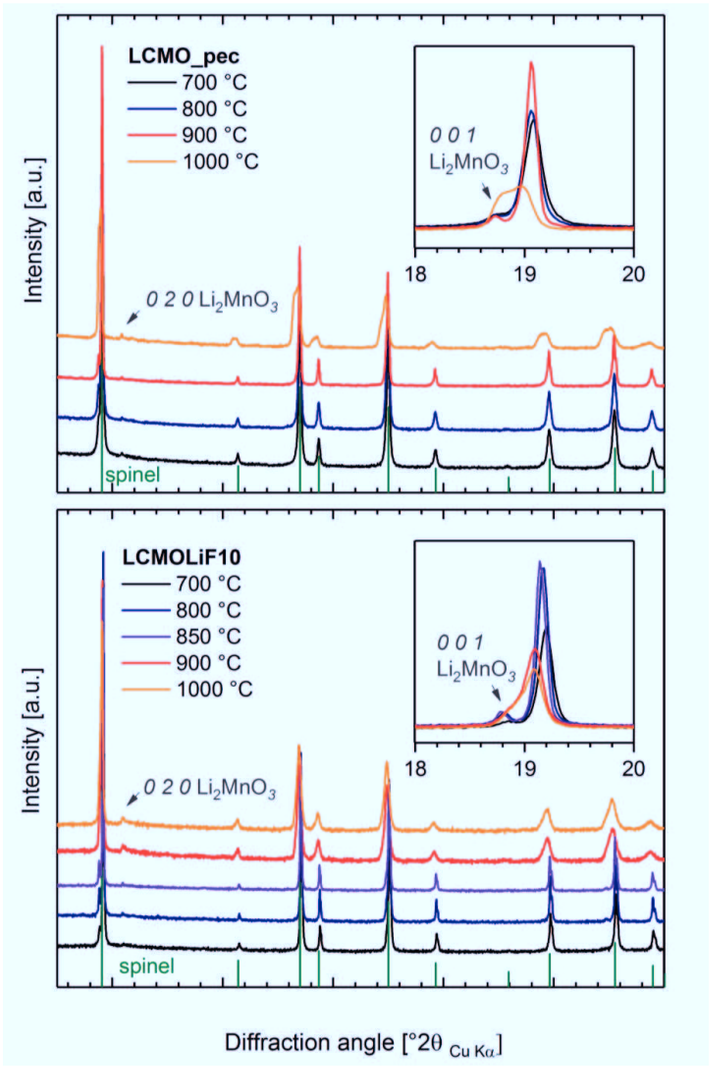

Figure 4.20: Results of ex-situ XRD on LCMO_pec and LCMOLiF10 samples.

Several observations can be made regarding to the changes in peak shapes, peak intensities and peak positions of the observed phases. The intensities of the *001* and *020* reflections of Li_2MnO_3 increase with increasing sintering temperatures for both samples. For the LCMOLiF10 samples sintered at 900 and 1000 °C, a peak shift of the spinel phase to lower diffraction angles can be observed as well as significant peak broadening. In contrast, the diffraction peaks of the Li_2MnO_3-like

phase shift to higher angles. For LCMO_pec, peak broadening occurs for the sample sintered at 1000 °C as well as peak shift of the spinel and the Li_2MnO_3 phase. The peak shift of Li_2MnO_3 towards higher angles is more pronounced in LCMOLiF10 samples. The relative intensity of the Li_2MnO_3-*020* reflection is observed to be slightly smaller as in corresponding LCMO_pec samples, indicating higher Li_2MnO_3 contents in the LCMOLiF10 samples.

4.3.2 Identifying optimal sintering conditions and resulting microstructure

The results of the obtained relative densities for different sintering temperatures and with different amounts of LiF additive are summarized in Table 4.1 and Figure 4.21a. The relative densities were calculated from the absolute densities, as measured by Archimedes method, divided by the theoretical densities, which were calculated from the lattice parameters and phase contents as analyzed by XRD (Table 4.1). Adding 0.5 wt.-% LiF to LCMO_pec leads to similar densities as without LiF addition, i.e. they stay below 85 % relative density even at higher sintering temperatures. The densities for using 1 and 1.5 wt.-% LiF additive display similar values of 90 and 92 % relative density that were gained at 1000 °C (Table 4.1 and Figure 4.21a).

Table 4.1. Phase contents, theoretical and relative densities of LCMOLiF samples.

Sample	Li_2MnO_3 [wt.-%]	Spinel lattice parameter [Å]	Theoretical density [g/cm³]	Measured density [g/cm³]	Relative density [%]
LCMO_800	5.2	8.058	4.648	2.668	57.4
LCMO_1000	7.9	8.077	4.599	3.764	81.8
LCMOLiF05_800	8.0	8.056	4.632	2.500	54.0
LCMOLiF05_900	9.7	8.062	4.609	3.660	79.4
LCMOLiF05_1000	10.0	8.062	4.606	3.673	79.7
LCMOLiF10_700	6.9	8.056	4.637	2.391	51.6
LCMOLiF10_800	11.5	8.057	4.595	2.741	59.7
LCMOLiF10_850	11.6	8.059	4.592	3.333	72.6
LCMOLiF10_900	19.6	8.099	4.481	4.065	90.7
LCMOLiF10_1000	24.7	8.099	4.444	4.021	90.5
LCMOLiF15_1000	32.4	8.180	4.283	3.929	91.7

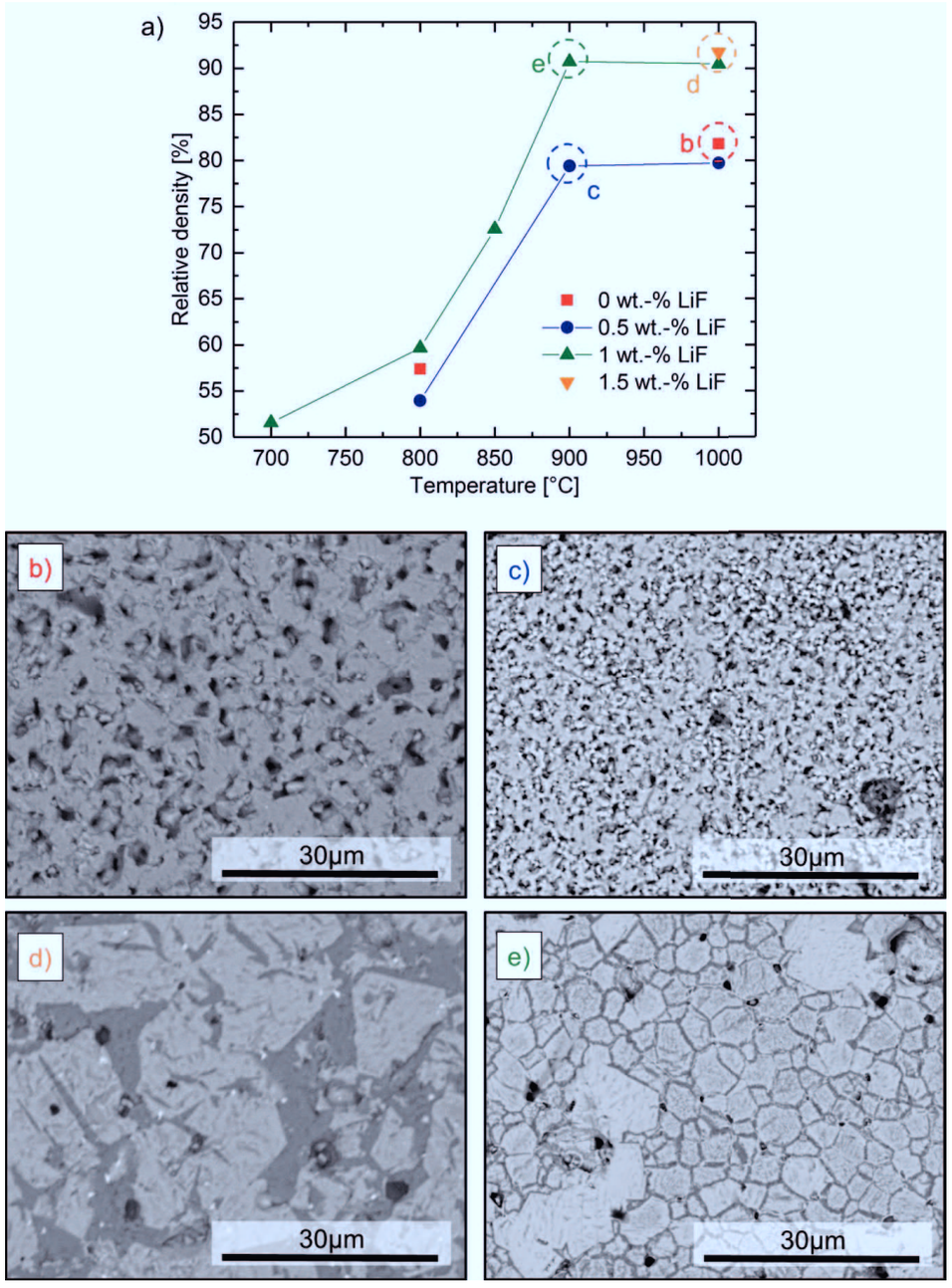

Figure 4.21: a) Obtained relative densities of LCMOLiF samples and SEM images of the samples with the highest achieved relative densities for using different amounts of the LiF sintering additive each: b) LCMO_1000; c) LCMOLiF05_900; d) LCMOLiF15_1000; e) LCMOLiF10_900.

Figure 4.21b shows the obtained microstructure of LCMO_pec, after sintering at 1000 °C for 2 h and 650 °C for 10 h. The particles, with an original particle size of around 0.5 µm, show a significant coarsening to particles of about 5 µm. Sintering necks in between the particles are clearly visible but sufficient densification (relative density 82 %) is not achieved due to pore coarsening. Similarly, the microstructure for the LCMOLiF05_1000 sample, in Figure 4.21c, shows grain and pore coarsening and sufficient densification is not achieved.

Figure 4.21d shows the microstructure of LCMOLiF15_1000. The relative density for this sample is 92 %. However, two phases evolve during sintering: A brighter and a darker phase can be distinguished from the SEM image. The bright phase exhibits a particle size of up to 25 µm. It is embedded in a matrix of the dark phase, which shows sharp angled boundaries to the bright phase. This kind of microstructure indicates the presence of a melting phase during sintering, explaining the improved density as a result of liquid phase sintering. Furthermore, round shaped pores with a diameter of around 5 µm can be found, which imply the existence of a vapor phase during sintering.

The content of the dark phase could be reduced by changing the sintering conditions to 900 °C for 2 h and using 1 wt.-% LiF as sintering additive (LCMOLiF10_900). The bright phase in the SEM image in Figure 4.21e exhibits a particle size of up to 5 µm. The dark phase is located at the grain boundaries of the bright phase. Its width is around 1 to 2 µm. The sample shows round shaped pores, which are not larger than ~3 µm. They can be found at triple junctions of grain boundaries of the bright phase, interjecting the dark phase which spreads along the grain boundaries.

To understand the nature of the phases in the sample, a Raman mapping was carried out for LCMOLiF10_900. The component analysis result based on the Raman mapping is shown in Figure 4.22. Four different components can be identified from the obtained spectra. The main component, colored in dark blue, shows typical Raman spectroscopy features of $LiCoMnO_4$ spinel, with characteristic bands at 652 and 575 cm^{-1} belonging to its A_{1g} and $F_{2g}^{(1)}$ mode (Figure 4.23a) [100]. The second component, colored in cyan, shows typical Raman spectroscopy features of a cubic $(Co,Mn)_3O_4$ spinel compound, with two bands at 573 and

679 cm^{-1} belonging to its A_{1g} and $F_{2g}^{(2)}$ modes [142,143] (Figure 4.23b). The third component, Li_2MnO_3, is identified in the Raman spectra by its characteristic high intensity bands at 617, 502, 445 and 375 cm^{-1} [134] (Figure 4.23c). The last component, with the lowest occurrence in the mapped area, shows the characteristic sharp bands of Co_3O_4 spinel in the Raman spectra, with the highest intensity mode at 697 cm^{-1} belonging to its A_{1g} mode [143,144] (Figure 4.23d).

The dark phase, which was found by SEM (Figure 4.21d) can now be identified as Li_2MnO_3, which is located at the grain boundaries of $LiCoMnO_4$ spinel. $LiCoMnO_4$ spinel is the main phase in the sample. The second $(Co,Mn)_3O_4$-type spinel component, colored in cyan, is present as individual phase with a grain size of up to 10 µm. Just as for the main spinel compound, the Li_2MnO_3 phase is located at its grain boundaries of the second spinel phase. The $(Co,Mn)_3O_4$-type spinel component was also identified as segregates in mainly $LiCoMnO_4$ spinel dominated regions. The Co_3O_4-like compound can be found at the grain boundaries of spinel and is concentrated at triple junctions of grain boundaries of the spinel phase.

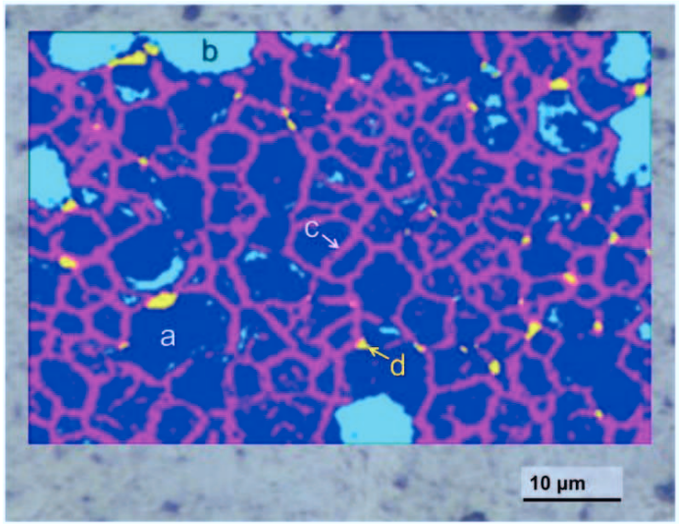

Figure 4.22: Component analysis results of the high-resolution micro Raman mapping for LCMOLiF10_900. Color coded identified components: (a) in blue, $LiCoMnO_4$ spinel; (b) in cyan, $(Co,Mn)_3O_4$-type spinel compound; (c) in magenta, Li_2MnO_3; (d) in yellow, Co_3O_4-type spinel compound. Component spectra below.

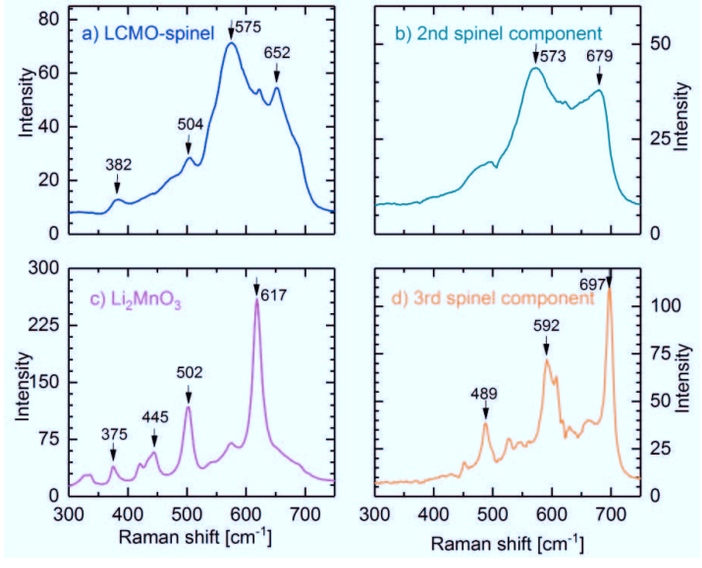

Figure 4.23: Representative spectra of the individual components in the component analysis of the Raman mapping result. a) $LiCoMnO_4$ spinel, b) $(Co,Mn)_3O_4$-type spinel compound, c) Li_2MnO_3, and d) Co_3O_4-type spinel compound.

4.3.3 Sample chemistry as a function of temperature

To monitor changes in the chemistry of the $LiCoMnO_4$ samples sintered with 1 wt.-% LiF, the LCMOLiF10 samples were analyzed by ICP-OES for their cation contents and by IFA for their oxygen contents. As can be seen in Figure 4.24a, the cation contents remain constant for different applied sintering temperatures, while oxygen contents decrease with increasing sintering temperatures. In parallel, the phase content of the secondary Li_2MnO_3 phase increases with increasing sintering temperature and reaches ~25 wt.-% at 1000 °C (Figure 4.24b, Table 4.1).

In addition to the loss of oxygen, the loss of fluorine is possible, which is why NRA measurements were carried out for the LCMOLiF10_1000 sample in comparison to the LCMOF10_700 sample. Figure 4.25 shows the measured spectra for both samples. In the interval 7400 to 8000 keV, the scattering and reactions of fluorine occur, which are not overlaid by the energy ranges of scattering and reactions of the other elements. As can be seen in the inset of Figure 4.25, α-particles which belong to the $^{19}F(p,\alpha_0)^{16}O$ nuclear reaction are measured. The occurrence of this nuclear reaction verifies the presence of fluorine in both samples. By fitting the spectrum with SIMNRA, the fluorine amount was quantified to a weight fraction of

0.8 ± 0.1 and 0.9 ± 0.1 wt.-% for LCMOLiF10_700 and LCMOLiF10_1000 respectively, which is close to the weighed amount of 0.8 wt.-% fluorine (according to 1 wt.-% LiF).

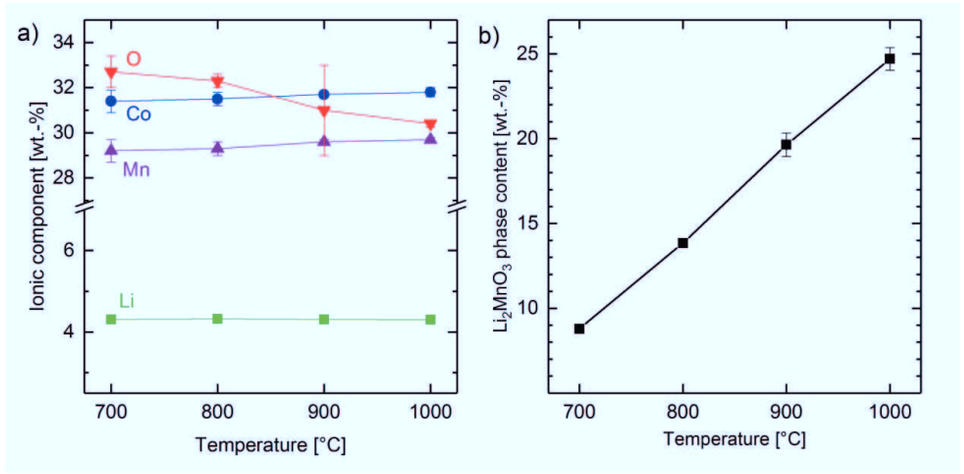

Figure 4.24: Changes in a) chemistry and b) weight fraction of the Li_2MnO_3 phase as a function of temperature in sintered LCMOLiF10 pellets.

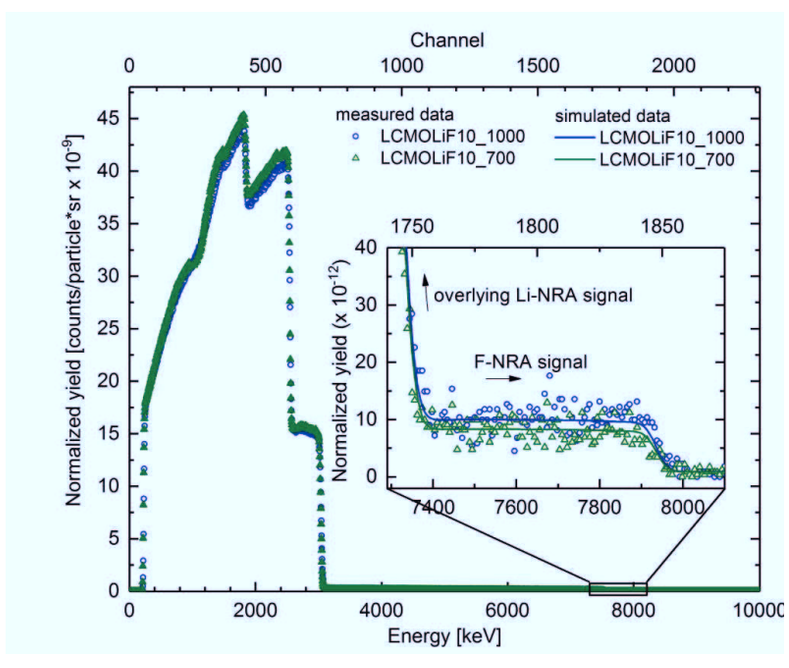

Figure 4.25: NRA measured and simulated data for LCMOLiF10_1000 and LCMOLiF10_700. The inset shows the not-overlain NRA data of fluorine. The yield was normalized to the particle*sr factor (=number of incident particles times the solid angle of the detector).

4.3.4 In-situ phase evolution as a function of temperature

To gain further insight into the evolution of crystalline phases during sintering, an in-situ high temperature XRD study was carried out for LCMO_pec and LCMOLiF10. Figure 4.26 shows the evolution of phases qualitatively. For LCMO_pec, the spinel peaks show a shift to lower angles, if the temperature is increased from 650 to 950 °C, implying larger lattice parameters at higher temperatures. A thermal expansion of the lattice is expected. However, the relative intensities of the main spinel reflections change upon heating, indicating a change in the stoichiometry of the spinel phase. The spinel *111* reflection is strongest at 650 °C and fades continuously until 950 °C. The *311* refection becomes the main reflection, as is typical for $(Co,Mn)_3O_4$ spinels [143,144]. At 850 °C another phase appears, which can be indexed to a (Li,Co,Mn)O phase in rocksalt configuration (space group *Fm-3m*). During cooling, this phase disappears again and the peaks of $LiCoMnO_4$ shift back to their original positions.

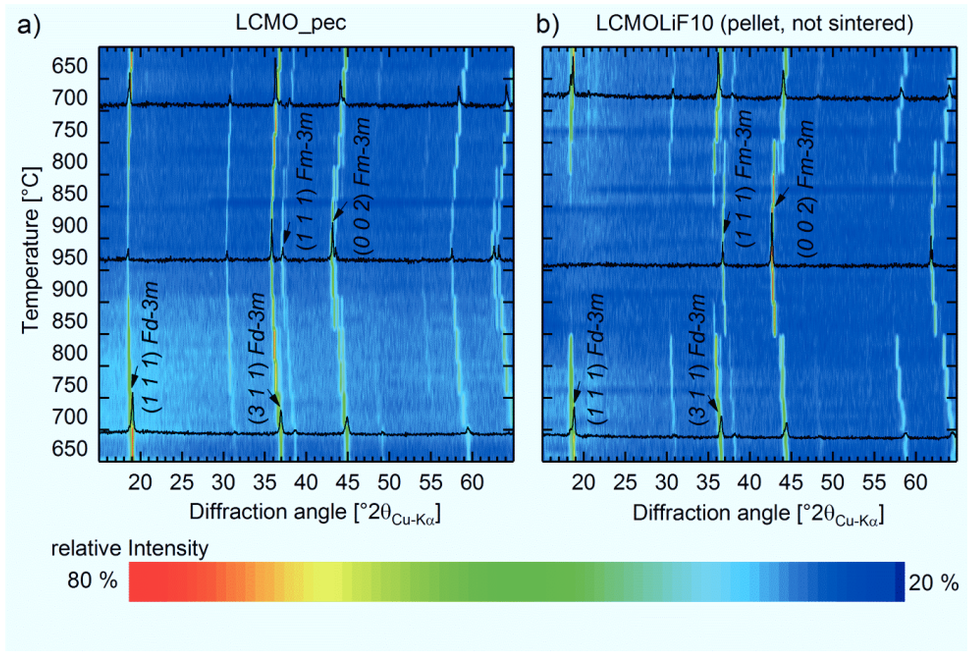

Figure 4.26: Color coded pseudo 3D diffractograms for the in-situ high temperature XRD for a) LCMO_pec and b) LCMOLiF10.

For the LCMOLiF10 sample, the phase evolution is different. From 650 to 850 °C the spinel peaks show a similar shift and change in relative intensities, as was ob-

served for the LCMO_pec sample. However, at 850 °C the spinel peaks disappear and the patterns show a contribution of the rocksalt-type phase only. Below 850 °C during cooling, the spinel phase is restored and no more peaks of the rocksalt phase are observed.

The presence of Li_2MnO_3, as suggested by the ex-situ XRD, is monitored by the in-situ measurement for LCMO_pec and LCMOLiF10 as well. For both samples Li_2MnO_3 is visible as a shoulder at the main spinel *111* refection. Especially in the cooling process from 800 to 650 °C, the relative intensity of this shoulder implies higher Li_2MnO_3 contents in the LCMOLiF sample than in the LCMO_pec sample.

Quantification of the occurring phases via Rietveld method allows a more detailed insight to the phase evolution during heating and cooling. Figure 4.27 summarizes the results of the quantitative phase analysis. The phase fractions in both samples are the same at the beginning of the measurement, which is around 10 wt.-% Li_2MnO_3 and 90 wt.-% $LiCoMnO_4$. For LCMO_pec, the Li_2MnO_3 content remains the same within the error of the measurement until 650 °C. From 650 to 800 °C, it increases from 10 wt.-% to 30 wt.-%, while the fraction of the spinel phase decreases. For temperatures higher than 800 °C, the rocksalt phase emerges and increases its weight fraction as the temperature increases, while the weight fractions for spinel and Li_2MnO_3 decrease. At 950 °C, the maximum temperature, no more Li_2MnO_3 can be detected, the rock salt phase is the main phase, and 40 wt.-% of the spinel phase is left. During cooling, the phase evolution displays a completely reversible trend. The room temperature scan after the measurement shows 10 wt.-% Li_2MnO_3 and 90 wt.-% $LiCoMnO_4$ again.

The first differences between the LCMO_pec and LCMOLiF10 sample are already apparent from the phase evolution in between 25 °C and 650 °C upon heating. The initial Li_2MnO_3 fraction of 10 wt.-% at 25 °C for LCMOLiF10 is doubled at 650 °C. From 650 °C to 800 °C the Li_2MnO_3 fraction increases to 50 wt.-%, leaving behind 50 wt.-% of spinel phase. For temperatures higher than 800 °C, no more Li_2MnO_3 can be detected. Instead, the rocksalt-type phase emerges as main phase at 850 °C with 90 wt.-%, while only 10 wt.-% of the spinel phase is left. No more spinel can be detected at 900 and 950 °C. The phase evolution is partially reversed upon cooling. At 25 °C, 15 wt.-% Li_2MnO_3 and 85 wt.-% $LiCoMnO_4$ are detected.

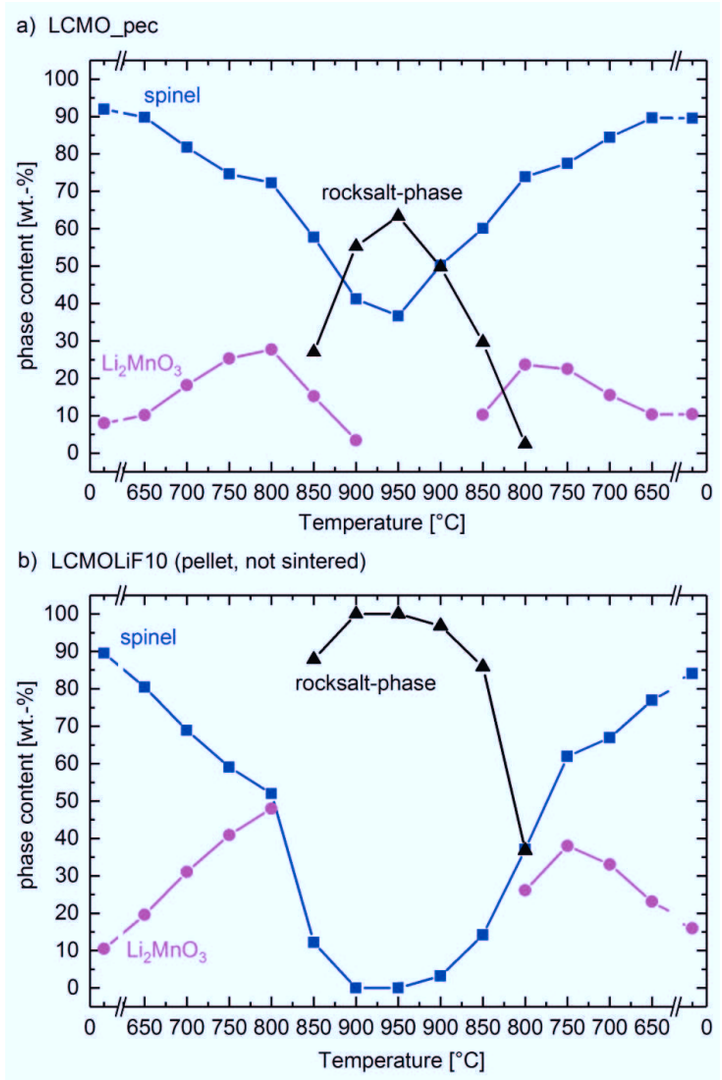

Figure 4.27: Quantification of phases from the in-situ high temperature XRD data.

4.3.5 Electrochemical activity

Figure 4.28 shows the CV diagrams for the LCMOLiF15_900 sample, after grinding and cathode-processing, compared with the LCMO_pec cathode obtained from Pechini synthesis, as described in section 4.1.2. Similar to LCMO_pec, the LCMOLiF15 sample shows the typical two-step redox reaction of the $Co^{3+/4+}$ redox reaction in $LiCoMnO_4$ in the high voltage region [136,145]. Additionally, the $Mn^{3+/4+}$ reaction at 3.9 to 4.0 V vs. Li/Li^+ [101] is measured for LCMOLiF15_900 as well.

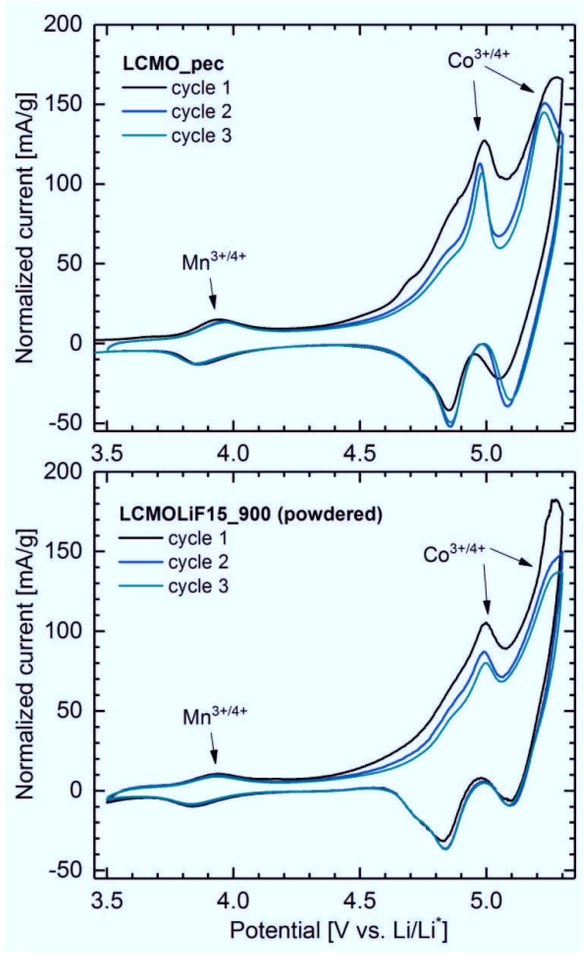

Figure 4.28: Cyclic voltammetry of LCMOLiF15_900 and pure LCMO_pec for comparison. Scan rate 0.1 mV/s.

4.4 Part IV: Synthesis and characterization of fluorinated $LiCoMnO_4$

This section presents the results on fluorinated $LiCoMnO_4$ powders to investigate possible impacts of fluorine insertion into the spinel lattice, as it might happen during sintering $LiCoMnO_4$ with LiF, on the properties and performance of $LiCoMnO_4$ cathodes.

4.4.1 Structure and chemistry of fluorinated $LiCoMnO_4$

The X-ray diffraction patterns of the synthesized LCMOF powders are given in Figure 4.29. All the powders show a main phase that was indexed to the cubic *Fd-3m* spinel structure [27,33], and a secondary phase which was indexed to a monoclinic Li_2MnO_3 - like phase in space group *C2/m* [128]. In Figure 4.29b, it can be seen that the *001* diffraction peak intensity of the Li_2MnO_3 phase decreases with increasing fluorine substituent, indicating a decreasing amount of the Li_2MnO_3 phase. The quantification of Li_2MnO_3 will be described in section 4.4.2.

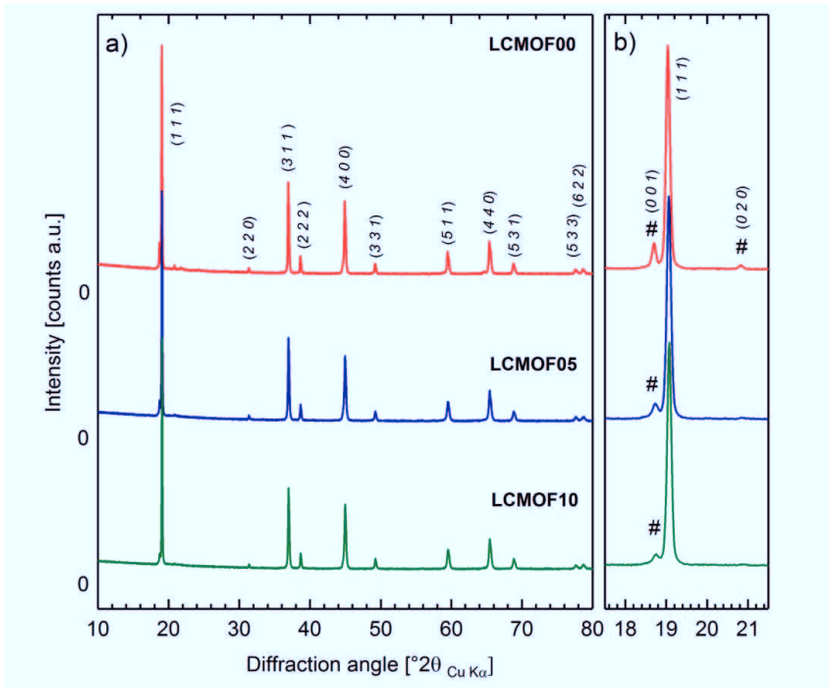

Figure 4.29: XRD result of LCMOF00, LCMOF05 and LCMOF10. a) full °2θ range, b) excerpt of data from 17.5-21.5°2θ. Main phase is indexed to *Fd-3m* [33] and secondary phase (#) was *C2/m*: Li_2MnO_3 [128].

The cation stoichiometry of all three samples according to the ICP-OES results is close to the weighed amount of cations (Table 4.2). The excess of lithium that was weighed is reflected in the ICP-OES results; hence there was only minor lithium loss during heat treatments. Nevertheless, lithium excess was reported to effectively reduce the concentration of transition metals on the tetrahedral sites of the spinel lattice, as well as to reduce the Mn^{3+} concentration, and to increase the specific capacity of the material [86]. Thus, the powders were accepted for further analysis despite their slight lithium excess. The measured oxygen content is clearly understoichiometric (Table 4.2), which will be discussed in 5.4.1. Furthermore, within the errors for this measurement, the same oxygen contents were measured for all three samples.

Table 4.2: Stoichiometry in mole per formula unit of LCMOF00, LCMOF05 and LCMOF10 samples derived from ICP-OES (Li, Mn Co), IFA (O) and NRA (F).

Sample	Li [mol] *	Mn [mol] *	Co [mol] *	O [mol] *	F [mol]**
LCMOF00	1.08 ± 0.02	0.97 ± 0.02	0.95 ± 0.02	3.57 ± 0.06	<0.001
LCMOF05	1.08 ± 0.03	0.97 ± 0.02	0.95 ± 0.02	3.56 ± 0.04	0.04 ± 0.01
LCMOF10	1.08 ± 0.02	0.97 ± 0.02	0.95 ± 0.01	3.56 ± 0.06	0.09 ± 0.01

*) calculated from the measured weight percentage by normalizing to overall cation mole fraction
**) calculated from the average fluorine content as measured by NRA

Figure 4.30 shows the measured NRA data for all three samples. The inset in Figure 4.30 shows the scattering and reactions of fluorine, which are not overlaid by the scattering and reactions of the other elements. In the interval 7400 to 7700 keV, the signal for the fluorine-free sample is only determined by the background signal, whereas the signals for the fluorinated samples exhibit increasing intensities with increasing amounts of fluorine substituent. Furthermore, the signals of the individual fluorinated samples display a maximum of intensity at higher energies of detected α–particles. Higher energy α-particles represent the near-surface region of the sample. Since a constant signal would be expected for a homogeneous depth profile of fluorine within the sample, the rising signal indicates fluorine enrichment towards the surface of the specimen.

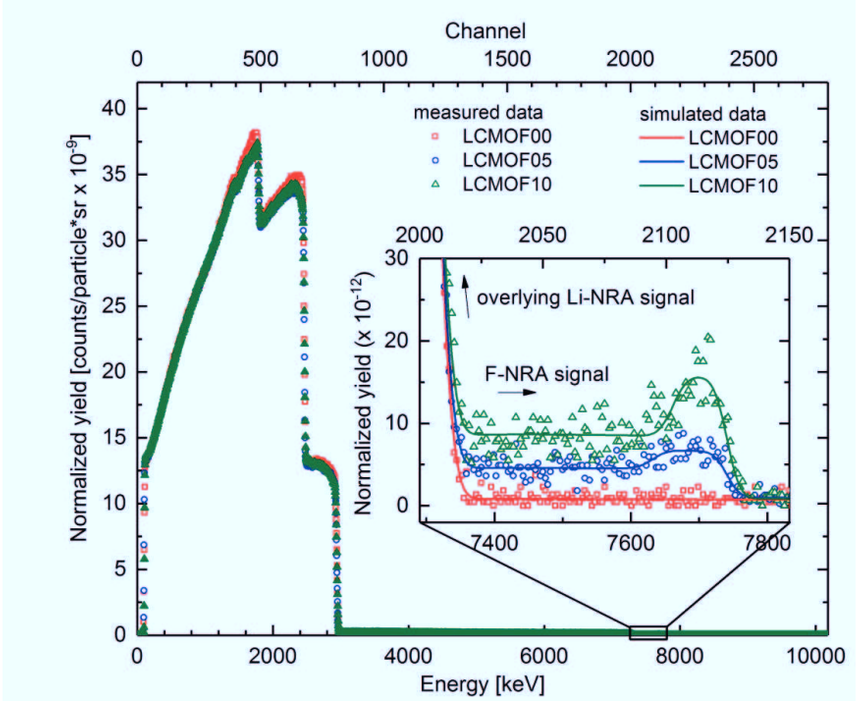

Figure 4.30: NRA measured and simulated data for LCMOF00, LCMOF05 and LCMOF10. The inset shows the not-overlain NRA data of fluorine. The yield was normalized to the particle*sr factor (=number of incident particles times the solid angle of the detector)

For fluorine quantification by SIMNRA, the inhomogeneous fluorine distribution was considered by simulating a two-layer system. In the model system, a fluorine-enriched “surface layer” and a “bulk layer” were chosen. Both bulk and surface layer together represent the complete probing depth. The best fit was achieved with a thin surface layer, which exhibits higher fluorine contents approximately twice as high as the bulk layer. The modeled surface layer thickness is about 2 % of the total probing range. Hence, the bulk layer dominates the properties of the model layer system and determines the average fluorine content. The overall fluorine stoichiometry of 0.04 and 0.09 mole per formula unit for LCMOF05 and LCMOF10, respectively, agrees with the expected values of 0.05 and 0.1 mol fluorine per formula unit (Table 4.2).

4.4.2 Crystallography and crystal chemistry of fluorinated $LiCoMnO_4$

Combined Rietveld refinement of neutron and synchrotron diffraction allowed for further investigation of the phase fraction of the spinel and secondary phase, the

lattice parameters, atomic positions, and site occupancies for the LCMOF00, LCMOF05 and LCMOF10 samples (Figure 4.31 and Figure 4.32). The lattice parameter of the main spinel phase was refined to a = 8.067 Å for the LCMOF00 sample, which is close to the reported lattice parameters in literature for $LiCoMnO_4$ [100]. The fluorinated samples show a slightly smaller lattice parameter of a = 8.0659 Å and a = 8.0652 Å for LCMOF05 and LCMOF10, respectively (Table 4.3). Monoclinic Li_2MnO_3-like phase in spacegroup *C2/m*, was identified from its *100*, *020*, *110*, *11-1* and *021* Bragg peaks. The amount of this secondary phase was quantified to 11 wt.-% for LCMOF00, 6 wt.-% for LCMOF05 and 4 wt.-% for LCMOF10 (Table 4.3 and Figure 4.33).

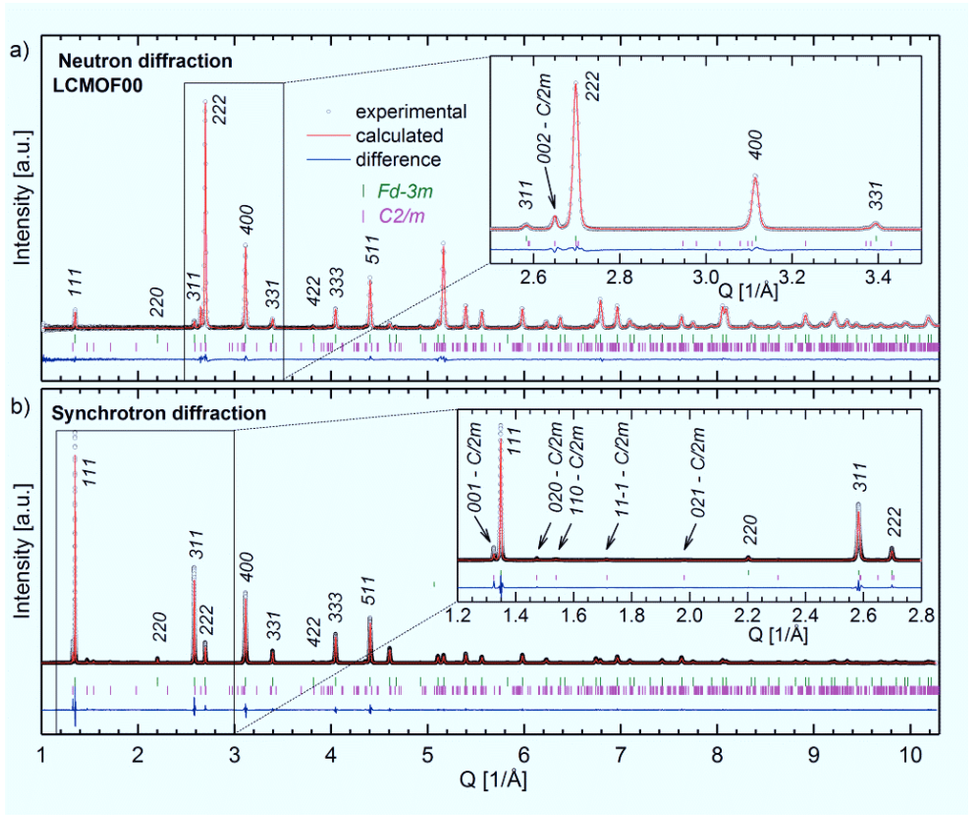

Figure 4.31: Combined Rietveld refinement of LCMOF00 a) Neutron diffraction (excerpt from 1 - 10.3 $Å^{-1}$, actual fitting range from 1 - 15 $Å^{-1}$), b) Synchrotron diffraction, full Q-range.

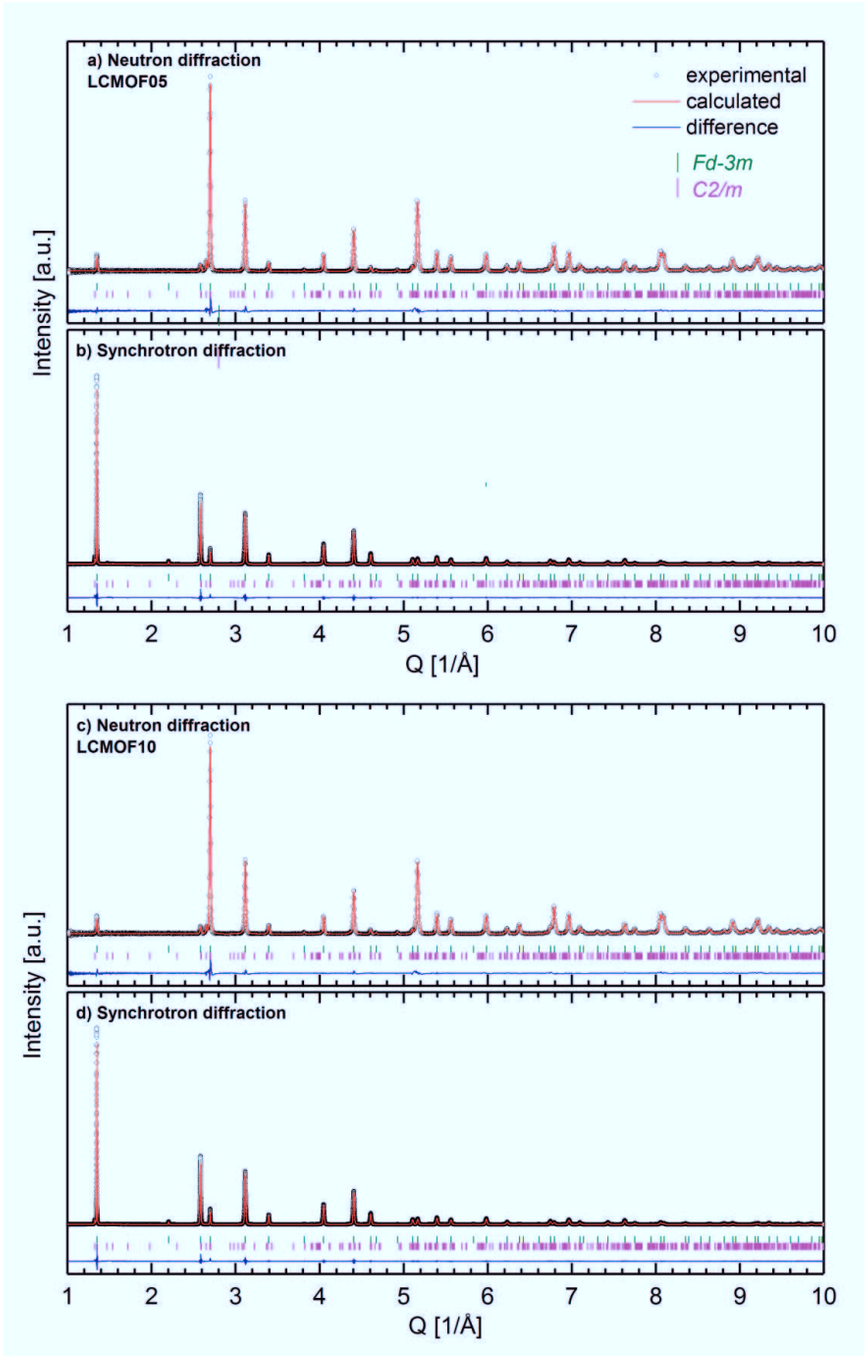

Figure 4.32: Combined Rietveld refinement of LCMOF05 a) Neutron diffraction (excerpt from 1 - 10 $Å^{-1}$, actual fitting range from 1 – 15 $Å^{-1}$), b) Synchrotron diffraction, full Q-range; and combined Rietveld refinement of LCMOF10 c) Neutron diffraction (excerpt from 1 – 10 $Å^{-1}$, actual fitting range from 1 – 15 $Å^{-1}$), d) Synchrotron diffraction, full Q-range.

Table 4.3: Lattice parameters, phase content, and goodness of fit obtained by the combined Rietveld refinement of LCMOF00, LCMOF05, and LCMOF10 based on neutron and synchrotron diffraction.

Sample	Lattice parameter of main phase [Å]	Amount of main phase [wt.-%]	Goodness of fit χ^2
LCMOF00	8.0670	89	7.6
LCMOF05	8.0659	94	5.3
LCMOF10	8.0652	96	5.3

Li_2MnO_3 is structurally related to $LiCoMnO_4$ spinel and most of its main Bragg peaks superimpose the spinel Bragg peaks. To eliminate false intensity contributions to the spinel Bragg peaks, it is important to describe the Li_2MnO_3 contribution to the pattern very carefully. However, Li_2MnO_3 is known to show stacking faults, which especially affect the peak intensity ratios and broadness of the *020*, *110*, *11-1*, *021*, and *111* reflections in the low Q-range from 1.4 to 2 $Å^{-1}$ [146].

To describe the peak profiles of Li_2MnO_3 in the neutron and synchrotron diffraction data, the profile functions were fixed at instrument resolution, with the addition of simple Lorentzian broadening for the X-ray data and quadratic broadening for the neutron data. This clearly led to an insufficient profile fit of the weak, asymmetric monoclinic Bragg peaks in the low Q-range, where the peak profiles display a Warren-type line shape as a result of stacking faults [147] (Figure 4.31). However, this provided an adequate fit to the more symmetric low Q-range *00l* reflections. As a result, Li_2MnO_3 Bragg peaks in the higher Q-range, where significant superimposition of spinel and monoclinic peaks occurred, can be described sufficiently well to provide an estimate of the phase fractions and refine the atomic parameters for the spinel phase.

The joint refinement of neutron and synchrotron data holds the advantage to investigate the cation distribution of the main phase very precisely, given the contrast of electron density for transition metal ions and lithium-ions for X-rays and the contrast of atomic scattering lengths for cobalt (b = 2.49 fm) and manganese (b = -3.73 fm) for neutrons [130]. Therefore, the site occupancy of lithium and cobalt cations on the tetrahedral *8a* site, as well as manganese and cobalt cations on the octahedral

16d site were refined constrained to full occupancy (i.e. occupancy Li + Co = 1 and Mn + Co = 1, respectively).

The distribution of fluorine and oxygen at the anionic *32e* site cannot be refined, since the electron density and the atomic scattering length for neutrons are similar for oxygen and fluorine. Thus, their contrast is too low to be distinguished. Therefore, the fluorine occupation was fixed to 0.01 and 0.0225 according to the quantification of fluorine contents by NRA, assuming that all fluorine is incorporated into the spinel phase. The oxygen occupancy parameter was found to be strongly correlated to the peak profile function parameters, the scale factors and atomic displacement parameters (*Uiso*). That is why the oxygen ion occupation parameter was first fixed to yield full occupation of the *32e* site (i.e. O + F = 1), while all other parameters were refined. After the fit had converged, all parameters were fixed and the oxygen occupancy was freed to converge.

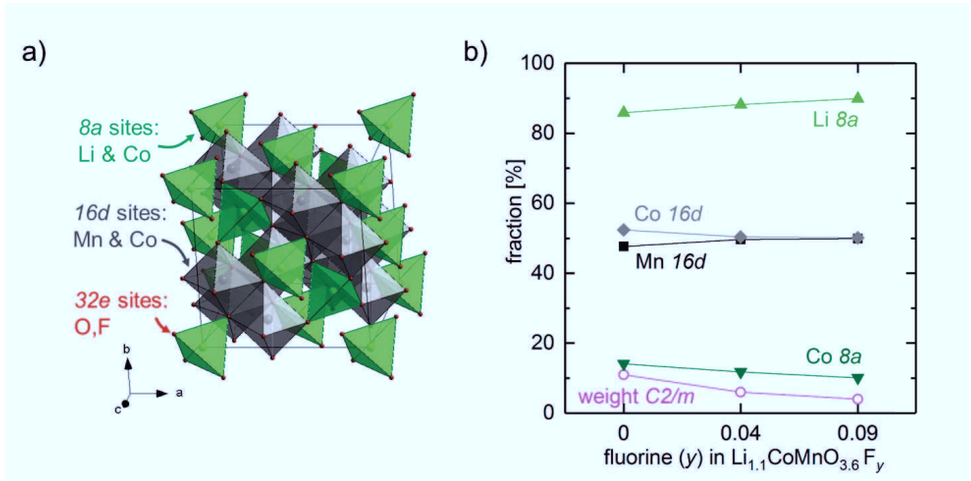

Figure 4.33. a) Visualization of spinel *Fd-3m* structure and cation distribution, b) cation distribution and phase content of Li_2MnO_3 (*C2/m*) as a function of fluorine content.

In Figure 4.33 and Table 4.4, the refined crystallographic data of the main phases in the samples are summarized. For all samples, the structural parameters converged to a very similar unit cell in terms of atomic positions: *8a* and *16d* Wyckoff positions are special positions and remain constant; the general *32e* oxygen atomic positions were refined freely and converged to relatively similar values of $0.2632 \pm 1 \times 10^{-5}$ for LCMOF00 and $0.2630 \pm 1 \times 10^{-5}$ for LCMOF05 and LCMF10.

Table 4.4: Structural parameters of spinel main phase obtained from Rietveld refinement of LCMOF00, LCMOF05 and LCMOF10. Space group *Fd-3m*, origin at *-3m.*

Sample	Wyckoff position	Atom type	Fractional coordinates, X=Y=Z	Site occupancy	Uiso*100 [nm²]
LCMOF00	*8a*	Li	0.125	0.8590(8)	0.82(3)
	8a	Co	0.125	0.1410(8)	0. 82(3)
	16d	Mn	0.500	0.4761(11)	0. 229(5)
	16d	Co	0.500	0.5239(11)	0. 229(5)
	32e	O	0.263175(14)	1.0*	0. 424(6)
LCMOF05	*8a*	Li	0.125	0.882(2)	0.85(3)
	8a	Co	0.125	0.118(2)	0.85(3)
	16d	Mn	0.500	0.496(2)	0.337(5)
	16d	Co	0.500	0.504(2)	0.337(5)
	32e	F	0.263	0.01	0.380(5)
	32e	O	0.263045(11)	0.99*	0.380(5)
LCMOF10	*8a*	Li	0.125	0.899(2)	0. 82(3)
	8a	Co	0.125	0.101(2)	0. 82(3)
	16d	Mn	0.500	0.499(2)	0. 281(4)
	16d	Co	0.500	0.501(2)	0. 281(4)
	32e	F	0.263	0.0225	0. 373(5)
	32e	O	0.263035 (10)	0.9775*	0. 373(5)

*) The oxygen ion occupation parameter was first fixed to yield full occupation of the *32e* site (i.e. O + F = 1), because of strong correlations to the peak profile function parameters, the scale factors, and atomic displacement parameters (*Uiso*).

The cation distributions on octahedral and tetrahedral sites show changes in dependence of the fluorine content, such that the occupation of cobalt cations on *8a* and *16d* sites decreases for higher fluorine contents in the samples. To be specific, LCMOF05 has two percentage points less cobalt cations at both, the *8a* site and the *16d* site compared to LCMOF00. LCMOF10 has two percentage points less cobalt cations at the *8a* site compared to LCMOF05, while the cation distribution at the *16d* site is similar within the errors of the refinement. In the subsequent refinement of the oxygen occupancy, the parameters shifted slightly away from their starting values to lower ones, i.e. 0.993 ± 0.001, 0.985 ± 0.001 and 0.972 ± 0.001

for LCMO00, LCMOF05 and LCMOF10 respectively. This corresponds to a shift of ~0.006 ± 0.001 for all samples.

Cubic spinel, in *Fd-3m* structure, possesses the O_h^7 spectroscopic symmetry and is expected to show five Raman active modes, as described in section 4.1.1. Furthermore, the secondary phase Li_2MnO_3, which is highly Raman active, is expected to show at least six Raman active modes [134]. Figure 4.34 shows the experimental and fitted Raman spectra based on the averaged and normalized data collected in an area of 60 µm × 100 µm. In the LCMOF00 sample, five bands corresponding to the expected modes for spinel are found at 650 (A_{1g}), 570 ($F_{2g}^{(1)}$), 535 ($F_{2g}^{(2)}$), 468 ($F_{2g}^{(3)}$), and 379 cm^{-1} (E_g). Five bands corresponding to Li_2MnO_3 are recorded at 613, 496, 438, 415, and 370 cm^{-1}, numbered from v_1 to v_5.

Furthermore, the spectrum of LCMOF00 shows a contribution of two low intensity bands that cannot be assigned to bands of spinel or Li_2MnO_3. These bands are centered at 594 cm^{-1}, visible as a shoulder at v_1, and at 692 cm^{-1}, visible as a shoulder at the high energy side of the A_{1g} mode. In literature, the latter one was found for a $LiCoMnO_4$ sample as well, where it was assigned to Co_3O_4 [148].

Upon fluorination, the positions of band centers do not show significant changes for neither the spinel nor the Li_2MnO_3 phase (Figure 4.34). However, the intensity contributions of both phases change. In the LCMOF00 sample, Li_2MnO_3 bands dominate the spectrum, i.e. the maximum intensity in the spectrum is recorded for the v_1 band of Li_2MnO_3. For the LCMOF10 sample on the other hand, the bands of the spinel phase are more dominant, i.e. the maximum intensity in the spectrum is recorded at 572 cm^{-1} for the $F_{2g}^{(2)}$ band of spinel. The trend of decreasing Li_2MnO_3 band intensities for higher fluorine contents agrees with the observation from powder diffraction, where less Li_2MnO_3 is detected upon fluorination.

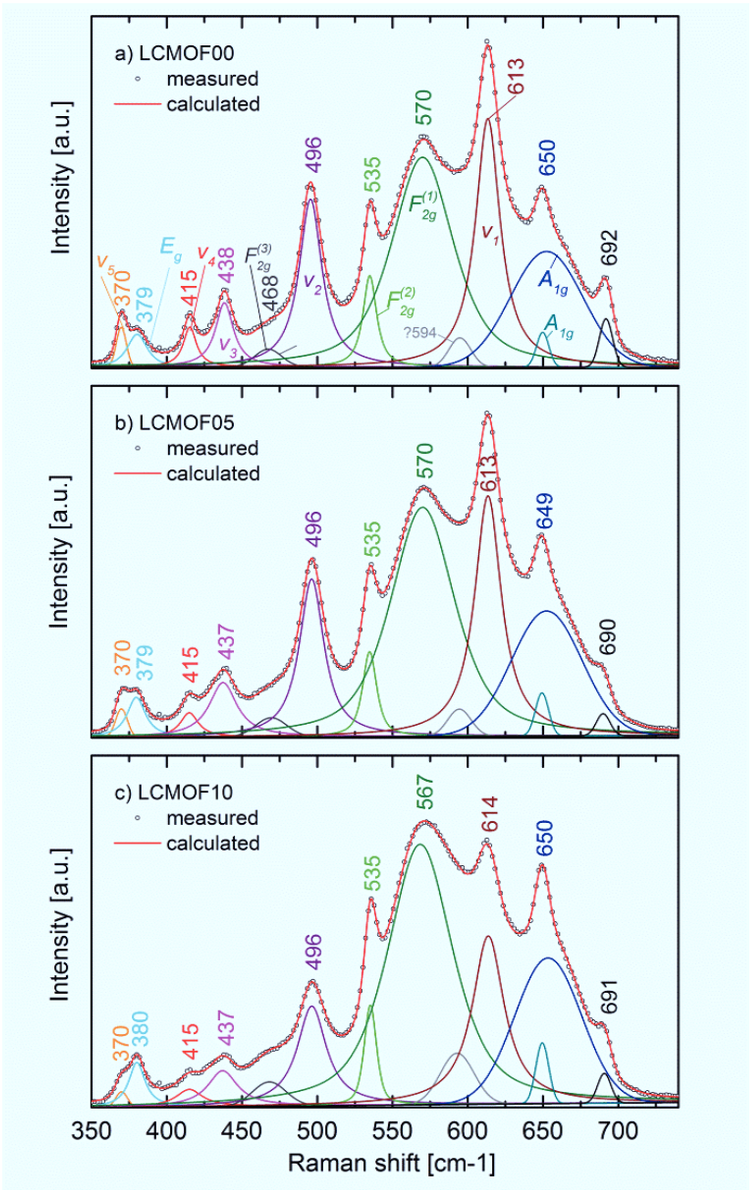

Figure 4.34: Results of the Raman mapping in an area of 100 × 60 µm. Averaged, normalized and fitted spectra for a) LCMOF00, b) LCMOF05 and c) LCMOF10. Color coding for bands in figure a is the same than in b and c.

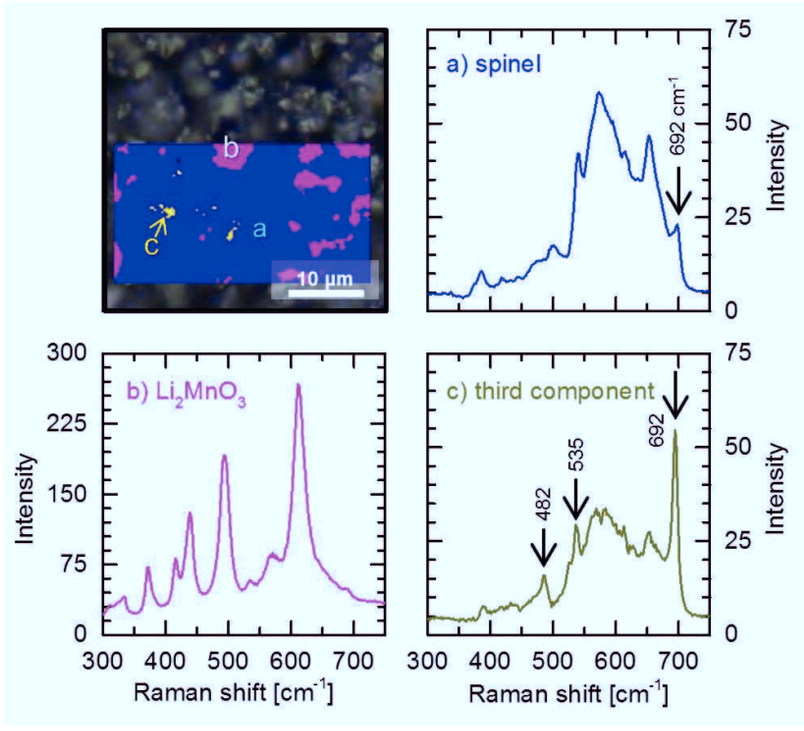

Figure 4.35: Component analysis results of the high-resolution micro Raman mapping of LCMOF00. Representative spectra of the individual components are given in a) for spinel, b) for Li_2MnO_3, and c) for a Co-rich component.

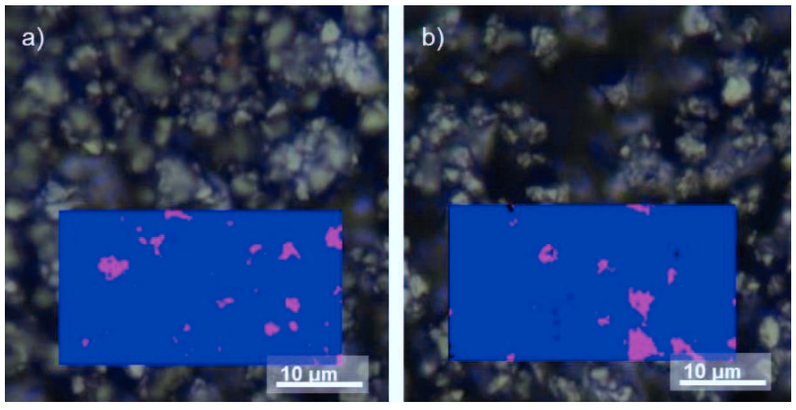

Figure 4.36: Component analysis results of the high-resolution micro Raman mapping of a) LCMOF05 and b) LCMOF10. The blue regions are spinel and the pink regions are Li_2MnO_3.

Although Li_2MnO_3 has a large contribution to the average spectra, the result of the high-resolution mappings clearly reveals spinel as the dominating phase throughout the samples (Figure 4.35 and Figure 4.36). Comparing the two representative spec-

tra for Li_2MnO_3 and spinel, in Figure 4.35a and Figure 4.35b, demonstrates that the maximum intensity of the Li_2MnO_3 spectrum is at least four times higher than the maximum intensity in the spinel spectrum. This observation explains the dominance of the Li_2MnO_3 phase in the average spectra in Figure 4.34. Furthermore, Li_2MnO_3 can clearly be identified as a separate phase in the micrometer length scale.

The recorded third component cannot be identified as an individual phase on this length scale. However, the presence of this third component can be recognized from its dominating band centered at 692 cm^{-1}. This band position is a fingerprint for Co_3O_4 and corresponds to its high intense A_{1g} mode. Two further low intense bands are expected for Co_3O_4 as well [149], which can be found at 535 and 485 cm^{-1}. Obviously, the Co_3O_4 spectrum is superimposed by the spectrum of the LCMOF spinel, which implies that the dimension of a separate Co_3O_4 phase is below the lateral resolution of the Raman microscope.

Figure 4.37 shows the band position of A_{1g} modes of lithium manganese based spinels as a function of the average ionic radius of the octahedrally coordinated transition metals in various spinels. The band position of the A_{1g} mode was shown to shift to higher wavenumbers, if the average ionic radius of the transition metals in the octahedron gets lower [133].

The shift of the A_{1g} mode is directly caused by a decreased bond length, leading to a higher frequency of the vibrational mode. The displayed averaged radii of the transition metals on the octahedral site belong to the compounds $LiMn_2O_4$ (Mn^{3+} : Mn^{4+} = 1 : 1) [131], $LiNi_{0.5}Mn_{1.5}O_4$ (Ni^{2+} : Mn^{4+} = 0.5 : 1.5) [133], $LiCo_{0.5}Mn_{1.5}O_4$ (Co^{3+} : Mn^{3+} : Mn^{4+} = 0.5 : 0.5 : 1) [133] and $LiCoMnO_4$ (Co^{3+} : Mn^{4+} = 1 : 1)[100,117]. The ionic radii were taken from Shannon [132]. For the LCMOF samples, an average radius of 0.543 Å is assumed (according to a ratio of Co^{3+} : Mn^{3+} : Mn^{4+} = 1 : 0.1 : 0.9), as will be discussed later. All three samples share a very similar Raman band position of the A_{1g} mode and are consistent with the trend derived from literature.

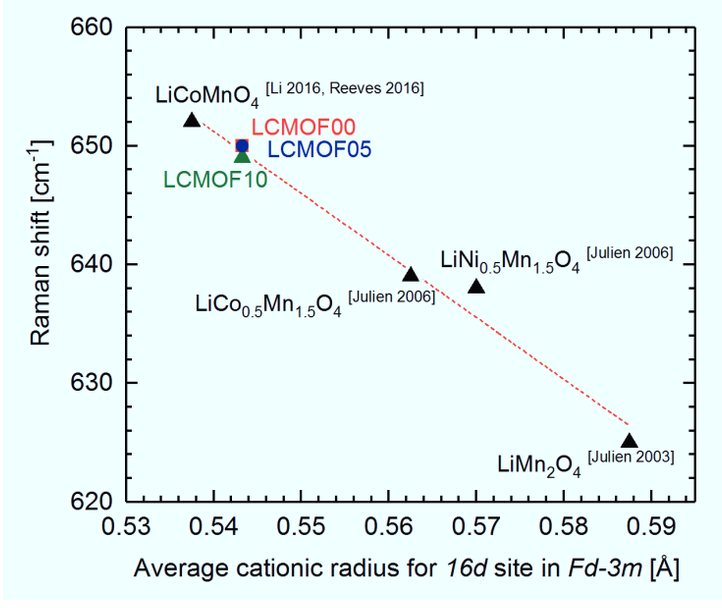

Figure 4.37: Correlation of the position of the band center of the A_{1g} mode to the average ionic radius of the transition metal cations on the octahedral site in lithium manganese based spinels (space group *Fd-3m)*. Literature data for $LiMn_2O_4$ [131], $LiNi_{0.5}Mn_{1.5}O_4$, $LiCo_{0.5}Mn_{1.5}O_4$ [133], and $LiCoMnO_4$ [100,117].

4.4.3 Microstructural properties

The synthesized powders were investigated by SEM (Figure 4.38) with respect to their microstructure and particle morphology. In general, the LCMOF00 sample appears to have a larger variety of particle sizes from smaller than 1 µm up to 6 µm, whereas the fluorinated samples show a narrower particle size distribution with 1 µm to 3 µm particles. Moreover, a change in particle morphology can be observed from non-fluorinated to fluorinated samples. On the one hand, for the LCMOF00 sample, large crystallites with a typical (111) plane-faceted habitus can be easily identified next to smaller particles with unidentified habitus. The fluorinated samples, on the other hand, show a larger degree of sintering rather than crystallization. Single crystallites can be identified less easily. For those that are identified, the development of (100) crystal planes can be observed besides the typical (111) crystal planes, leading to a more compact crystal habitus. Thus, the microstructure of the powders changes from well-crystallized larger particles to smaller truncated and partially sintered agglomerates upon fluorine incorporation.

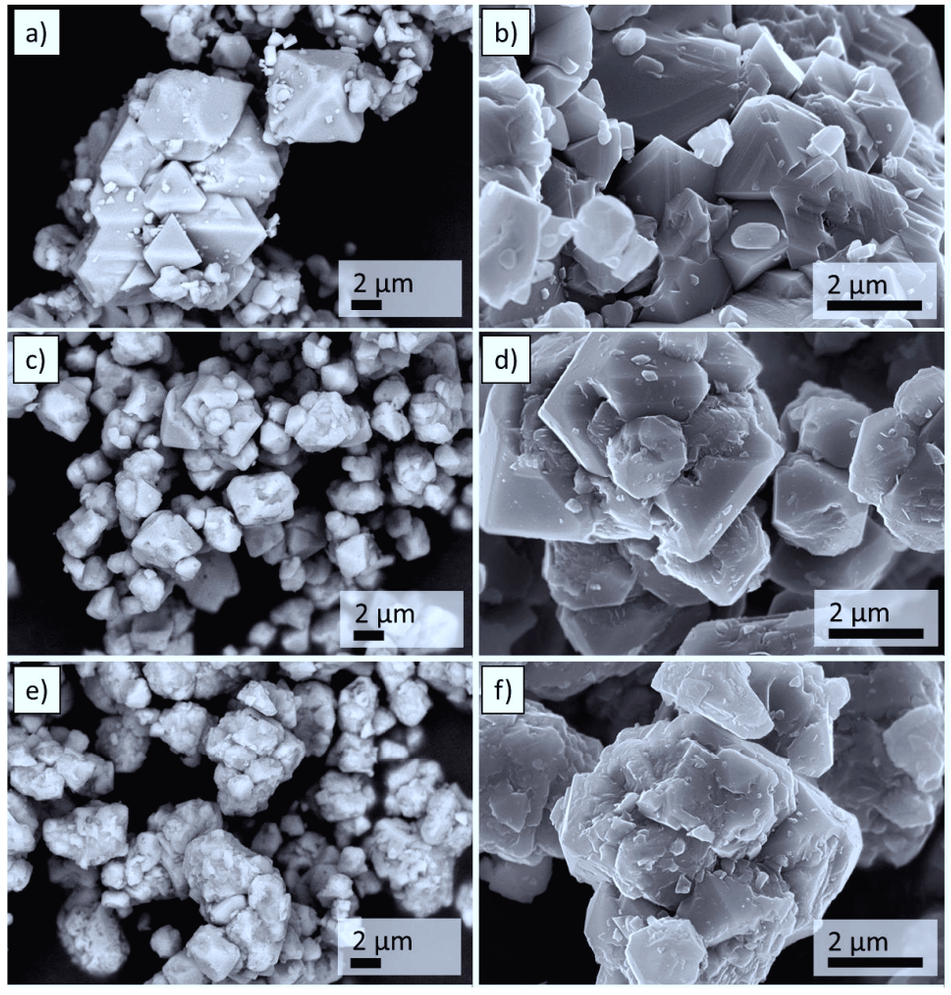

Figure 4.38: SEM images of (a)+(b) LCMOF00, (c)+(d) LCMOF05 and (e)+(f) LCMOF10.

4.4.4 Electrochemical properties

Figure 4.39a shows the second cycle of the cyclic voltammetry curves of the three materials studied. All the samples display a two-step electrochemical reaction near 4.9 and 5.2 V vs. Li/Li^+ during charging and discharging, agreeing with the $Co^{3+/4+}$ oxidation and reduction, respectively [106]. Besides the common double-peak characteristics, all three samples also show a shoulder on the first $Co^{3+/4+}$ reaction peak near 4.8 V vs Li/Li^+, as was observed for the LCMO_pec and LCMOLiF15_900 sample as well and was previously shown to be characteristic of

the electrochemical reaction of slightly non-stoichiometric $LiCoMnO_4$ materials [101].

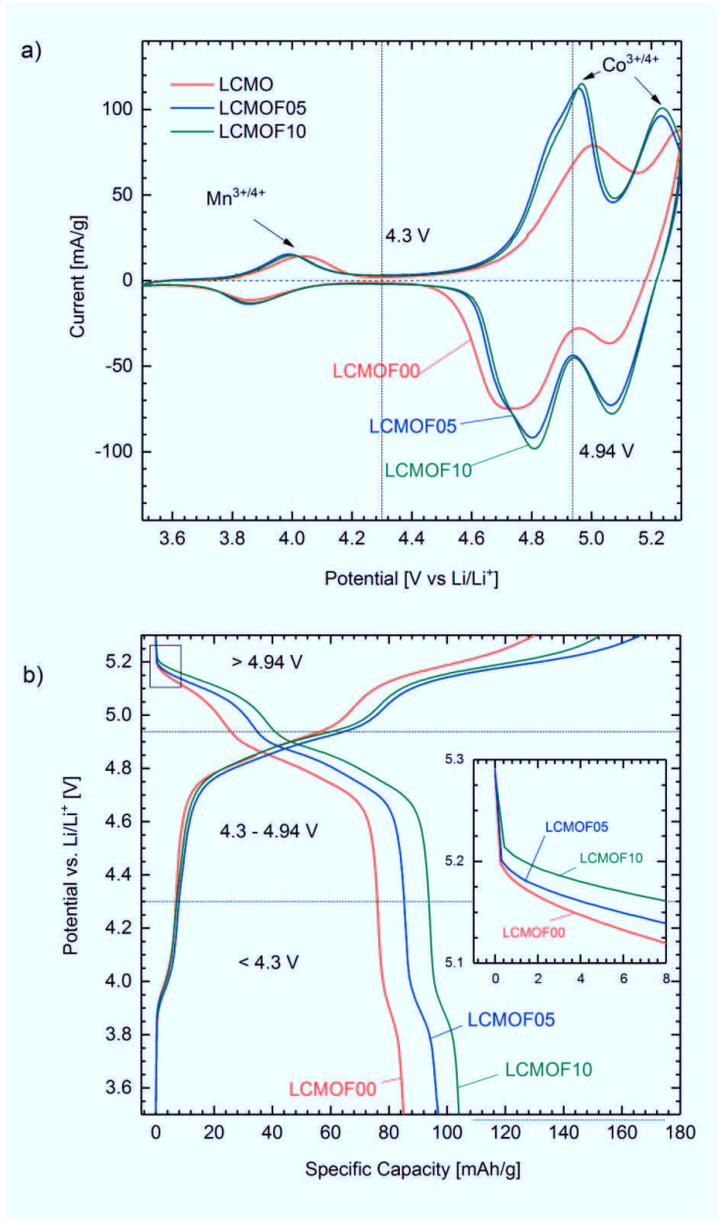

Figure 4.39: a) CV results of 2nd cycle for LCMOF00, LCMOF05 and LCMOF10. **b)** Charge-discharge curves of the 2nd cycle for LCMOF00, LCMOF05 and LCMOF10.

Additionally, weak electrochemical activity was measured at 3.9 to 4.0 V vs. Li/Li^+ for all three samples, which can be attributed to the $Mn^{3+/4+}$ redox couple in spinels [101]. Ideally, $LiCoMnO_4$ should not contain any Mn^{3+}. The detection of the $Mn^{3+/4+}$ redox couple in oxygen non-stoichiometric $LiCoMnO_{4-\delta}$ is consistent with previous studies [15,100]. Furthermore, the $Mn^{3+/4+}$ reaction peak intensities appear similar for all the three samples. The intensities of the $Co^{3+/4+}$ reactions, on the other hand, show slightly increasing intensities with increasing fluorine content. Consequently, the ratio of Co^{3+} to Mn^{3+} redox activity is higher for higher amounts of fluorine substituent.

In contrast to LCMOF05 and LCMOF10, LCMOF00 shows a higher asymmetry between the oxidation and reduction processes. The peak electrochemical reactions were shifted to higher (for oxidation) or lower (for reduction) values due to higher ohmic resistance.

Figure 4.39b shows the charge and discharge curves in the second cycle for LCMOF00, LCMOF05 and LCMOF10. Three plateaus can be identified upon charging and discharging, in coherence to the reactions found in CV. A small plateau can be seen at around 4.0 V vs. Li/Li^+, corresponding to the $Mn^{3+/4+}$ reaction, in the charge and discharge curves, respectively. The second and third plateau can be found at around 4.8 and 5.1 V vs. Li/Li^+, which correspond to the $Co^{3+/4+}$ reaction. The discharge capacity in the second cycle is recorded as 85.1, 97.0 and 104.0 $mAhg^{-1}$ for LCMOF00, LCMOF05 and LCMOF10, respectively. Thus, the specific capacity of LCMOF10 in the second cycle is 18 % higher than that of LCMOF00.

Assuming that below 4.3 V vs. Li/Li^+ only $Mn^{3+/4+}$ contributes to the capacity and above only $Co^{3+/4+}$, the contribution of Mn^{3+} to the total discharge capacity is similarly low for all samples. The capacities below 4.3 V vs. Li/Li^+ are 9.1, 11.5 and 10.3 $mAhg^{-1}$ for LCMOF00, LCMOF05 and LCMOF10 respectively. Thus, around 11 % of the total discharge capacity can be attributed to the $Mn^{3+/4+}$ reaction.

The discharge capacities that originate from the reduction reaction of $Co^{3+/4+}$ can be separated into two parts, i.e. above 4.94 V vs. Li/Li^+ and in between 4.3 and 4.94 V vs. Li/Li^+. The lower limit, 4.3 V vs. Li/Li^+, is determined from the offset of the $Mn^{3+/4+}$ reaction in the CV scan and the upper limit, 4.94 V vs. Li/Li^+, is determined

from the local maximum between two reduction peaks of $Co^{3+/4+}$ in the CV scan (Figure 4.39a). The resulting capacities in between 4.3 and 4.94 V vs. Li/Li^+ are calculated to be 50.6, 50.6 and 53.0 $mAhg^{-1}$ for LCMOF00, LCMOF05 and LCMOF10, respectively. Thus, the difference in the total discharge capacities for the prepared materials mainly arises from the discharge capacities above 4.94 V vs. Li/Li^+.

The total charge capacities are recorded as 130.0, 166.5 and 152.6 $mAhg^{-1}$ for LCMOF00, LCMOF05 and LCMOF10, respectively. However, the charge capacities below 4.94 V vs. Li/Li^+ are only 56.8, 65.0 and 60.2 $mAhg^{-1}$. The total coulombic efficiencies are 65.5 %, 58.2 % and 68.2 %. Thus, most of the charge consumption, leading to the low coulombic efficiencies, takes place in the voltage region above 4.94 V vs. Li/Li^+.

The initial voltage drop shows different characteristics for all the three different samples as shown in the inset in Figure 4.39b. LCMOF00 shows the strongest drop, from 5.3 to 5.19 V vs. Li/Li^+, whereas LCMOF05 drops to 5.20 V vs. Li/Li^+ and LCMOF10 drops to 5.21 V vs. Li/Li^+. Additionally, the slope of the discharge curves in between 5.2 and 4.94 V vs. Li/Li^+ for LCMOF05 and LCMOF10 is lower than that for LCMOF00.

The cycling performances between 3.5 and 5.3 V vs. Li/Li^+ at a C/5 C-rate are given in Figure 4.40. The measured discharge capacity increases with increasing fluorine substituent. The highest specific capacity was recorded in the 2^{nd} cycle. After the second cycle, the reversible capacity of all three samples starts to degrade. Nevertheless, the degradation of the discharge capacity over cycling is slower for fluorinated samples. After 50 cycles, a degradation of 40.1 % for LCMOF00 was measured, whereas 29.6 % and 20.4 % degradation was observed for LCMOF05 and LCMOF10, respectively.

The capacity retention of each cycle, given by the ratio of the discharge capacity in the $(n+1)^{th}$ to the n^{th} cycle, which defines the retention of Li-ions in the active electrode material, is around 100 % for all three materials. However, the coulombic efficiency is lower than 80 % for all the measured cycles. In the first cycles, the coulombic efficiencies of LCMOF00 and LCMOF05 were as low as 50 %. The difference between the capacity retention per cycle and the coulombic efficiency yields the factor of charge consumption by liquid electrolyte decomposition in each

cycle [110]. Thus, up to 50 % of the charge was consumed by liquid electrolyte decomposition in the first cycles and 20 % in each higher cycle. Liquid electrolyte consumption might also lead to the observed data scattering after 40 cycles.

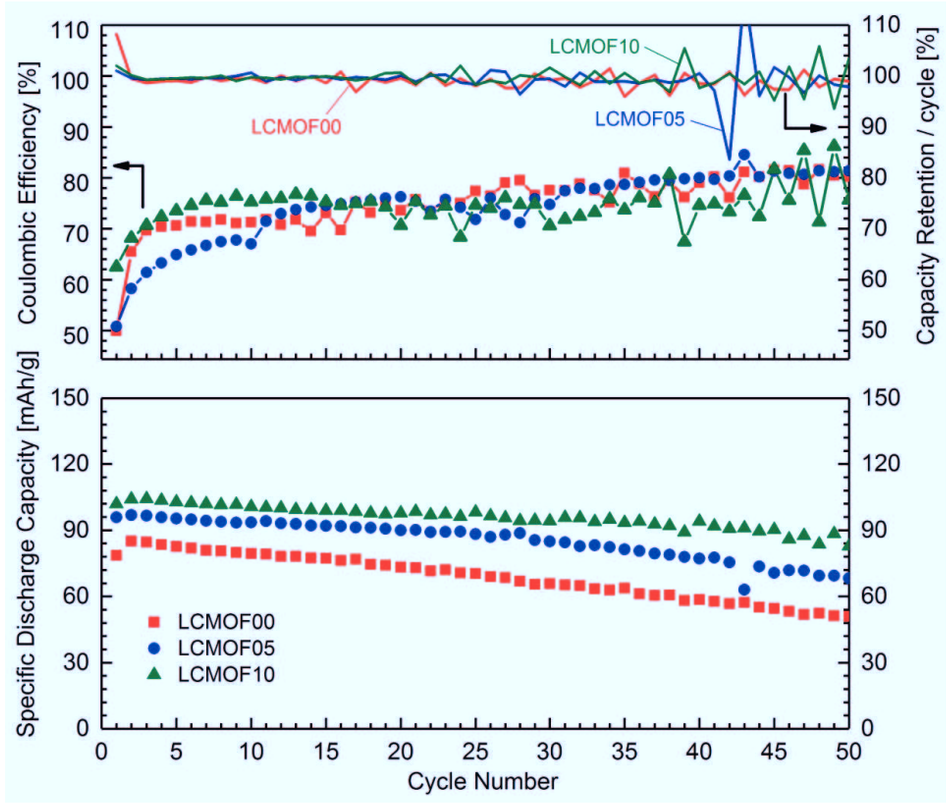

Figure 4.40: Specific discharge capacity, capacity retention and efficiency for LCMOF00, LCMOF05 and LCMOF10.

The rate capability tests, carried out at the same C-rate for charging and discharging, are shown in Figure 4.41. LCMOF10 always exhibits the highest capacity at different tested C-rates whereas LCMOF00 displays the lowest. The capacity retention at C/5 after cycling at elevated C-rates is around 90 % for all three materials.

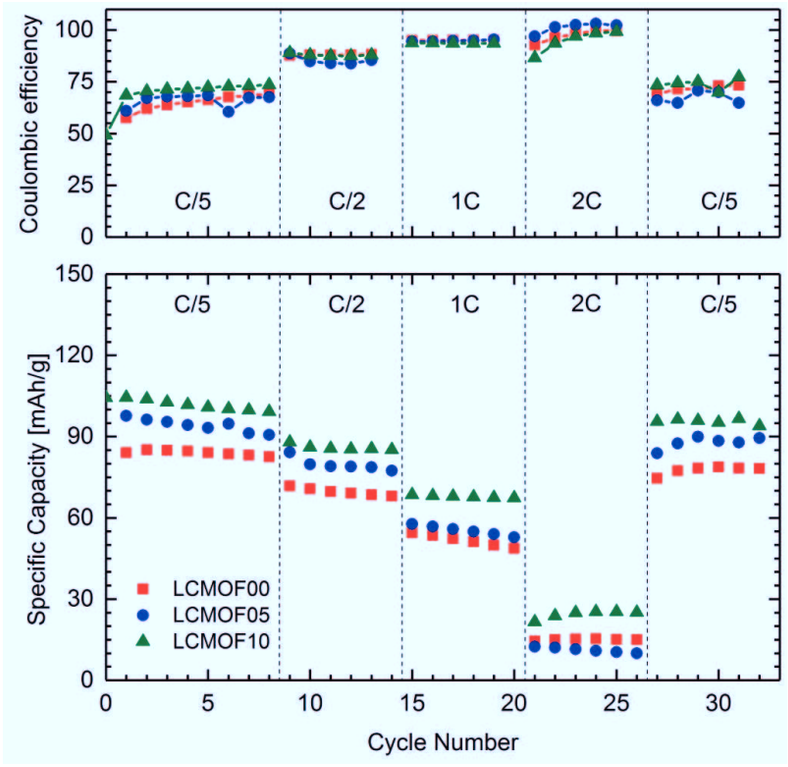

Figure 4.41: Rate capability testing for LCMOF00, LCMOF05 and LCMOF10.

Figure 4.42 shows the results of cyclic voltammetry at different scan rates. Three oxidation and reduction reactions are recorded, which are centered at 3.9, 4.9 and at 5.1 V vs. Li/Li^+, belonging to the $Mn^{3+/4+}$ reaction (at 3.9 V vs Li/Li^+) and the $Co^{3+/4+}$ reaction (at 4.9 and 5.1 V vs. Li/Li^+), as described above (Figure 4.39a).

With increasing scan rates, increasing peak current densities for all the samples are observed. This behavior is expected, since the time for charge transfer decreases for higher scan rates (according to I = Q/t). While the peak currents for peak 1, at 4.0 V vs. Li/Li^+, and peak 2, at 4.9 V vs. Li/Li^+, clearly display the expected behavior, peak 3 at 5.1 V vs. Li/Li^+ behaves differently: the forward peak current rises, while the reverse peak current decreases with increasing scan rates.

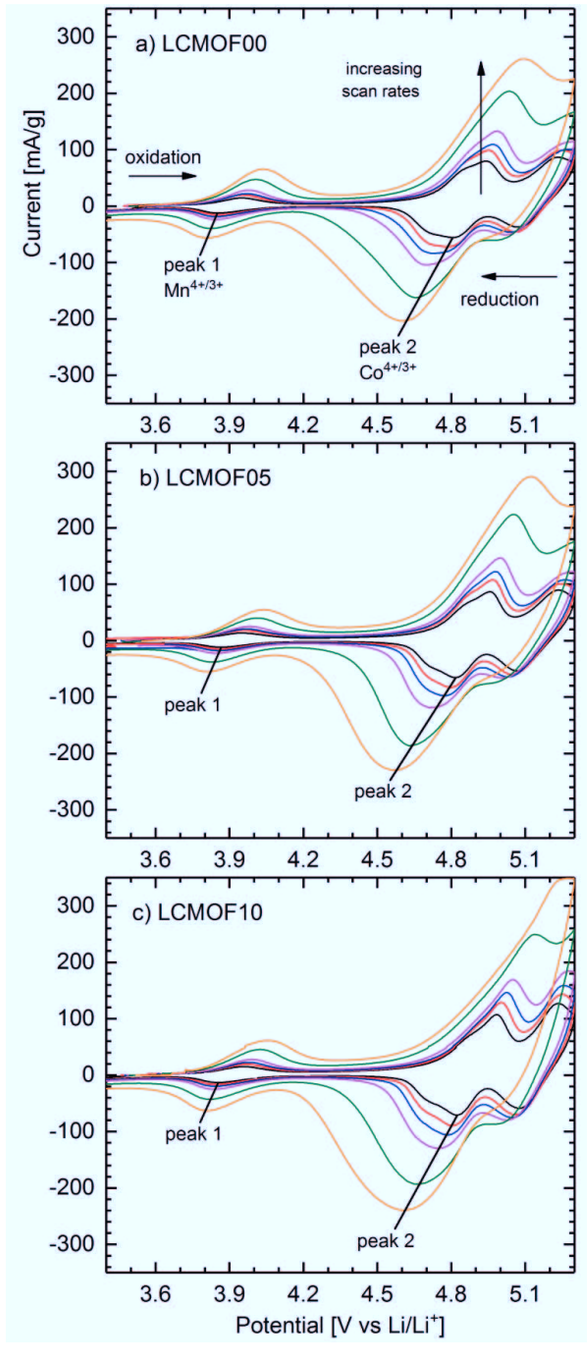

Figure 4.42: Cyclic voltammetry of LCMOF00, LCMOF05 and LCMOF10 at different scan rates: 0.1, 0.13, 0.16, 0.21, 0.4, and 0.65 mV/s.

Peak 3 behaves differently, because the oxidation reaction of Co^{3+} to Co^{4+} is not completed yet at the cut-off voltage (5.3 V vs. Li/Li^+). This effect gets more and more severe for the higher scan rates, where less time for Li-ion diffusion is given. As a consequence, the peak current densities for peak 3 in the reduction path decrease for higher scan rates. The cut-off voltage could not be raised beyond 5.3 V vs. Li/Li^+, due to the instability of the liquid electrolyte in the high voltage region [8].

For a CV scan, the integral of the oxidation and reduction current over the oxidation and reduction time gives an approximation of the capacity of a sample during discharge and charge, respectively. It is observed that the integrals of the oxidation and reduction curves are highest for LCMOF10 and lowest for LCMOF00 for all scan rates. This agrees with the results from the direct measurement of capacities the galvano-static charge discharge experiment, where 18 % higher discharge capacities were recorded for LCMOF10 compared to LCMOF00.

A possible reason for the increased capacity could be an improved Li-ion mobility in the fluorinated spinels, which allows for a faster diffusion and effectively more Li-ion extraction before the cut-off voltage is reached. To investigate the Li-ion mobility, the Randles-Sevcik equation was applied. According to the Randles-Sevcik equation (Equation 4.1), the peak current of a certain redox peak in a CV experiment is proportional to the square root of the diffusion coefficient (D) and the square root of the scan rate (υ) [145]:

$$I_p = 2.67 \cdot 10^5 \cdot An^{1.5} C_0 D^{0.5} \upsilon^{0.5} \tag{4.1}$$

Here, A is the surface area of the electrode in cm^2, n is the number of electrons involved in one single reaction and C_0 the concentration of Li-ions at the respective reaction center in $mol \cdot cm^{-3}$. The unit of the constant is $C^{1.5} J^{-0.5} mol^{-1}$.

A first comparison of the Li-ion mobility in the different samples is given by the discharge peak current density as a function of the square root of the scan rate. In Figure 4.43, the linear regression of I_p *vs.* $\upsilon^{0.5}$ is displayed for the peaks centered at 4.0 V vs. Li/Li^+ (peak 1) and 4.9 V vs. Li/Li^+ (peak 2). Peak 3 is not evaluated, because of the incomplete reaction at 5.1 V vs. Li/Li^+, as a reason of the low cut-off voltage, as explained before.

It is observed that the slopes of the linear regression lines for peak 2 are significantly higher than those for peak 1. Furthermore, the lines for peak 1 display very similar slopes for all samples, whereas peak 2 shows a trend of increasing slopes in the following order: 9.7 $As^{0.5}V^{-0.5}g^{-1}$ (LCMO00) < 10.7 $As^{0.5}V^{-0.5}g^{-1}$ (LCMOF05) < 10.9 $As^{0.5}V^{-0.5}g^{-1}$ (LCMOF10).

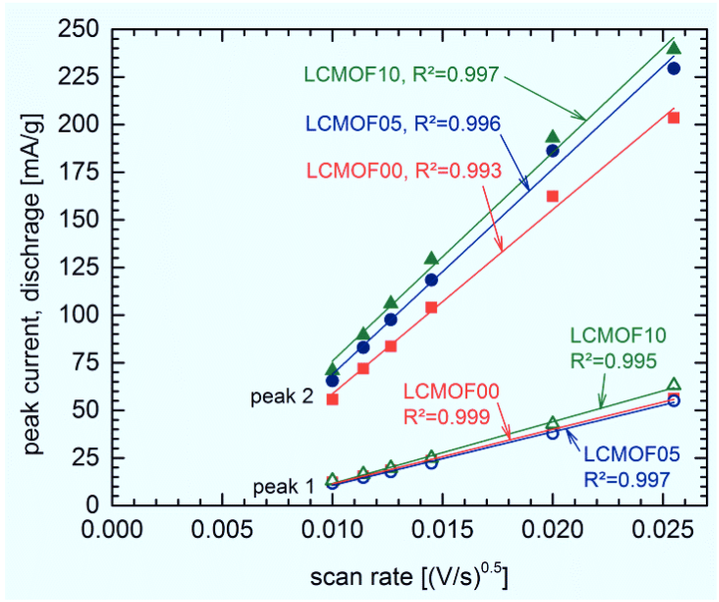

Figure 4.43 Linear regression of square root of CV scan rate and the peak current for peak 1 (centered at 3.9 V vs. Li/Li+) and peak 2 (centered at 4.9 V vs. Li/Li+).

If *A* and C_0 are known, Li-ion diffusion coefficients can be calculated from equation 4.1. In here, *A* is approximated from the experimental set-up by 1 cm². C_0 is approximated by the discharge capacity at the respective voltage (according to Figure 4.39b), assuming that for every electron transferred, a Li-ion will be inserted into the structure. The calculated values for C_0 and *D* are given in Table 4.5.

As a result, very similar Li-ion diffusion coefficients are calculated for peak 1 ($Mn^{3+/4+}$), namely 6 × 10^{-13} cm^2s^{-1} for LCMOF00, 7 × 10^{-13} cm^2s^{-1} for LCMOF05, and 9 × 10^{-13} cm^2s^{-1} for LCMOF10. For peak 2 ($Co^{3+/4+}$), the calculated Li-ion diffusion coefficients display slightly increasing values: LCMOF00 (1.37 × 10^{-11} cm^2s^{-1}) < LCMOF05 (1.79 × 10^{-11} cm^2s^{-1}) < LCMOF10 (1.86 × 10^{-11} cm^2s^{-1}).

Table 4.5: Calculated concentration of Li-ions (C_0) and Li-ion diffusion coefficients (D) at peak 1 and peak 2 for LCMOF00, LCMOF05 and LCMOF10.

Sample	Concentration of Li-ions at 4.0 V vs. Li/Li^+ (C_0) [$mol \cdot cm^{-3}$]	Concentration of Li-ions at 4.9 V vs. Li/Li^+ (C_0) [$mol \cdot cm^{-3}$]	Li-ion diffusion coefficient at 4.0 V vs. Li/Li^+ (D) [$cm^2 s^{-1}$]	Li-ion diffusion coefficient at 4.9 V vs. Li/Li^+ (D) [$cm^2 s^{-1}$]
LCMOF00	0.0303	0.0216	6×10^{-13}	1.37×10^{-11}
LCMOF05	0.0291	0.0220	7×10^{-13}	1.79×10^{-11}
LCMOF10	0.0297	0.0228	9×10^{-13}	1.86×10^{-11}

5 Discussion

5.1 Part I: $LiNi_{0.5}Mn_{1.5}O_4$, $LiFe_{0.5}Mn_{1.5}O_4$ and $LiCoMnO_4$ single materials properties

5.1.1 Structural and electrochemical aspects

All spinel samples can be synthesized via Pechini synthesis within two steps of heat treatment at 650 °C with ball milling in between. Phase pure $LiNi_{0.5}Mn_{1.5}O_4$ spinel was obtained after ball milling and annealing for 10 h at 650 °C, as was shown by XRD in Figure 4.2. This long annealing time is necessary to guarantee oxygen uptake and transformation of low-oxygen content rocksalt phases ($Li(Ni,Mn)O_2$) into the high oxygen containing spinel phase, in coherence to the results from Pasero *et al*. [82].

The LNMO_pec sample showed more bands in its Raman spectrum (Figure 4.4c), than expected for a spinel in *Fd-3m* structure. The additional observed bands can only arise from a symmetry reduction from the cubic face centered *Fd-3m* spinel structure to the cubic primitive superstructure $P4_332$, due to ordering of Mn- and Ni-ions at the octahedral site [81,133]. For a high degree of ordering, i.e. over a long range, it would be expected that superstructural Bragg reflections, belonging to the primitive lattice, are detected via XRD [30,31]. Low intense superstructural Bragg reflections belonging to $P4_332$ were detected via XRD for highly ordered $LiNi_{0.5}Mn_{1.5}O_4$ based on a Cu-Kα source before [81,150,151]. Since there were no such peaks detected for LNMO_pec (Figure 4.2), it has to be concluded that the degree of cation order is low, i.e. cation ordering does not happen over a long range.

The degree of cation order is known to be correlated to the Mn^{3+} content. In absence of the Mn^{3+} cation, the Ni^{2+} and Mn^{4+} cations exhibit the maximum order at the octahedral sites due to their large differences in ionic radii (0.69 Å vs. 0.53 Å) [80]. If oxygen is lost during synthesis and Mn^{4+} is partially reduced to Mn^{3+}, the Mn^{3+} ion induces disorder, i.e. the distribution of Mn- and Ni-ions at the octahedral sites become more statistical, which weakens the intensity of the superstructural Bragg reflections [81,82]. For a usual Cu-Kα source as used here, the intensity of these weak superstructural peaks might even be too low to be detected. The ab-

sence of superstructural peaks in the XRD results for LNMO_pec implies that a small amount of Mn^{3+} resides inside the spinel lattice. In fact, small amounts of Mn^{3+} were detected by the $Mn^{3+/4+}$ reaction in the CV experiment of LNMO_pec (Figure 4.7a). This means, Ni^{2+} and Mn^{4+} in LNMO_pec are ordered locally at octahedral sites, while any long range order might be suppressed by the presence of Mn^{3+}, which is why local order was detected in Raman but no long range order was detected in XRD.

Phase pure $LiFe_{0.5}Mn_{1.5}O_4$ could be synthesized successfully via additional heat treatment after the Pechini synthesis, as shown by XRD in Figure 4.1 and Figure 4.2. Mn_2O_3, which might have precipitated during solvent evaporation in the Pechini process, was found as impurity phase before ball milling and the final synthesis step at 650 °C (Figure 4.1). After this final step, the Mn_2O_3 precipitates had reacted with the spinel phase to the desired $LiFe_{0.5}Mn_{1.5}O_4$ spinel (Figure 4.2).

As far as known, no Raman spectrum of $LiFe_{0.5}Mn_{1.5}O_4$ has been reported so far. However, the displayed features in the Raman spectrum of $LiFe_{0.5}Mn_{1.5}O_4$ in Figure 4.4b are relatively similar to the Raman spectra of $LiMn_2O_4$ spinel, known from literature [131]. The similar Raman spectra of $LiFe_{0.5}Mn_{1.5}O_4$ and $LiMn_2O_4$ spinel agree to the similar sizes and masses of the cations in both phases, i.e. Mn^{3+} in $LiMn^{3+}Mn^{4+}O_4$ has an ionic radius of 0.645 Å and a mass of 54.938 $g \cdot mol^{-1}$, while Fe^{3+} in $LiFe^{3+}_{0.5}Mn^{3+}_{0.5}Mn^{4+}O_4$ has the same ionic radius of 0.645 Å and a mass of 55.845 $g \cdot mol^{-1}$. One major difference in the spectra of $LiFe_{0.5}Mn_{1.5}O_4$ and of $LiMn_2O_4$ is the intensity of the $F_{2g}^{(1)}$ mode. This intensity is known to be correlated to the average manganese oxidation state [133]. A higher average Mn valance might explain the higher intensity of the $F_{2g}^{(1)}$ mode in the Raman spectrum of $LiFe_{0.5}Mn_{1.5}O_4$. $LiFe_{0.5}Mn_{1.5}O_4$ has a higher Mn^{4+} to Mn^{3+} ratio (1 : 0.5) compared to the Mn^{4+} to Mn^{3+} ratio in $LiMn_2O_4$ (1 : 1).. According to the stoichiometry of $LiFe^{3+}_{0.5}Mn^{3+}_{0.5}Mn^{4+}_{1.5}O_4$ with a Fe^{3+} to Mn^{3+} ratio of 1 : 1, Mn^{3+} and Fe^{3+} were detected by their $Mn^{3+/4+}$ and $Fe^{3+/4+}$ redox reactions at 4.0 and 5.1 V vs. Li/Li^+ in the CV scans with similar capacities (Figure 4.7b).

Pec_LCMO showed a Li_2MnO_3 secondary phase in XRD, as was shown in Figure 4.2. Li_2MnO_3 is well known to coexist with $LiCoMnO_4$ spinels [100]. It usually precipitates upon the loss of oxygen from $LiCoMnO_4$, which leaves behind a cobalt en-

riched and lithium and manganese depleted spinel. Several studies reported the presence of Li_2MnO_3 in $LiCoMnO_4$ samples [15,101,102,105]. Typically, Li_2MnO_3 precipitation can be diminished by using high oxygen partial pressure atmospheres during synthesis and/or lower synthesis temperatures [15,100]. With the chosen Pechini approach, a lowering of temperature was not possible, because 650 °C is the minimum temperature for the burning of the residual organics and nitrates. Especially the nitrates need to be decomposed to avoid Li-nitrate like impurities.

The Raman spectrum of LCMO_pec, as shown in Figure 4.4a, showed the expected bands corresponding to the *Fd-3m* structure, similar to reports in literature [100,131]. Additional bands are correlated to the Li_2MnO_3 secondary phase. The occurrence of Li_2MnO_3 in the Raman spectrum is in coherence to the XRD result. Because of the reduction of Mn^{4+} to Mn^{3+} in spinel, parallel to Li_2MnO_3 formation, as discussed above, the average Mn-ion valence in the spinel compound is reduced. The reduced Mn-valence directly affects the band position of the A_{1g} mode, which is correlated to the average cationic radius on the *16d* site: Mn^{3+} raises the average ionic radius at the octahedral site and causes a shift of the A_{1g} mode to lower wave numbers, due to reduced bond strength and increased bond length in the octahedron [133].

Because of the presence of Mn^{3+}, the position of the A_{1g} mode (at 650 cm^{-1}) of LCMO_pec deviates from the position of the A_{1g} mode as recorded for $LiCoMnO_4$ in literature (652 cm^{-1}) [100], which was illustrated by Figure 4.5 in section 4.1.1 earlier. The position of the A_{1g} mode, as found in this study, would agree to an average cationic radius of 0.542 Å, as shown by Figure 5.1 (which is modified form Figure 4.5, showing the estimated average radius of the cations at the *16d* site in LCMO_pec by a dashed line). This average radius for the octahedral site would match a Mn^{3+} content of around 7 %, i.e. a ratio of $Co^{3+} : Mn^{3+} : Mn^{4+}$ of 1 :0.07:0.93. Consistently, the CV scan for LCMO_pec, as was shown in Figure 4.7c, suggested the presence of Mn^{3+} in the spinel compound by its $Mn^{3+/4+}$ reaction at 4.0 V vs. Li/Li^+ [135].

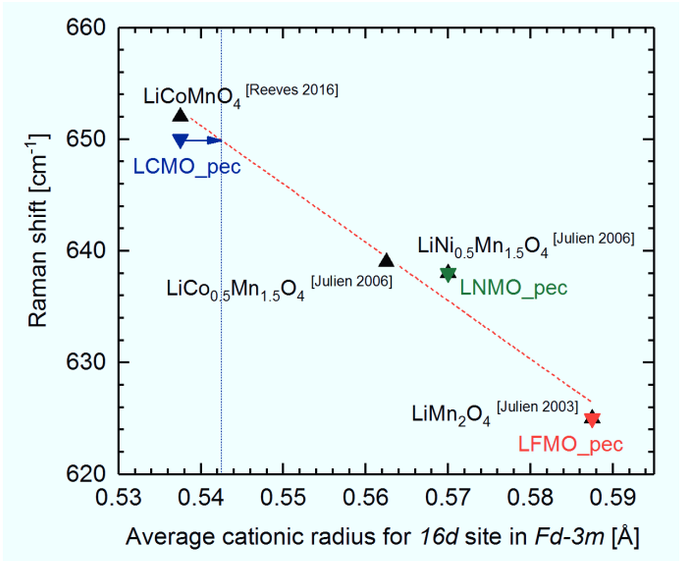

Figure 5.1: Correlation of the position of the band center of the A_{1g} mode of LCMO_pec and LFMO_pec and the A_1 mode of LNMO_pec to the average ionic radius of the transition metal cations on the octahedral site in lithium manganese based spinels and for literature data for $LiMn_2O_4$ [134], $LiNi_{0.5}Mn_{1.5}O_4$, $LiCo_{0.5}Mn_{1.5}O_4$, [133] and for $LiCoMnO_4$ [100].

5.1.2 Thermal decomposition behavior

The thermal decomposition characteristics of the three studied spinels as recorded by DTA/TG (Figure 4.8), agree with the very well-known decomposition behavior of $LiMn_2O_4$ spinel [14]. $LiMn_2O_4$ shows several decomposition reactions upon heating due to oxygen loss [14]. The first decomposition reaction of $LiMn_2O_4$ was reported to start at around 780 °C by releasing oxygen from the lattice and forming an oxygen deficient spinel. The recorded starting temperature for decompositions of the Pechini powders by DTA/TG was at around 650 °C, which is 130 K lower than that for $LiMn_2O_4$. This is in coherence to studies on Ni and Co substituted $LiMn_2O_4$ spinels, which showed that the decomposition temperatures decrease with increasing amount of Co and Ni [54,152].

For $LiMn_2O_4$ spinels, oxygen loss is known to trigger the precipitation of Li_2MnO_3, while the residual spinel becomes lithium and manganese depleted [14,103]. This process is known to start above 780 °C for $LiMn_2O_4$ [14]. However, the investigated Pechni powders are expected to show Li_2MnO_3 precipitates at a much lower tem-

perature due to their lower thermal stability, as observed from the DTA/TG measurements.

Above 915 °C, as a second step, Li_2MnO_3 and $LiMn_2O_4$ are known to react with each other to form $LiMnO_2$ in rocksalt configuration, while manganese is reduced and oxygen is released from the lattice [14]. The reaction was reported to be reversible for $LiMn_2O_4$ spinels [14], which was also detected for the studied spinels by DTA/TG at T_5 in Figure 4.8. For all the three investigated spinels, these reactions happen below 900 °C, which again demonstrates the low thermal stability of the Ni, Fe and Co substituted $LiMn_2O_4$ spinels in comparison to $LiMn_2O_4$.

5.2 Part II: Compatibility of $LiNi_{0.5}Mn_{1.5}O_4$, $LiFe_{0.5}Mn_{1.5}O_4$ and $LiCoMnO_4$ with solid electrolytes

Thermal decomposition of the electrolytes is known to occur at much higher temperatures than the decomposition of the lithium manganese spinels [14,153,154]. LATP remains stable against oxygen loss until 900 °C and LLZ is predicted to decompose due to lithium loss above 1500 °C [153,154]. Heat treatment of the mixtures of the oxide electrolytes and spinel cathodes results in decomposition reactions at temperatures lower than the decomposition temperatures of any used single material, as is evident from the comparison of the DTA/TG results of the single spinel materials in Figure 4.8 with the spinel + electrolyte mixtures in Figure 4.9 and Figure 4.10.

If spinel cathodes are mixed with LLZ, decomposition reactions start at 500 to 550 °C, as can be seen from the DTA/TG and in-situ XRD results (Figure 4.9 and Figure 4.17a, c, and e). This is at least 100 K lower than the decomposition temperature of the spinels themselves. From the thermodynamic theoretical calculations for LLZ+spinels reported by Miara *et al*. [154], it is known that the spinel cathodes act as oxidizers for LLZ that lead to decomposition reactions at temperatures lower than for any of the used single materials. When the two ceramics are in contact with each other at elevated temperatures, oxygen and lithium exchange occur, which leads to accelerated decomposition reactions. It was observed in the in-situ and ex-situ XRD results (Figure 4.11 – Figure 4.13 and Figure 4.17a, c, and e) that one of the major reaction products is Li_2MnO_3. It seems that oxygen, which is lost from the spinel, is absorbed by LLZ to form a lithium rich oxide compound which then drives the formation of Li_2MnO_3. Similar reactions most likely lead to the formation of thermodynamically stable $LiCoO_2$, $LiFeO_2$, and NiO in LCMO+LLZ, LFMO+LLZ, and LNMO+LLZ mixtures, respectively. These phases can be observed via ex-situ XRD (Figure 4.11 – Figure 4.13) together with highly stable phases, such as $La_2Zr_2O_7$, La_2O_3, La_3TaO_7, TiO_2, and $LaMnO_3$, for samples co-sintered at 800 °C.

The mixtures of cathodes and LATP showed decomposition reactions at 550 to 600 °C in the DTA/TG and in-situ XRD experiments (Figure 4.10 and Figure 4.17b, d, and f), which is at least 50 K lower than the individual decomposition tem-

peratures of the single compounds. The decomposition products are thermodynamically stable phosphates and oxides, such as Li_2MnO_3 or Li_3PO_4 that were detected by ex-situ XRD (Figure 4.14 – Figure 4.16). As suggested by the theoretical calculations in [154], the reactions might as well be triggered by oxygen loss from the spinels. However, for LATP, the formation of more stable phosphates is seemingly the major driving force and leads to a large reactivity in between the two materials.

To conclude, both LLZ and LATP in mixture with spinels produce highly stable reaction products at relatively low temperatures. This low reaction temperature makes it impossible to sinter the mixtures in a free sintering process into dense pellets that would have sufficient mechanical strength for battery applications. It would need to be studied if sintering of a mixed cathode can be done by special sintering methods at relatively low temperatures, such as field assistant sintering technology. This method might achieve suitable mixed cathode pellets with reduced formation of large amounts of insulating phases at the cathode-electrolyte interface.

5.3 Part III: Densification of $LiCoMnO_4$ with LiF as sintering additive

Since the compatibility of the materials for processing mixed cathodes by co-sintering is not given, a self-supported dense cathode is chosen as alternative solution to possibly proof the concept of high voltage solid-state batteries. To identify processing routes that lead to high relative densities, as sintering study was carried out for $LiCoMnO_4$. The densification of $LiCoMnO_4$ by usual sintering is insufficient, but its sinterability could be significantly improved by using the sintering additive LiF, as was shown by dilatometry (Figure 4.19) and microstructural investigations via SEM on LCMO_pec and LCMOLiF (Figure 4.21). LiF is known to melt at 845 °C [155] and is used as an effective sintering additive, due to liquid phase sintering, for several oxide class materials, such as perovskites and spinels [139–141]. For $LiCoMnO_4$ spinel, the best sintering conditions were found for 1 wt.-% LiF at 900 °C for 2 h. However, arising pores, with diameters of up to 5 µm, as shown in Figure 4.21e, could be a drawback for the deposition of a continuous thin-film electrolyte with a thickness of 1 to 1.5 µm. Therefore, the microstructure should still be improved with respect to the interface towards the thin-film electrolyte.

To optimize the microstructure further it is crucial to understand the sintering process and the nature and origin of evaporating phases. The chemical analysis of the LCMOLiF10 pellets for 700, 800, 900 and 1000 °C did not indicate any change in cation and fluorine contents upon heating to 1000 °C, as was summarized in Figure 4.24a. This excludes the evaporation of lithium- or transition metal fluorides as was found in other studies [96,139,141,156]. Instead, it could be shown that oxygen is lost from the samples in dependence of the sintering temperature (Figure 4.24a). Oxygen loss is likely to be the reason for the observed large and round shaped pores at triple junctions of the grains of spinel.

Parallel to oxygen loss it was observed by XRD that the phase fraction of Li_2MnO_3 increases in dependence of the sintering temperature (Figure 4.24b). As described in section 5.1.2, oxygen loss for $LiCoMnO_4$ starts at around 650 °C, which triggers the reaction of $LiCoMnO_4$ to lithium and manganese depleted spinel and Li_2MnO_3, with a lower oxygen to cation ratio [100]. It is noted that the formation of Li_2MnO_3 is accelerated in LCMOLiF10 samples compared to the LCMO_pec sample, as disclosed by the quantification of the in-situ high temperature XRD in Figure 4.27. The

Li_2MnO_3 fraction in the LCMO_pec sample did not increase below 650 °C, i.e. the initial Li_2MnO_3 phase fractions of 10 wt.-% is found at 650 °C as well. However, for the LCMOLiF10 sample, the phase fraction of Li_2MnO_3 increased from 10 to 20 wt.-% from room temperature to 650 °C. Lithium over-stoichiometry in lithium manganese spinels is known to result in the formation of Li_2MnO_3 [103,157]. In the investigated sample system, LiF seems to act as a lithium source initiating the formation of additional Li_2MnO_3 already below 650 °C, as illustrated in Figure 5.2.

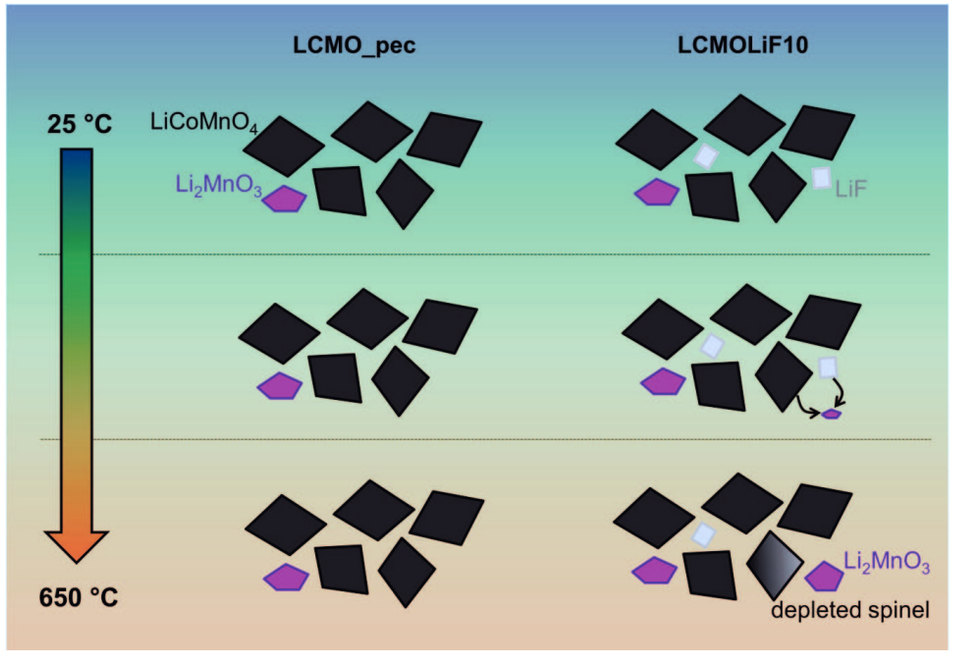

Figure 5.2: Scheme for the explanation of the additional formation of Li_2MnO_3 below 650 °C due to LiF addition in LCMOLiF10 compared to LCMO_pec.

Upon heating from 650 °C to 800 °C, the accelerated Li_2MnO_3 formation for the sample with LiF addition is maintained, as can be seen from the continuous rising of the Li_2MnO_3 fraction until it reaches 50 wt.-% at 800 °C, as was shown in Figure 4.27. At 800 °C, the sample with LiF additive obtains 20 wt.-% more Li_2MnO_3 than the sample without LiF. The lithium supply from 1 wt.-% LiF alone (= 5.5 mol.-%) would only allow for additional Li_2MnO_3 of ~10 wt.-%. The additional ~10 wt.-% of Li_2MnO_3, which are found at 800 °C for the sample with LiF additive can only arise from an accelerated decomposition reaction of spinel, supplying lithium for Li_2MnO_3 formation, as illustrated in Figure 5.3.

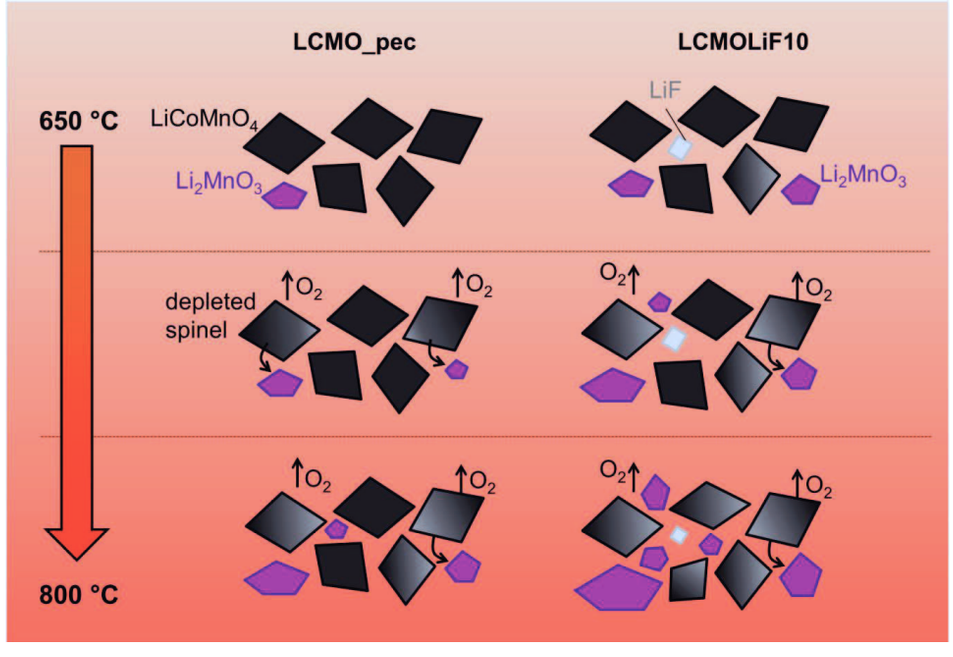

Figure 5.3: Scheme for the explanation of the decomposition reaction of spinel between 650 °C and 800 °C, with and without LiF addition.

Beyond 800 °C, while oxygen is released from the sample continuously, Li_2MnO_3 and spinel are known to react to a $LiMnCoO_3$ phase in rocksalt configuration [100]. The reaction of spinel and Li_2MnO_3 to the rocksalt-type phase starts between 800 and 850 °C for both, the LCMO_pec and LCMOLiF10 sample, as was shown by the quantification of the in-situ XRD data in Figure 4.27. Due to the higher fraction of Li_2MnO_3 in LCMOLiF10, the resulting fraction of the rocksalt phase is much higher than in the LCMO_pec sample (90 wt.-% vs. 30 wt.-% at 850 °C). At 900 °C the rocksalt phase is the only phase detected by XRD in the LCMOLiF10 sample, as illustrated in Figure 5.4. The sinterability of the rocksalt phase might be much better than of spinel, which is why higher densification degrees are achieved for the LCMOLiF10 samples. Additionally, a possible melt phase arising at 850 °C, due to the melting of LiF at 845 °C [155], might help to densify the material.

There is no liquid phase detected in the samples after cooling, i.e. any liquid component that might be present during sintering is crystalline now, as could be demonstrated with the Raman mapping in Figure 4.22. Liquid phases are invisible for XRD, which is why no conclusion can be made regarding any liquid phase for-

mation from the in-situ XRDs. The only evidence for liquid phase formation is the microstructure of the LCMO pellets sintered with LiF (Figure 4.21d+e). The sharp angles and the dense microstructure give a strong indication that a small amount of a liquid phase was present during sintering that is now crystalline.

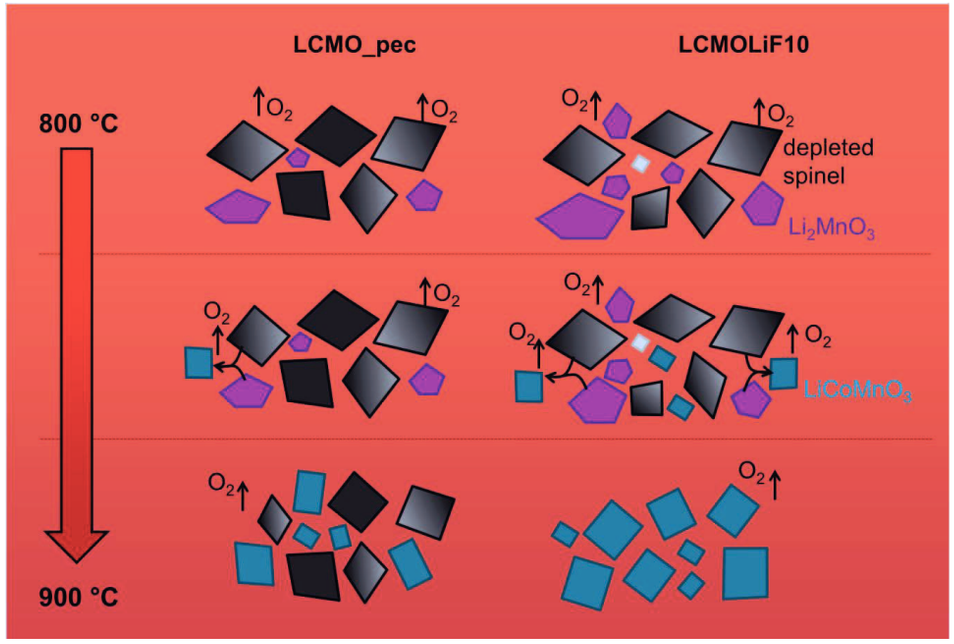

Figure 5.4: Scheme for the explanation of decomposition reactions leading to $LiCoMnO_3$ formation in $LiCoMnO_4$ samples with and without LiF addition.

The Raman mapping, as was shown in Figure 4.22, localizes Li_2MnO_3 at the grain boundaries of spinel in LCMOLiF10_900. The detected second component matches to a $(Co,Mn)_3O_4$ phase, with a lattice parameter similar to $LiCoMnO_4$. Therefore, it is not detected by XRD. This phase might be a residue from the reaction of the $LiCoMnO_3$ rocksalt phase to Li_2MnO_3 and a lithium- and manganese-depleted spinel during cooling. Locally, the lithium- and manganese-depleted spinel might not be reacted to $LiCoMnO_4$ during further cooling and remained as a lithium-depleted spinel derivate. There is no phase detected that indicates a separate fluorine containing phase. It is not clear if fluorine is incorporated into the spinel and/or secondary phases instead. However, it is very likely that fluorine incorporates the spinel structure, since fluorination of spinel has been reported widely [86,91,96].

Despite the large content of impurity phases and despite the unknown distribution and role of fluorine in the densified samples, the electrochemical activity in the high voltage region is unrestricted, as was shown by CV in Figure 4.28. However, the powder properties of the two samples (LCMO_pec and LCMOLiF10_900), especially their particle size distributions, are not comparable due to very different routes of powder processing (wet-chemical powder synthesis vs. sintering and grinding of dense material). A detailed conclusion about the impact on the electrochemical performance during longer cycling in charge discharge experiments cannot be gained from this comparison reliably.

To summarize, the densification of $LiCoMnO_4$ is possible with LiF as sintering additive and relative densities of 90 % are achieved. Further densification is complicated by the evaporation of oxygen and pore coarsening. The obtained microstructure would still be a challenge for any thin-film deposition, but might be improved by sintering in oxygen atmosphere and/or applying pressure during sintering, as in a hot press. Besides oxygen, no evaporating species could be monitored. Since the lithium from the LiF source is consumed by Li_2MnO_3 formation, the fluorine anion likely is incorporated into the lattice of spinel and/or the secondary phases. The electrochemical activity of the material sintered with LiF has been proven; still the impact of fluorine on the electrochemical properties of fluorinated spinel cathodes remains to be investigated. Therefore, $LiCoMnO_{4-\delta}F_x$ powders with different amounts of fluorine contents were studied in *Part IV* of this dissertation and are discussed in the following section.

5.4 Part IV: Impact of fluorination on properties of $LiCoMnO_4$

5.4.1 Chemistry, structure and crystal chemistry of $LiCoMnO_{4-\delta}F_x$

The fluorinated $LiCoMnO_4$ powders were obtained from solid-state reaction. First of all, chemical analysis by NRA (shown in Figure 4.30) confirmed the successful fluorination of $LiCoMnO_{4-\delta}F_x$ (x = 0.05 and 0.1) at 800 °C. Thus, no fluorine loss was observed, which contrasts with studies on fluorinated $LiMn_2O_4$ by Luo *et al.* [96], where the same synthesis temperature was applied. A possible explanation might be that a 100 gram batch size and a closed environment during synthesis were chosen, instead of a two to five gram batch size and an open environment, which alters the synthesis conditions. The present synthesis conditions therefore might have hindered fluorine evaporation, allowing for incorporation of fluorine into the samples.

Moreover, the incorporated fluorine influences the phase purity of the synthesized samples. As was shown by the diffraction results in Figure 4.29 and Figure 4.33, higher amounts of fluorine substituents lead to less secondary Li_2MnO_3 phase and higher amounts of the spinel phase, indicating that fluorine stabilizes the spinel phase.

Joint Rietveld refinement of neutron and synchrotron diffraction confirmed that the structure of the main phase in all samples is the *Fd-3m* spinel structure. The structural formulas were determined to be $[Li_{0.86}Co_{0.14}]^{8a}[Co_{1.05}Mn_{0.95}]^{16d}O_{3.97}$ for LCMOF00, $[Li_{0.88}Co_{0.12}]^{8a}[CoMn]^{16d}O_{3.94}F_x$ for LCMOF05, and $[Li_{0.9}Co_{0.1}]^{8a}[CoMn]^{16d}O_{3.89}F_x$ for LCMOF10, respectively (Table 4.4). It was not possible to determine x with the applied methods. Thus, x is assumed to be 0.04 (for LCMOF05) and 0.09 (for LCMOF10), as derived by NRA.

The oxygen contents of the spinel phases agree to the oxygen contents that are derived by IFA, if the contributions of spinel and secondary phases are considered. That is to say, the overall oxygen stoichiometry as measured by IFA is the sum of the oxygen contents of the spinel and the Li_2MnO_3 secondary phase. The overall sample stoichiometry, as determined by ICP-OES, IFA and NRA (as was given in Table 4.2), is $Li_{1.1}CoMnO_{3.6}$, $Li_{1.1}CoMnO_{3.6}F_{0.04}$ and $Li_{1.1}CoMnO_{3.6}F_{0.09}$, respectively. If the overall oxygen content is calculated from the amount of the main and secondary phase and their stoichiometry, as derived from the powder diffraction re-

sults, a value of 3.63, 3.63 and 3.62 mol is obtained for the oxygen stoichiomtery for LCMOF00, LCMOF05 and LCMOF10.

The oxygen occupancy parameter for the spinel phase in all three samples shifted only slightly away from full occupancy of the anionic site (Table 4.4). As a result, around 0.6 % oxygen vacancies for the spinel phase in all samples is suggested. This confirms that the tolerance for oxygen vacancies in spinel is low and oxygen loss is partially compensated by Li_2MnO_3 formation, consistent with the literature [100,158].

Since the samples consist of both spinel and monoclinic Li_2MnO_3, the changing cation stoichiometry of the spinel phase is a consequence of Li_2MnO_3 formation. Li_2MnO_3 formation leads to lithium and manganese depletion and cobalt enrichment of the residual spinel during synthesis, as was also reported by Reeves *et al*. and Thackeray *et al.* [14,100]. Since fluorination hinders Li_2MnO_3 formation during synthesis, samples with higher fluorine contents (less secondary Li_2MnO_3 phase) exhibit spinels with a lower Co/Li and Co/Mn cation ratio.

Although fluorination impacts the phase purity positively, the recorded impact of fluorination on the crystal lattice is minor. Firstly, the obtained lattice parameters decrease by less than 0.02 % upon fluorination, i.e. from 8.067 Å for LCMOF00 to 8.0652 Å for LCMOF10 (Table 4.3). Usually, for fluorinated $LiNi_{0.5}Mn_{1.5}O_4$, an increase of the lattice parameter is observed upon fluorination, due to an increased Mn^{3+} content as a result of aliovalent substitution of O^{2-} by F^- [93,96]. Secondly, the position of the anionic *32e* site shows hardly any deviation upon fluorination, it remains to be around 0.263 for all samples (Table 4.4). Due to the higher electronegativity of the fluorine anion, shortening of cation-anion bonding could be expected [96]. However, the amount of inserted fluorine is small so that resulting changes in the average structure might be too minor to be resolved by the diffraction methods.

Similarly, the changing cation distribution on tetrahedral and octahedral sites upon fluorination has hardly any effect on the lattice parameter or the anionic site position. A change in the cation ratio on tetrahedral and octahedral sites in between different cations with different ionic radii is usually accompanied by changes in the anionic site position and/or the lattice parameter of the spinel phase [24]. Figure 5.5 illustrates the relation between the oxygen anionic parameter and the volumes of

the tetrahedral and octahedral site. As can be seen, similar anionic positions, as is found for the three studied spinels, reflect similar dimensions of the coordination polyhedra.

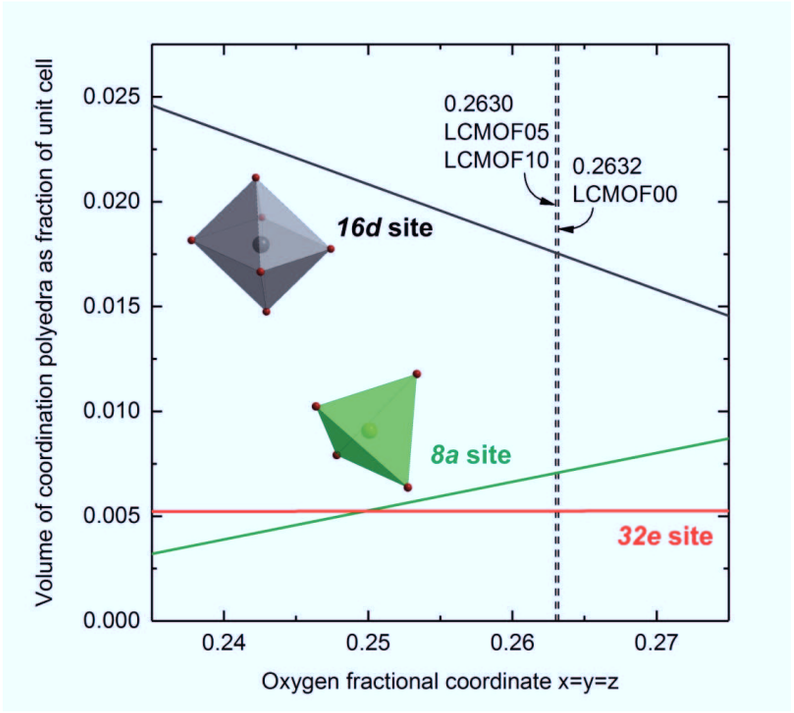

Figure 5.5: Changes in the volume of the coordination polyhedra in the spinel structure as a function of the oxygen fractional coordinate based on Sickafus *et al.* [24] and position for LCMOF00, LCMOF05 and LCMOF10 samples according to the combined Rietveld refinement results.

Changing cation ratios on octahedral and tetrahedral sites without changing the dimensions of the coordination polyhedral is only possible, if cations with very similar radii are interchanged. In the respective systems, this is true for Mn^{4+} and low spin Co^{3+} in octahedral coordination, with ionic radii of 0.53 and 0.545 Å, respectively; and for Li^{+} and Co^{2+} in tetrahedral coordination, with ionic radii of 0.58 and 0.59 Å, respectively [132]. This result indirectly identifies Co^{2+} in the studied spinels, which is in coherence to Reeves *et al*. [100]. According to their study, Co^{2+} was found to migrate to the tetrahedral site, after reduction of Co^{3+} due to oxygen loss and Li_2MnO_3 formation during synthesis [100].

Parallel to the reduction of Co^{3+} to Co^{2+}, Mn^{4+} is reduced to Mn^{3+} in the spinel phase during synthesis, before Li_2MnO_3 precipitation [100]. The electrochemical

measurements (Figure 4.39) confirmed very similar Mn^{3+} contents (around 10 %) for all samples, as will be discussed later. A very similar Mn^{3+} content for the studied spinels is strongly suggested by the powder diffraction results as well. Considering the very large radius of the Mn^{3+} ion (0.645 Å in octahedral coordination), any changes in Mn^{3+} contents would be reflected in the lattice parameters and/or in the oxygen positions, which is not the case. Since all manganese ions in the studied spinels are located at the octahedral sites, it is concluded that Co^{3+}, Mn^{3+}, and Mn^{4+} occupy the octahedral site in a ratio of 1.05 : 0.1 : 0.85 for LCMOF00 and 1 : 0.1 : 0.9 for LCMOF05 and LCMOF10.

5.4.2 Local chemical order

In coherence with the powder diffraction results for the lattice properties and atomic positions, the Raman spectra of the spinel phases (as shown in Figure 4.34) do not suggest any significant changes upon fluorination regarding the lattice vibrations within the tetrahedra and octahedra. The insertion of the fluorine anion into the spinel lattice is expected to impact the bond strength distribution of the cations to the anions, which causes a lowering of the local coordination symmetry and an alteration of the average bond length. This would cause broadening of bands and shifts in the band positions. Since none of these effects are observed upon fluorination, it is concluded that the amount of fluorine anions might to be too low in LCMOF05 and LCMOF10 to cause significant and observable shifts of band positions or broadening of bands in comparison to LCMOF00.

Nevertheless, the increased phase purity of the spinel with increasing fluorination of the samples is clearly visible in the Raman spectra (Figure 4.34), in agreement with the powder diffraction results. Additionally, the high-resolution mapping (shown in Figure 4.35) implies the occurrence of Co_3O_4 in LCMOF00 as impurity with dimensions below the micrometer range. The characteristic Co_3O_4 band at 692 cm^{-1} was recorded in the component spectra of spinel as well. From this observation, it is not clear if there are cobalt enriched Co_3O_4-type clusters within the spinel or if small amounts of Co_3O_4 segregate from the material as an individual phase. In any case, the Co_3O_4 occurrence is observed to get even lower upon fluorination.

Since the results of the high-resolution Raman mapping suggest the occurrence of Co_3O_4 only in trace amounts, Co_3O_4 was disregarded for quantification within the

Rietveld analysis. Moreover, with a lattice parameter of 8.072 Å, Co_3O_4 is close to the lattice parameter of the LCMOF spinel phase (8.067 - 8.065 Å). This means the Co_3O_4 peaks will almost fully overlap with LCMOF, which would make it impossible to refine even higher amounts of Co_3O_4 separately from LCMOF.

As discussed in the previous section 5.4.1, the studied spinels show a mixed cation occupation at octahedral and tetrahedral sites. Especially the mixed cation occupation at the octahedral site is mirrored in the Raman spectra (Figure 4.34): For all samples, the A_{1g} mode of spinel was described best by the superimposition of a relatively sharp and a relatively broad pseudo Voigt function. The A_{1g} mode is the symmetric stretching vibration of the transition metal octahedron. In the investigated LCMOF samples, Mn^{3+}, Mn^{4+} and Co^{3+} share the same octahedral environment. Mn^{3+} causes a local distortion of the octahedral symmetry, known as the Jahn-Teller effect [36]. Mn^{4+} and Co^{3+} maintain the symmetric octahedral coordination, but exhibit rather different bond strengths. This leads to local expansion and contraction of the transition metal octahedrons. Hence, the broadness of the A_{1g} mode is directly caused by different bond lengths and local distortions, due to the occupation of different ions in different valence states at the octahedral site.

In stoichiometric spinel ($LiCoMnO_4$), with Mn^{4+} and Co^{3+} in a 1 : 1 ratio with ionic radii of 0.53 and 0.545 Å (Co^{3+} radius for low spin configuration, see 4.1.1), the average radius of the cations in the octahedron is 0.538 Å. For the spinels in this study, 10 % Mn^{3+} (with a radius of 0.645 Å) raise the average radius to 0.543 Å. This leads to an increased bond length, which weakens the bond strength and causes a shift to lower frequencies of the symmetric stretching vibration of the transition metal octahedron [133]. Thus, the raised Mn^{3+} content in the studied spinels is directly reflected in the position of the A_{1g} mode in the recorded Raman spectra, as was visulaized by Figure 4.37.

5.4.3 Microstructure and electrochemical performance

Besides the clear differences in phase contents and crystallography, the three samples also showed clear differences in microstructure. Figure 4.38 showed that well-crystallized octahedrally shaped particles in LCMOF00 change to smaller truncated crystallites and sintered particles upon fluorination. In previous studies on the fluorination of $LiNi_{0.5}Mn_{1.5}O_4$, increasing amounts of fluorine substituent usually led

to particle growth [86,89,90,97]. In these studies, fluorination was carried out in a post-synthesis step of pristine $LiNi_{0.5}Mn_{1.5}O_4$ spinel. Spinel particle growth was discussed as being a result of a fluxing effect, i.e. of LiF, which melts at 845 °C [86]. Adding LiF as a precursor to the synthesis seems to circumvent the fluxing effect, thus no particle growth was observed. Nevertheless, the development of higher surface energy (100) crystal planes that lead to a truncated octahedral habitus of spinel particles upon F-substitution is in agreement with other studies [91,97].

The observed differences in microstructure (Figure 4.38) directly affect the electrochemical performance in terms of ohmic resistance. Since Li-ion diffusion in the bulk spinel lattice is poor, the large, micrometer sized crystallites in the LCMOF00 sample raise the resistance of the cathode material. Accordingly, the CV shows higher ohmic resistance for the LCMOF00 sample compared to LCMOF05 and LCMOF10, as was shown in Figure 4.39.

In general, the microstructure of the investigated cathodes is not optimized with respect to the electrochemical performance, which is revealed by the values of the discharge capacity of the LCMOF00 sample. In the literature, usually 70 % of the theoretical capacity was reported to be achieved in the first cycles [54,104,106]. Here, only 60 % of the theoretical capacity was recorded, as was demonstrated in Figure 4.40. Likewise, the C-rate tests presented in Figure 4.41 showed rapid capacity fading with increasing C-rates. Spinel-type cathodes usually provide relatively high working C-rates due to their three dimensional Li-ion diffusion paths [27]. However, the total conductivity in the bulk spinel material is relatively low [53]. Thus, a smaller particle size would be more suitable for high C-rate performance due to its shorter diffusion length. The poor results in the electrochemical performance test can therefore be attributed to the relatively large particle size and agglomeration of the particles, i.e., the non-optimized microstructure.

Nevertheless, F-substitution leads to improved cycling stability (as was shown in Figure 4.40), which is in agreement with previous studies [86,88–91]. Additionally, a significant increase in discharge capacity of about 18 % was recorded for LCMOF10 compared to LCMOF00, in the charge discharge experiments (Figure 4.40). An initial explanation might be the improved phase purity with increased fluorine substituent. Taking (possibly) inert Li_2MnO_3 [159,160] into account, these val-

ues need to be normalized to the amount of the spinel phase. Considering 89 wt.-% spinel in LCMOF00, 94 wt.-% spinel in LCMOF05, and 96 wt.-% spinel in LCMOF10, as found by the Rietveld refinements based on the synchrotron and neutron diffraction, yields ~96 $mAhg^{-1}_{spinel}$ for LCMOF00, ~103 $mAhg^{-1}_{spinel}$ for LCMOF05 and ~108 $mAhg^{-1}_{spinel}$ for LCMOF10. Accordingly, the capacity increases by around 8 % from LCMOF00 to LCMOF05 and by around 5 % from LCMOF05 to LCMOF10. Thus, the presence of Li_2MnO_3 – irrespective of whether active or inert – does not alone explain the general trend of increased capacity with rising fluorine substituent.

The improved capacity of fluorinated lithium manganese spinels was discussed on the basis of the increased Mn^{3+} content in previous studies [93,96]. The Mn-ion valence will decrease for charge compensation, if fluorine substitutes oxygen aliovalently. Thus, more electrochemically active Mn^{3+} is available, which increases the capacity. The CV results in Figure 4.39 suggest similar Mn^{3+} contents in all samples, which contrasts with earlier reports [86,90,93,96,97]. However, the intensity of the $Co^{3+/4+}$ redox reactions in the CV measurements increased with increasing amounts of fluorine substituent, implying a higher utilization of the $Co^{3+/4+}$ redox couple with higher fluorine content.

The theoretical discharge capacity of an electrode can be calculated from the possible Li-ion insertion in a given voltage range. In the voltage range starting from 5.3 to 3.4 V vs. Li/Li^+, Li-ions are inserted on tetrahedral *8a* sites in spinel [20]. Based on the structural data derived from Rietveld refinement, one can expect a capacity enhancement for the fluorinated samples because the availability of *8a* sites for Li-ion insertion gets higher for the fluorinated samples, where less cobalt ions reside at *8a* sites.

In fact, calculating the theoretical capacity from the structural formulae as obtained from Rietveld analysis yields ~120 $mAhg^{-1}$ for $[Li_{0.86}Co_{0.14}]^{8a}[Co_{1.05}Mn_{0.95}]^{16d}O_{3.97}$, ~124 $mAhg^{-1}$ for $[Li_{0.88}Co_{0.12}]^{8a}[CoMn]^{16d}O_{3.94}F_{0.04}$ and ~127 $mAhg^{-1}$ for $[Li_{0.9}Co_{0.1}]^{8a}[CoMn]^{16d}O_{3.89}F_{0.09}$. Hence, an increase in capacity by ~ 6 % as an effect of 5 % less cobalt ions on the tetrahedral site is expected. So far two effects can be named, which increase the capacity of $LiCoMnO_4$ upon fluorination: The first reason is the enhanced phase purity and the second reason is the higher availabil-

ity of *8a* Li-sites for lithium extraction and insertion during the electrochemical process.

A third reason for the enhanced capacity might be due to enhanced Li-ion mobility for the fluorinated $LiCoMnO_4$ cathodes. The charge-discharge curves of the second cycle (Figure 4.39) showed that the initial voltage drop is lowest for the LCMOF10 sample. Voltage loss due to activation polarization is usually associated with the activation energy of the Li-ions/electrons inside the material [161]. Since the used amount of carbon in the cathodes is the same, the lower activation polarization for LCMOF10 and LCMOF05 compared to LCMOF00 cathodes suggests a higher Li-ion mobility for higher fluorine contents.

The different slopes of the discharge curves in Figure 4.39b in between 5.2 and 4.94 V vs. Li/Li^+ can be explained by the ohmic polarization of the used cathodes. Ohmic polarization can be attributed to many aspects of the cathode, such as the microstructure of the cathode and used materials, the conductivity of the used material, and the tortuosity for the Li-ion diffusion paths inside the cathode. In other words, since the loading and the preparation processes of the cathodes were similar, the lower slope for LCMOF05 and LCMOF10 than for LCMOF00 indicates that fluorinated $LiCoMnO_4$ has a higher total conductivity, which is the sum of ionic and electronic conductivities, than non-fluorinated $LiCoMnO_4$.

To investigate the Li-ion mobility, the Li-ion diffusion coefficient was approximated from the Randles-Sevcik equation [145] based on CV experiments with different scan rates (Figure 4.42 and Figure 4.43). The sensitivity of this method is known to be relatively high. For the presented samples, systematic errors due to liquid electrolyte decomposition and cell degradation are expected, which might explain the deviation of the derived values for the diffusion coefficient (in the order 10^{-11}) from the theoretical calculated diffusion coefficient for spinels (in the order 10^{-9}) [28] Nevertheless, the observed results can be interpreted qualitatively, which offers valuable insight about how fluorination affects the Li-ion mobility.

First of all, significantly higher Li-ion diffusion coefficients are observed at 4.8 V vs. Li/Li^+ than at 4.0 V vs. Li/Li^+. It is a well-known phenomenon for spinel cathodes that Li-ion diffusion is facilitated when more Li-ion positions in the structure are vacant. At 4.0 V vs. Li/Li^+, at least 90 % of the Li-ion positions are occupied

(as calculated from the concentration of Li-ions, which is described in the results section 4.4.4), causing a low Li-ion mobility. At 4.8 V vs. Li/Li^+, only around 50 % of the Li-ion positions are occupied. Accordingly, Li-ion mobility is enhanced in the high voltage region, due to a higher amount of lithium vacancies, as a result of the electrochemical extraction of Li-ions.

At 4.8 V vs. Li/Li^+a slightly enhanced Li-ion diffusion is observed upon fluorination. Similar to the effect of raised activation energy for the Li-ion hopping mechanism by neighboring Li-ions [28], the occupation of the *8a* site by cobalt ions is expected to cause a raise in the activation energy as well. Considering the slightly lower values of the cobalt ion occupancy at the *8a* site in LCMOF10 (10 %) and LCMOF05 (12 %) in comparison with LCMOF00 (14 %), a slight increase in Li-ion mobility is plausible from a structural point of view and agrees to the observed trend of rising Li-ion diffusion coefficients upon fluorination. This explains the observation of higher capacities upon fluorination, due to faster Li-ion extraction during charging in the high voltage region before the cut-off voltage is reached.

To summarize, improved electrochemical performance was demonstrated upon fluorination of $LiCoMnO_4$, as a result of higher phase purity of the material, better availability of *8a* Li-sites and a slight enhancement in Li-ion mobility, as illustrated in Figure 5.6.

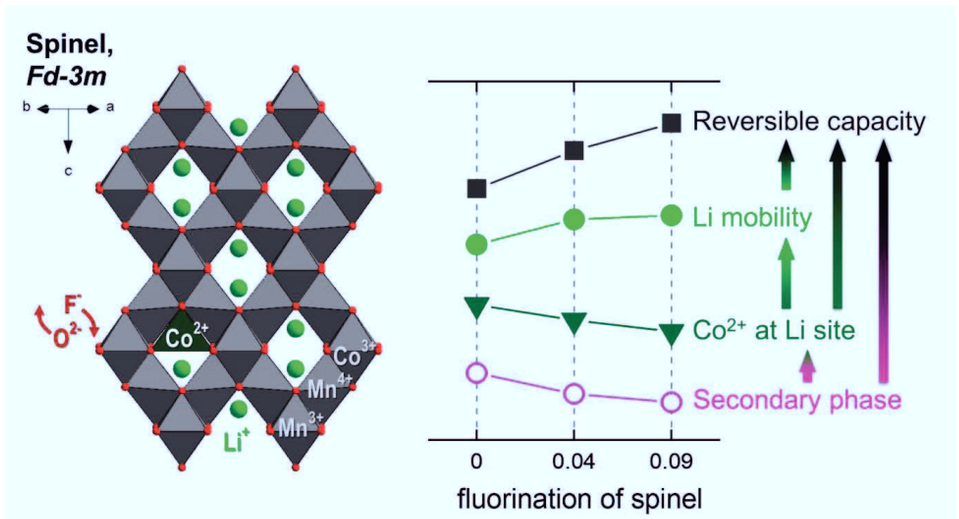

Figure 5.6: Schematic summary of effects leading to higher capacity in fluorinated $LiCoMnO_4$ cathodes

For the LCMOLiF sample systems, where LiF is used as a sintering additive and the additional lithium is consumed by Li_2MnO_3 formation, the effect of better capacity due to higher phase purity is not valid, of course. It has even to be expected, that the capacity is further reduced by migration of Co^{2+} to tetrahedral sites in the cobalt rich spinel residues. However, fluorination had no negative impact on the long-term stability or the rate capability of the $LiCoMnO_4$ cathodes – in fact the cycling stability was even enhanced upon fluorine insertion to the spinel lattice, as could be demonstrated with the fluorinated $LiCoMnO_{4-\delta}F_x$ sample system.

Since liquid electrolyte decomposition could be shown to be a severe problem for the $LiCoMnO_4$ material (Figure 4.40), the engineering of compatible cathode-electrolyte solutions is crucial. Solid electrolytes are among the favorite candidates for the realization of high voltage battery concepts. The concept of the self-supported dense $LiCoMnO_4$ cathode as a substrate for thin-film electrolyte deposition has proved itself worthy to investigate. The addition of LiF could be shown not only to help the densification of the material, but also might lead to an improved performance of the cathode itself if parameters, such as the lithium stoichiometry, are controlled carefully.

6 Summary and outlook

Three high voltage spinels, $LiNi_{0.5}Mn_{1.5}O_4$, $LiFe_{0.5}Mn_{1.5}O_4$ and $LiCoMnO_4$ were synthesized by Pechini synthesis, at a maximum temperature of 650 °C. The obtained powders had a medium particle size of around half a micro-meter. $LiNi_{0.5}Mn_{1.5}O_4$ was synthesized as a partially ordered oxygen non-stoichiometric spinel. $LiCoMnO_4$ was synthesized as an oxygen non-stoichiometric $LiCoMnO_{4-\delta}$ compound with small amounts of Li_2MnO_3 secondary phase, as typical for this compound. A cathode processing route was developed to test the materials with liquid electrolytes to verify their electrochemical activity. All three materials show the expected electrochemical activity, i.e. $LiNi_{0.5}Mn_{1.5}O_4$ with a high voltage redox activity centered at 4.7 V vs. Li/Li^+, $LiFe_{0.5}Mn_{1.5}O_4$ with a high voltage redox activity centered at 5.1 V vs. Li/Li^+ and $LiCoMnO_4$ with a high voltage redox activity centered at 4.9 and 5.2 V vs. Li/Li^+.

In view of the further processing as mixed cathodes and self-supported thin cathodes the three spinels were subjected to thermal analysis by DTA/TG. As typical for lithium-manganese spinel materials, the $LiNi_{0.5}Mn_{1.5}O_4$, $LiFe_{0.5}Mn_{1.5}O_4$ and $LiCoMnO_4$ samples showed thermal decomposition due to oxygen loss and reaction to phases with a lower oxygen content from an onset temperature of 650 °C. The reactions are partially reversible upon cooling, i.e. from 1400 °C to 650 °C up to 80 wt.-% of the lost oxygen is taken up again by the sample and the original spinel phases are restored.

The spinel materials in combination with the LATP or LLZ electrolyte showed the onset of thermal decomposition already at temperatures around 500 to 550 °C and 600 to 650 °C, respectively, which is significantly lower than the onset of the decomposition reactions of the spinels alone. Above these temperatures new phases emerge. Co-sintering without the formation of new phases, as far as detectable by XRD, was possible for spinels+LLZ at 400 °C and for spinels+LATP at 600 °C. For the processing of mixed cathodes by conventional sintering at temperatures above 600 °C, the chemical stability of the investigated spinel and electrolyte mixtures is too low and either different processing routes, different electrolytes or different cell designs need to be investigated.

Since the mixed cathode approach was not applicable in this study, another approach was chosen to target a proof of concept for a high voltage solid-state battery. This approach was based on a self-supported thin cathode, made from the active material only. For this concept, the first step is to find processing routes that lead to high relative densities of the active material. Furthermore, the sinterability of the active material to high relative densities is a crucial step for the processing of mixed cathodes as well. Therefore, $LiCoMnO_4$ spinel, the one with the highest energy density among the synthesized spinels, was selected to be subjected to a sintering study.

Due to the decomposition reactions of $LiCoMnO_4$ spinel its densification via sintering in air is poor. However, it was found that $LiCoMnO_4$ can be densified effectively to up to 90 % by adding 1 wt.-% of LiF as a sintering additive and sintering at 900 °C. LiF accelerates the reaction to Li_2MnO_3 by additional supply of lithium. Li_2MnO_3 and spinel react to $LiCoMnO_3$ rocksalt phase at the sintering temperature completely. The rocksalt phase densifies at 900 °C possibly with the help of a melting phase derived from LiF melting starting at 850 °C. During cooling the reaction is partially reversed – the rocksalt phase separates into spinel and Li_2MnO_3 again, leaving behind a dense microstructure, with Li_2MnO_3 located at the grain boundaries of spinel.

The electrochemical activity and unrestricted high voltage characteristics of the spinel pellets, densified with LiF, could be verified via CV. With the successful densification of $LiCoMnO_4$, the first step in the realization of the solid-state battery based on a self-supported cathode could be completed. However, fluorine was shown to stay within the sample during sintering. This raised the question, which impact a possible fluorination of spinel (F content of ~0.75 wt.-%) would have on the cathode properties and electrochemical performance during cycling. This particular problem gave reason for the investigations of fluorinated $LiCoMnO_4$ cathodes in *Part IV*.

Spinels with the nominal compositions $LiCoMnO_4$, $LiCoMnO_{3.95}F_{0.05}$ and $LiCoMnO_{3.9}F_{0.1}$ (which is equal to ~0.5 and ~1 wt.-% F per formula mass) were synthesized by solid-state reaction at 800 °C. Fluorine incorporation into the spinel lattice was verified directly by NRA and indirectly by XRD. Interestingly, the fluorinated samples showed an improved electrochemical performance in terms of

achieved reversible capacity and cycling stability. The improved cycling stability is most likely an effect of the stabilization of the spinel lattice by the fluorine anion. The capacity was improved by 18 % when 0.1 mol of fluorine was inserted into $LiCoMnO_4$. Detailed investigations of fluorinated $LiCoMnO_4$ cathodes revealed the origin of their enhanced capacity to be an effect of three different reasons:

1) Fluorination improved the phase purity of the samples, due to stabilization of the spinel phase upon the addition of fluorine to the spinel anionic lattice. As observed, the fraction of Li_2MnO_3 secondary phase decreased for higher amounts of fluorine.

2) The fraction of Li_2MnO_3 in the LCMOF samples influences the stoichiometry of spinel. The higher the Li_2MnO_3 fraction, the higher the cobalt-stoichiometry of the spinel phase. The more Co-ions present in spinel, the more Co^{2+}-ions to migrate to the *8a* tetrahedral site. If less cobalt-ions reside at the *8a* site, as in the fluorinated samples (with a lower Li_2MnO_3 phase fraction), there are more tetrahedral sites available for lithium insertion. Consequently, the theoretical capacity is increased, i.e. lowering the Co-ion occupancy on tetrahedral sites by 5 % was shown to increase the theoretical capacity by 6 %. That way, fluorination affects the reversible capacity of $LiCoMnO_4$ indirectly, via influencing Li_2MnO_3 precipitation and the Co-stoichiometry in spinel.

3) Since fluorination affects the distribution of cobalt- and lithium-ions on the tetrahedral sites, it has an indirect influence on the Li-ion diffusion properties, which impact the reversible capacity. If the cobalt-ion occupancy at the *8a* site is lower, the impedance for lithium-ion conduction is lower. Therefore, lithium-ion mobility is enhanced, leading to a faster lithium-ion diffusion causing effectively more lithium-ions to be inserted and extracted, before the cut-off voltage in the high voltage region is reached, thus raising the value of the capacity indirectly.

Based on the studies of $LiCoMnO_{4-\delta}F_x$ spinels, an answer can be given to the question how fluorine incorporation affects $LiCoMnO_4$ cathodes sintered with LiF: First, it could be shown, that LiF addition to $LiCoMnO_4$ leads to an increased Li_2MnO_3 formation with increasing LiF content and temperature. On the other hand, if the lithium stoichiometry is held constant, as in the $LiCoMnO_{4-\delta}F_x$ samples, and only the fluorine content is changed, the Li_2MnO_3 content decreases for increasing fluorine contents. The extent of Li_2MnO_3 formation impacts the extent of lithium- and man-

ganese-depletion and cobalt-enrichment of the spinel phase, which imapcts its capacity. For the $LiCoMnO_4$ cathodes sintered with LiF, it has to be expected that capacities are decreased compared to pure $LiCoMnO_4$ cathodes, due to extended Li_2MnO_3 formation as a reason of additional lithium supply. If the lithium stoichiometry is controlled carfully for $LiCoMnO_4$ cathodes sintered with LiF, capacites could further improve. Furthermore, fluorination was shown to enhance the stability of the spinel phase thermodynamically and during cycling. From these results, no major drawback should be expected for the electrochemical performance of $LiCoMnO_4$ cathodes sintered with LiF. With this study an important step is done towards dense high voltage spinel cathodes that can be used to build up a solid-state battery.

Future work would focus on the development of thin LCMOF pellets with a dense surface. The properties need to be optimized for using the pellet as substrate for the deposition of a thin-film electrolyte. If the large pores, which were found in the samples in this study, cannot be avoided, the thin-film electrolyte needs to be thicker in order to avoid pinholes that would lead to short-circuits. With lithium metal as anode a complete solid-state battery can be build up and cycling in between 3.5 to 5.5 V vs. Li/Li^+ would proof the concept of a high voltage solid state battery.

Once the proof of concept is brought, further effort would need to be put into the optimization of the battery performance. First, the cathode would need to be optimized regarding its thickness to improve its energy density. Thicker cathodes on the other hand require the integration of electronically and ionically conductive pathways to allow for fast electronic and lithium-ion transportation. Electronic pathways might be integrated via infiltration of carbon, silver or other metals. For example, silver can be infiltrated as silver-nitrate(aq)-solution and be reduced to silver below 400 °C. Suitable ionic conducting materials need to be found that might be infiltrated in a similar way. Obviously, a lot of research effort would still ne to be put into the optimization of a high voltage solid-state battery - of which the first step is presented in here.

Acknowledgement

This work would not have been possible without the help of so many people.

First of all, I want to thank Dr. Sven Uhlenbruck, the project leader of the DESIREE project (BMBF project under grant number *03SF0477A* is gratefully acknowledged) that funded my Dissertation. I also want to thank Sven for his open door and open ear and his advice, as well as our scientific discussions that always brought me further.

I want to acknowledge Prof. Dr. Olivier Guillon who agreed to take care of my supervision as “doctoral father” for this dissertation and always supported and encouraged me in doing this research, and Prof. Ulrich Simon, who agreed to evaluate my Dissertation as “zweiter Berichter”.

I want to address many thanks to Dr. Hans-Gregor Gehrke, the post-doc who took care of my supervision in my first year, who was always there for discussion and brought in many good ideas. He left the institute during my first year and I wish him all the best with his new position. I want to say many thanks to Dr. Chih-Long Tsai, who agreed to take care of my supervision afterwards and already helped me a lot in the very first year. Long, I want thank you for your advice and guidance - without interfering my own creativity - throughout these three years of research. Thanks for your open door and all our scientific discussions, especially for your advice in writing publications and bringing everything on its way just in time.

I want to thank all the colleagues in IEK-1 who helped me with my experimental work: Marie-Theres Gerhards and and Sylke Pristat, thank you for all the DTA/TG measurements that you ran for me; Thanks to Dr. Doris Sebold and Reiner Kriescher, who conducted so many SEM analyses for me; Thanks go to Andrea Hilgers und Sigrid Schwartz-Lückge for Archmiedes and particle size distribution measurements; Many thanks also go to Dr. Yoo-Jung Sohn for her help with the Rietveld refinements in the very beginning and her guidance for doing the Refinements on my own; Thank you, Dr. Tim van Gestel, for helping me to develop a wet chemical synthesis route for the spinels. Even though I did not include the results here, because some investigations are still ongoing, I think our collaboration was very fruitful and the first results were really exciting; Special thanks are also at-

tributed to Nicole Lenssen, who helped me in my most busy second year with the experimental work. Nicole, without you I would have never published my first paper in time.

Some very important experiments for this dissertation were conducted abroad, in Oak-Ridge National Lab. Therefore, I would like to thank Dr. Gabriel Veith and his team from the Materials Research group of ORNL for hosting me for a week and giving me the possibility and helping me to carry out experiments in their laboratory. I want to thank Kathie Browning for her help with the thin-film depositions; I especially want to thank Dr. Robert Sacci and Dr. Rose E Ruther for their help in the laboratory particularly with Raman and IR spectroscopy. Many thanks go to Dr. Craig Bridges for teaching me the combined refinement with GSAS and Fullprof and his help in getting this published. Furthermore, I would like to thank Dr. Ashfia Huq and Melanie Kirkham for conducting the Neutron Diffraction experiments and helping me to send the samples to the Advanced Photon Source in Argonne National Lab for Synchrotron measurements, which were carried out by Dr. Saul Lapidus, many thanks.

Many many thanks go to all the colleagues from the battery group, we worked in close collaboration, we discussed and helped each other, we had a good time in the lab, in our battery group meetings and also free time activities, like our carnevals parties. Thank you all for making these three years a lot of fun too. Many of you became good and trusted friends. Thank you, Dr. Sandra Lobe, Dr. Christian Dellen, Dr. Sven Uhlenbruck, Frank Vondahlen, Dr. Martin Bitzer, Thorsten Albrecht, Thorsten Reppert, Dr. Georg Teucher, Dr. Martin Finsterbusch, Dr. Chih-Long Tsai, Dr. Hao Zheng, Yulia Arinicheva, Dr. Frank Tietz, Dr. Quianly Ma, Dr. Enkhe Dashjav, Dr. Marie Guin, Sahir Naquash.

I would like to thank the other colleagues in IEK-1 too that created a nice and warm working atmosphere all the time. Many thanks go to Nikolas Grünwald, we started our PhD in the same month and we shared one office since. Thanks for sharing the fun and also the frustration that one can experience within a Dissertation project. I enjoyed our extended scientific discussions as well as our random talks. I am looking forward to sharing this office with you for a little bit longer.

There are many colleagues at Jülich campus who helped me to conduct a lot of interesting experiments, even though some of these results have not made it into this Dissertation: First of all I want to thank Dr. Volker Nischwitz and Dr. Matthias Balski for the chemical analyses on almost all of my sample systems via ICP-OES and IFA; I also want to thank Dr. Astrid Besmehn for her effort in trying to quantify fluorine via wet chemical methods; I would like to thank Dr. Sören Möller from IEK-4 for helping me with the NRA measurements and their evaluation to quantify fluorine finally; I would like to thank Dr. Egbert Wessel for his efforts in trying to find fluorine in my densified samples via EDX and WDX and to locate it in the sample - unfortunately its signal was overlain by the Co-signal. I want to thank Emmanouil Veroutis and Prof. Dr. Josef Granwehr for investigating my samples via NMR to look at the local order around the fluorine anion, an investigation which is still ongoing. I want to thank Dr. Jin Lei for conducting very amazing TEM measurements on a sample system which unfortunately has not made it into this dissertation because it is not completed yet. I also want to thank the SPS-group including Prof. Dr. Martin Bram, Prof. Dr. Jesus Gonzales, Dr. Marc Rubat du Merac and Ralf Steinert for collaborating with me on the densification of $LiMn_2O_4$ and $LiCoMnO_4$ spinels.

Finally, I would like to thank my husband, my mother, my brother and my grandparents for their love, support and their curiosity in my work, without you backing me I would not have made it that far.

List of figures

Figure 1.1: Schematic representation of potential, capacity and energy density relations between commercial and high voltage cathode materials in lithium-ion batteries. 2
Figure 1.2: Scheme of the desired microstructure for a mixed cathode for solid-state lithium batteries. 3
Figure 2.1: Schematic representation of a lithium-ion battery and the processes during discharge and charge. 6
Figure 2.2: Visualization of the $Li(M,Mn)_2O_4$ cathode in *Fd-3m* spinel structure with indication of Wyckoff positions from two different viewing directions: a) 1, 2, 5 viewing direction and representation of the lithium-ion diffusion path (green arrows) in between the *8a* and *16d* sites; b) 13, 11, -1 viewing direction to visualize the three dimensional channels for lithium-ion diffusion. 9
Figure 2.3: Properties of the $LiNi_{0.5}Mn_{1.5}O_4$ high voltage cathode. 12
Figure 2.4: Properties of the $LiFe_{0.5}Mn_{1.5}O_4$ high voltage cathode. 14
Figure 2.5. Properties of the $LiCoMnO_4$ high voltage cathode. 15
Figure 2.6: Schematic representation of a solid-state lithium battery and the processes during discharge and charge. 17
Figure 3.1: Scheme for the Pechini synthesis of $LiNi_{0.5}Mn_{1.5}O_4$, $LiFe_{0.5}Mn_{1.5}O_4$ and $LiCoMnO_4$. 20
Figure 3.2: Scheme for the solid-state reaction synthesis of LCMOF00, LCMOF05 and LCMOF10. 21
Figure 3.3: Scheme for the preparation of spinel + electrolyte mixtures and spinel + electrolyte pellets. 22
Figure 3.4: Sheme for the preparation of LCMOLiF powders and LCMOLiF pellets. 22
Figure 3.5: Scheme of the $^{19}F(p,\alpha_0)^{16}O$ nuclear reaction. 25
Figure 3.6:.Principle of X-ray diffraction and intensity of scattered X-rays (described by the structure factor) as a function of the electron density of the given element, for a Bragg angle of $2\theta = 0$ (for $2\theta = 0$ the structure factor equals the number electrons / atomic number of the given element) [129]. 29

Figure 3.7: Principle of Neutron diffraction and neutron scattering length as a function of the atomic number. The scattering lengths of the elements were taken from Sears [130]. 29
Figure 4.1: XRD patterns of LMCO_pec, LMFO_pec and LMNO_pec after calcination..... 32
Figure 4.2: XRD patterns of LMCO_pec, LMFO_pec and LMNO_pec after annealing. 32
Figure 4.3: Correlation of the lattice parameter to the average ionic radius of the transition metal cations on the octahedral site in lithium manganese based spinels (space group *Fd-3m*) for LCMO_pec, LFMO_pec and LNMO_pec in comparison to literature data for $LiMn_2O_4$ [131], $LiNi_{0.5}Mn_{1.5}O_4$ [30], $LiCo_{0.5}Mn_{1.5}O_4$ [133] and $LiCoMnO_4$ [100]. 33
Figure 4.4: Results of the micro Raman spectroscopy from a sample surface area of 70 µm × 40 µm. Averaged and normalized data from measurement with fitted spectra for a) LCMO_pec, b) LFMO_pec and c) LNMO_pec. 35
Figure 4.5: Correlation of the position of the band center of the A_{1g} mode of LCMO_pec and LFMO_pec and the A_1 mode of LNMO_pec to the average ionic radius of the transition metal cations on the octahedral site in lithium manganese based spinels and for literature data for $LiMn_2O_4$ [134], for $LiNi_{0.5}Mn_{1.5}O_4$ and for $LiCo_{0.5}Mn_{1.5}O_4$ [133] and for $LiCoMnO_4$ [100]. 36
Figure 4.6: SEM images LNMO_pec, LFMO_pec and LCMO_pec. 37
Figure 4.7: CV of the samples a) LMNO_pec, b) LMFO_pec and c) LMCO_pec. .. 38
Figure 4.8: a) DTA and b) TG results of spinel powders. DTA signal offset: 1 unit (for LFMO_pec), 2 units (for LCMO_pec). TG signal offset: 2 units (for LFMO_pec) and 4 units (for LCMO_pec). 40
Figure 4.9: a) DTA and b) TG of spinel+LLZ powders. DTA signal offset: 1 unit (for LFMO), 2 units (for LCMO). TG signal offset: 2 units (for LFMO) and 4 units (for LCMO). 41
Figure 4.10: a) DTA and b) TG of spinel+LATP powders. DTA signal offset: 1 unit (for LFMO), 2 units (for LCMO). TG signal offset: 2 units (for LFMO) and 4 units (for LCMO). 42
Figure 4.11: XRD patterns of LCMO+LLZ mixtures that were heat treated at 800 °C, 600 °C, 400 °C and as mixed powder..... 43

Figure 4.12: XRD patterns of LFMO+LLZ mixtures that were heat treated at 800 °C, 600 °C, 400 °C and as mixed powder. 44
Figure 4.13: XRD patterns of LNMO+LLZ mixtures that were heat treated at 800 °C, 600 °C, 400 °C and as as-mixed powder. 44
Figure 4.14: XRD patterns of LCMO+LATP mixtures that were heat treated at 800 °C, 700 °C, 600 °C and as mixed powder. 46
Figure 4.15: XRD patterns of LNMO+LATP mixtures that were heat treated at 800 °C, 700 °C, 600 °C and as mixed powder. 46
Figure 4.16: XRD patterns of LFMO+LATP mixtures that were heat treated at 800 °C, 700 °C, 600 °C and as mixed powder. 47
Figure 4.17: In-situ high temperature XRD of a) LCMO+LLZ, b) LFMO+LLZ, and c) LNMO+LLZ in between 300 and 900 °C in 50 K steps. At each temperature, five scans were collected..... 49
Figure 4.18: In-situ high temperature XRD of a) LCMO+LATP, b) LFMO+LATP, and c) LNMO+LATP in between 300 and 900 °C in 50 K steps. At each temperature, five scans were collected. 50
Figure 4.19: Results of dilatometry of LCMO_pec and LCMOLiF10. 51
Figure 4.20: Results of ex-situ XRD on LCMO_pec and LCMOLiF10 samples. ... 52
Figure 4.21: a) Obtained relative densities of LCMOLiF samples and SEM images of the samples with the highest achieved relative densities for using different amounts of the LiF sintering additive each: b) LCMO_1000; c) LCMOLiF05_900; d) LCMOLiF15_1000; e) LCMOLiF10_900. 54
Figure 4.22: Component analysis results of the high-resolution micro Raman mapping for LCMOLiF10_900. Color coded identified components: (a) in blue, $LiCoMnO_4$ spinel; (b) in cyan, $(Co,Mn)_3O_4$-type spinel compound; (c) in magenta, Li_2MnO_3; (d) in yellow, Co_3O_4-type spinel compound. Component spectra below. 56
Figure 4.23: Representative spectra of the individual components in the component analysis of the Raman mapping result. a) $LiCoMnO_4$ spinel, b) $(Co,Mn)_3O_4$-type spinel compound, c) Li_2MnO_3, and d) Co_3O_4-type spinel compound. 57
Figure 4.24: Changes in a) chemistry and b) weight fraction of the Li_2MnO_3 phase as a function of temperature in sintered LCMOLiF10 pellets. 58
Figure 4.25: NRA measured and simulated data for LCMOLiF10_1000 and LCMOLiF10_700. The inset shows the not-overlain NRA data of fluorine. The yield

was normalized to the particle*sr factor (=number of incident particles times the solid angle of the detector). 58
Figure 4.26: Color coded pseudo 3D diffractograms for the in-situ high temperature XRD for a) LCMO_pec and b) LCMOLiF10. 59
Figure 4.27: Quantification of phases from the in-situ high temperature XRD data. 61
Figure 4.28: Cyclic voltammetry of LCMOLiF15_900 and pure LCMO_pec for comparison. Scan rate 0.1 mV/s....62
Figure 4.29: XRD result of LCMOF00, LCMOF05 and LCMOF10. a) full °2θ range, b) excerpt of data from 17.5-21.5°2θ. Main phase is indexed to *Fd-3m* [33] and secondary phase (#) was *C2/m*: Li_2MnO_3 [128]. 63
Figure 4.30: NRA measured and simulated data for LCMOF00, LCMOF05 and LCMOF10. The inset shows the not-overlain NRA data of fluorine. The yield was normalized to the particle*sr factor (=number of incident particles times the solid angle of the detector)....65
Figure 4.31: Combined Rietveld refinement of LCMOF00 a) Neutron diffraction (excerpt from 1 - 10.3 $Å^{-1}$, actual fitting range from 1 - 15 $Å^{-1}$), b) Synchrotron diffraction, full Q-range. 66
Figure 4.32: Combined Rietveld refinement of LCMOF05 a) Neutron diffraction (excerpt from 1 - 10 $Å^{-1}$, actual fitting range from 1 – 15 $Å^{-1}$), b) Synchrotron diffraction, full Q-range; and combined Rietveld refinement of LCMOF10 c) Neutron diffraction (excerpt from 1 – 10 $Å^{-1}$, actual fitting range from 1 – 15 $Å^{-1}$), d) Synchrotron diffraction, full Q-range. 67
Figure 4.33. a) Visualization of spinel *Fd-3m* structure and cation distribution, b) cation distribution and phase content of Li_2MnO_3 (*C2/m*) as a function of fluorine content....69
Figure 4.34: Results of the Raman mapping in an area of 100 × 60 µm. Averaged, normalized and fitted spectra for a) LCMOF00, b) LCMOF05 and c) LCMOF10. Color coding for bands in figure a is the same than in b and c. 72
Figure 4.35: Component analysis results of the high-resolution micro Raman mapping of LCMOF00. Representative spectra of the individual components are given in a) for spinel, b) for Li_2MnO_3, and c) for a Co-rich component....73

Figure 4.36: Component analysis results of the high-resolution micro Raman mapping of a) LCMOF05 and b) LCMOF10. The blue regions are spinel and the pink regions are Li_2MnO_3. 73
Figure 4.37: Correlation of the position of the band center of the A_{1g} mode to the average ionic radius of the transition metal cations on the octahedral site in lithium manganese based spinels (space group *Fd-3m)*. Literature data for $LiMn_2O_4$ [131], $LiNi_{0.5}Mn_{1.5}O_4$, $LiCo_{0.5}Mn_{1.5}O_4$ [133], and $LiCoMnO_4$ [100,117]. 75
Figure 4.38: SEM images of (a)+(b) LCMOF00, (c)+(d) LCMOF05 and (e)+(f) LCMOF10. 76
Figure 4.39: a) CV results of 2nd cycle for LCMOF00, LCMOF05 and LCMOF10. b) Charge-discharge curves of the 2nd cycle for LCMOF00, LCMOF05 and LCMOF10. 77
Figure 4.40: Specific discharge capacity, capacity retention and efficiency for LCMOF00, LCMOF05 and LCMOF10. 80
Figure 4.41: Rate capability testing for LCMOF00, LCMOF05 and LCMOF10. 81
Figure 4.42: Cyclic voltammetry of LCMOF00, LCMOF05 and LCMOF10 at different scan rates: 0.1, 0.13, 0.16, 0.21, 0.4, and 0.65 mV/s. 82
Figure 4.43 Linear regression of square root of CV scan rate and the peak current for peak 1 (centered at 3.9 V vs. Li/Li+) and peak 2 (centered at 4.9 V vs. Li/Li+). 84
Figure 5.1: Correlation of the position of the band center of the A_{1g} mode of LCMO_pec and LFMO_pec and the A_1 mode of LNMO_pec to the average ionic radius of the transition metal cations on the octahedral site in lithium manganese based spinels and for literature data for $LiMn_2O_4$ [134], $LiNi_{0.5}Mn_{1.5}O_4$, $LiCo_{0.5}Mn_{1.5}O_4$, [133] and for $LiCoMnO_4$ [100]. 89
Figure 5.2: Scheme for the explanation of the additional formation of Li_2MnO_3 below 650 °C due to LiF addition in LCMOLiF10 compared to LCMO_pec. 94
Figure 5.3: Scheme for the explanation of the decomposition reaction of spinel between 650 °C and 800 °C, with and without LiF addition. 95
Figure 5.4: Scheme for the explanation of decomposition reactions leading to $LiCoMnO_3$ formation in $LiCoMnO_4$ samples with and without LiF addition. 96
Figure 5.5: Changes in the volume of the coordination polyhedra in the spinel structure as a function of the oxygen fractional coordinate based on Sickafus et al. 1999 [24] and position for LCMOF00, LCMOF05 and LCMOF10 samples according to the combined Rietveld refinement results. 100

Figure 5.6: Schematic summary of effects leading to higher capacity in fluorinated $LiCoMnO_4$ cathodes 106

List of tables

Table 2.1: Properties of commercial lithium-ion batteries [21,22]. 7
Table 2.2: Examples of high voltage spinel cathodes as known from literature. 11
Table 3.1: Synthesis conditions for $LiNi_{0.5}Mn_{1.5}O_4$, $LiFe_{0.5}Mn_{1.5}O_4$ and $LiCoMnO_4$. 20
Table 3.2: Sintering conditions for different LCMOLiF pellets. 23
Table 3.3: Parameters for the XRD measurement and analysis method. 24
Table 3.4: Measurement conditions for DTA/TG and Dilatometry measurements of samples. 26
Table 3.5: Measurement conditions for the in-situ high temperature X-ray diffraction. 27
Table 3.6: Measurement conditions for micro Raman spectroscopy. 28
Table 3.7: Electrochemical measurements setup and sample systems. 30
Table 4.1. Phase contents, theoretical and relative densities of LCMOLiF samples. 53
Table 4.2: Stoichiometry in mole per formula unit of LCMOF00, LCMOF05 and LCMOF10 samples derived from ICP-OES (Li, Mn Co), IFA (O) and NRA (F). 64
Table 4.3: Lattice parameters, phase content, and goodness of fit obtained by the combined Rietveld refinement of LCMOF00, LCMOF05, and LCMOF10 based on neutron and synchrotron diffraction. 68
Table 4.4: Structural parameters of spinel main phase obtained from Rietveld refinement of LCMOF00, LCMOF05 and LCMOF10. Space group *Fd-3m*, origin at *-3m.* 70
Table 4.5: Calculated concentration of Li-ions (C_0) and Li-ion diffusion coefficients (D) at peak 1 and peak 2 for LCMOF00, LCMOF05 and LCMOF10. 85

References

[1] M. S. Whittingham, *Lithium Batteries and Cathode Materials*, Chem. Rev. 104 (2004) 4271–4302.

[2] J. B. Goodenough, Y. Kim, *Challenges for Rechargeable Li Batteries*, Chem. Mater. 22 (2010) 587–603.

[3] E. J. Cairns, P. Albertus, *Batteries for Electric and Hybrid-Electric Vehicles*, Annu. Rev. Chem. Biomol. Eng. 1 (2010) 299–320.

[4] M. Freire, N. V. Kosova, C. Jordy, D. Chateigner, O. I. Lebedev, A. Maignan, V. Pralong, *A new active Li–Mn–O compound for high energy density Li-ion batteries*, Nat Mater 15 (2015) 173–177.

[5] K. Kang, Y. S. Meng, J. Bréger, C. P. Grey, G. Ceder, *Electrodes with High Power and High Capacity for Rechargeable Lithium Batteries*, Science 311 (2006) 977–980.

[6] H. Kawai, M. Nagata, H. Tukamoto, A.R. West, *High-voltage lithium cathode materials*, J. Power Sources 81-82 (1999) 67–72.

[7] A. Kraytsberg, Y. Ein-Eli, *Higher, Stronger, Better… A Review of 5 Volt Cathode Materials for Advanced Lithium-Ion Batteries*, Adv. Energy Mater. 2 (2012) 922–939.

[8] W. Xu, X. Chen, F. Ding, J. Xiao, D. Wang, A. Pan, J. Zheng et al., *Reinvestigation on the state-of-the-art nonaqueous carbonate electrolytes for 5 V Li-ion battery applications*, J. Power Sources 213 (2012) 304–316.

[9] K. Xu, *Nonaqueous Liquid Electrolytes for Lithium-Based Rechargeable Batteries*, Chem. Rev. 104 (2004) 4303–4418.

[10] C. Sun, J. Liu, Y. Gong, D.P. Wilkinson, J. Zhang, *Recent advances in all-solid-state rechargeable lithium batteries*, Nano Energy 33 (2017) 363–386.

[11] J. G. Kim, B. Son, S. Mukherjee, N. Schuppert, A. Bates, O. Kwon, M. J. Choi et al., *A review of lithium and non-lithium based solid state batteries*, Journal of Power Sources 282 (2015) 299–322.

[12] Q. Ma, Q. Xu, C.-L. Tsai, F. Tietz, O. Guillon, *A Novel Sol–Gel Method for Large-Scale Production of Nanopowders: Preparation of $Li_{1.5}Al_{0.5}Ti_{1.5}(PO_4)_3$ as an Example*, J. Am. Ceram. Soc. 99 (2016) 410–414.

[13] C.-L. Tsai, V. Roddatis, C. V. Chandran, Q. Ma, S. Uhlenbruck, M. Bram, P. Heitjans et al., *$Li_7La_3Zr_2O_{12}$ Interface Modification for Li Dendrite Prevention*, ACS Appl. Mater. Interfaces 8 (2016) 10617–10626.

[14] M. M. Thackeray, M. F. Mansuetto, D. W. Dees, D. R. Vissers, *The thermal stability of lithium-manganese-oxide spinel phases*, Mat. Res. Bull. 31 (1996) 133–140.

[15] D. Pasero, S. de Souza, N. Reeves, A. R. West, *Oxygen content and electrochemical activity of $LiCoMnO_{4-\delta}$*, J. Mater. Chem. 15 (2005) 4435–4440.

[16] B. Scrosati, K. M. Abraham, W. A. van Schalkwijk, J. Hassoun, *Lithium batteries: Advanced technologies and applications*. Electrochemical Society series, Wiley; 1st edition, 2013.

[17] M.S. Whittingham, *Introduction: Batteries*, Chem. Rev. 114 (2014) 11413.

[18] G.-A. Nazri, G. Pistoia (Eds.), *Lithium Batteries*, Springer US, 2003.

[19] M. M. Thackeray, *Spinel Electrodes for Lithium Batteries*, J. Am. Chem. Soc. 82 (1999) 3347–3354.

[20] C. M. Julien, A. Mauger, *Review of 5-V electrodes for Li-ion batteries*, Ionics 19 (2013) 951–988.

[21] R. A. Meyers, *Encyclopedia of Sustainability Science and Technology*, Springer New York, New York, NY, 2012.

[22] T. B. Reddy, *Linden's handbook of batteries: Set 2*, 4th ed., McGraw-Hill Professional; McGraw-Hill [distributor], New York, London, 2010.

[23] E. Riedel, R. Alsfasser, *Moderne anorganische Chemie*, 3rd ed., Gruyter, Berlin [u.a.], 2007.

[24] K. E. Sickafus, J. M. Wills, N.W. Grimes, *Structure of Spinel*, J. Am. Chem. Soc. 82 (1999) 3279–3292.

[25] T. Hahn, H. Fuess, H. Wondratschek, U. Müller, U. Shmueli, E. Prince, A. Authier et al., *International Tables for Crystallography*, 5th ed., International Union of Crystallography, Chester, England, 2006.

[26] R. G. Burns, *Mineralogical Applications of Crystal Field Theory*, Cambridge University Press, Cambridge, 1993.

[27] M. M. Thackeray, W. I. F. David, P. G. Bruce, J. B. Goodenough, *Lithium insertion into manganese spinels*, Mater. Res. Bull. 18 (1983) 461–472.

[28] X. Ma, B. Kang, G. Ceder, *High Rate Micron-Sized Ordered $LiNi_{0.5}Mn_{1.5}O_4$*, J. Electrochem. Soc. 157(8) A925, 2010, 10.1149/1.3439678.

[29] P. B. Samarasingha, N. H. Andersen, M. H. Sørby, S. Kumar, O. Nilsen, H. Fjellvåg, *Neutron diffraction and Raman analysis of $LiMn_{1.5}Ni_{0.5}O_4$ spinel type oxides for use as lithium ion battery cathode and their capacity enhancements*, Solid State Ionics 284 (2016) 28–36.

[30] J. Cabana, M. Casas-Cabanas, F. O. Omenya, N. A. Chernova, D. Zeng, M. S. Whittingham, C. P. Grey, *Composition-Structure Relationships in the Li-Ion Battery Electrode Material $LiNi_{0.5}Mn_{1.5}O_4$*, Chem. Mater. 24 (2012) 2952–2964.

[31] D. W. Shin, C. A. Bridges, A. Huq, M. P. Paranthaman, A. Manthiram, *Role of Cation Ordering and Surface Segregation in High-Voltage Spinel $LiMn_{1.5}Ni_{0.5-x}M_xO_4$ (M = Cr, Fe, and Ga) Cathodes for Lithium-Ion Batteries*, Chem. Mater. 24 (2012) 3720–3731.

[32] M. M. Thackeray, A. de Kock, M. H. Rossouw, D. Liles, R. Bittihn, D. Hoge, *Spinel Electrodes from the Li-Mn-O System for Rechargeable Lithium Battery Applications*, Journal of The Electrochemical Society 139 (1992) 363–366.

[33] M. M. Thackeray, A. de Kock, W. I. F. David, *Synthesis and structural characterization of defect spinels in the lithium-manganese-oxide system*, Mat. Res. Bull. 28 (1993) 1041–1049.

[34] J. M. Tarascon, D. Guyomard, *The $Li_{1+x}Mn_2O_4$/C rocking-chair system: a review*, Electrochimica Acta 38 (1993) 1221–1231.

[35] J. W. Fergus, *Recent developments in cathode materials for lithium ion batteries*, Journal of Power Sources 195 (2010) 939–954.

[36] A. Yamada, M. Tanaka, K. Tanaka, K. Sekai, *Jahn–Teller instability in spinel Li–Mn–O*, J. Power Sources 81–82 (1999) 73–78.

[37] R. J. Gummow, A. de Kock, M. M. Thackeray, *Improved capacity retention in rechargeable 4 V lithium/lithium-manganese oxide (spinel) cells*, Solid State Ionics 69 (1994) 59–67.

[38] A.V. Chadwick, S. L. P. Savin, R. J. Packer, A. N. Blacklocks, R. A. Davis, M. S. Islam, *EXAFS studies of lithium manganese oxides*, Phys. Status Solidi C 2 (2005) 657–660.

[39] H. W. Chan, J. G. Duh, S. R. Sheen, *$LiMn_2O_4$ cathode doped with excess lithium and synthesized by co-precipitation for Li-ion batteries*, Journal of Power Sources 115 (2003) 110–118.

[40] A. Paolone, R. Cantelli, B. Scrosati, P. Reale, M. Ferretti, C. Masquelier, *Doping effects on the phase transition of $LiMn_2O_4$ by anelastic spectroscopy and differential scanning calorimetry*, Proceedings of the 14th International Conference on Internal Friction and Mechanical Spectroscopy 442 (2006) 220–223.

[41] S. Shi, C. Ouyang, D.-S. Wang, L. Chen, X. Huang, *The effect of cation doping on spinel $LiMn_2O_4$: a first-principles investigation*, Solid State Communications 126 (2003) 531–534.

[42] R. Thirunakaran, R. Ravikumar, S. Gopukumar, A. Sivashanmugam, *Electrochemical evaluation of dual-doped $LiMn_2O_4$ spinels synthesized via co-precipitation method as cathode material for lithium rechargeable batteries*, Journal of Alloys and Compounds 556 (2013) 266–273.

[43] M. A. Arillo, G. Cuello, M. L. López, P. Martín, C. Pico, M. L. Veiga, *Structural characterisation and physical properties of $LiMMnO_4$ (M=Cr, Ti) spinels*, Solid State Sciences 7 (2005) 25–32.

[44] L.-W. Ma, B.-Z. Chen, X.-C. Shi, W. Zhang, K. Zhang, *Stability and Li^+ extraction/adsorption properties of $LiM_xMn_{2-x}O_4$ (M = Ni, Al, Ti; 0 ≤ x ≤ 1) in aqueous solution*, Colloids and Surfaces A: Physicochemical and Engineering Aspects 369 (2010) 88–94.

[45] T. Ohzuku, S. Takeda, M. Iwanaga, *Solid-state redox potentials for $Li[Me_{1/2}Mn_{3/2}]O_4$ (Me: 3d-transition metal) having spinel-framework structures: a*

series of 5 volt materials for advanced lithium-ion batteries, Journal of Power Sources 81-82 (1999) 90–94.

[46] M. Obrovac, Y. Gao, J. Dahn, *Explanation for the 4.8-V plateau in $LiCr_xMn_{2-x}O_4$*, Phys. Rev. B 57 (1998) 5728–5733.

[47] J. Molenda, J. Marzec, K. Świerczek, D. Pałubiak, W. Ojczyk, M. Ziemnicki, *The effect of 3d substitutions in the manganese sublattice on the electrical and electrochemical properties of manganese spinel*, Fourteenth International Conference on Solid State Ionics 175 (2004) 297–304.

[48] C. Sigala, D. Guyomard, A. Verbaere, Y. Piffard, M. Tournoux, *Positive electrode materials with high operating voltage for lithium batteries: $LiCr_yMn_{2-y}O_4$ ($0 \le y \le 1$)*, Solid State Ionics 81 (1995) 167–170.

[49] K. Amine, H. Tukamoto, H. Yasuda, Y. Fujita, *Preparation and electrochemical investigation of $LiMn_{2-x}Me_xO_4$ (Me: Ni, Fe, and x = 0.5, 1) cathode materials for secondary lithium batteries*, Proceedings of the Eighth International Meeting on Lithium Batteries 68 (1997) 604–608.

[50] H. Shigemura, M. Tabuchi, H. Kobayashi, H. Sakaebe, A. Hirano, H. Kageyama, *Structural and electrochemical properties of $Li(Fe,Co)_xMn_{2-x}O_4$ solid solution as 5 V positive electrode materials for Li secondary batteries*, J. Mater. Chem. 12 (2002) 1882–1891.

[51] H. Kawai, M. Tabuchi, M. Nagata, H. Tukamoto, A. R. West, *Crystal chemistry and physical properties of complex lithium spinels $Li_2MM'_3O_8$ (M=Mg, Co, Ni, Zn; M'=Ti, Ge)*, J. Mater. Chem. 8 (1998) 1273 – 1280.

[52] P. Aitchison, B. Ammundsen, D. J. Jones, G. Burns, J. Roziere, *Cobalt substitution in lithium manganate spinels: examination of local structure and lithium extraction by XAFS*, J. Mater. Chem. 9 (1999) 3125–3130.

[53] H. Kawai, M. Nagata, H. Kageyama, H. Tukamoto, A. R. West, *5 V lithium cathodes based on spinel solid solutions $Li_2Co_{1+X}Mn_{3-X}O_8$: $-1 \le X \le 1$*, Electrochim. Acta 45 (1999) 315–327.

[54] S. Mandal, R. M. Rojas, J. M. Amarilla, P. Calle, N. V. Kosova, V. F. Anufrienko, J. M. Rojo, *High Temperature Co-doped $LiMn_2O_4$-Based Spinels. Struc-*

tural, Electrical, and Electrochemical Characterization, Chem. Mater. 14 (2002) 1598–1605.

[55] Q. Zhong, *Synthesis and Electrochemistry of $LiNi_xMn_{2-x}O_4$*, J. Electrochem. Soc. 144 (1997) 205.

[56] Y. Ein-Eli, *$LiCu_x^{II}Cu_y^{III}Mn_{2-(x+y)}^{III,IV}O_4$: 5 V Cathode Materials*, J. Electrochem. Soc. 144(8) L205, 1997, 10.1149/1.1837857.

[57] Y. Ein-Eli, W. F. Howard, S. H. Lu, S. Mukerjee, J. McBreen, J. T. Vaughey, M. M. Thackeray, *$LiMn_{2-x}Cu_xO_4$ Spinels ($0.1 \leqslant x \leqslant 0.5$): A new Class of 5 V Cathode Materials for Li Batteries: I. Electrochemical, Structural, and Spectroscopic Studies*, Journal of The Electrochemical Society 145 (1998) 1238–1244.

[58] Y. Ein-Eli, W. Wen, S. Mukerjee, *Unexpected 5 V Behavior of Zn-Doped Mn Spinel Cathode Material*, Electrochemical and Solid-State Letters 8 (2005) A141-A144.

[59] W. Wen, B. Kumarasamy, S. Mukerjee, M. Auinat, Y. Ein-Eli, *Origin of 5 V Electrochemical Activity Observed in Non-Redox Reactive Divalent Cation Doped $LiM_{0.5-x}Mn_{1.5+x}O_4$ ($0 \leqslant x \leqslant 0.5$) Cathode Materials: In Situ XRD and XANES Spectroscopy Studies*, Journal of The Electrochemical Society 152 (2005) A1902-A1911.

[60] R. Thirunakaran, N. Kalaiselvi, P. Periasamy, B. R. Babu, N. G. Renganathan, N. Muniyandi, M. Raghavan, *Significance of Mg doped $LiMn_2O_4$ spinels as attractive 4 V cathode materials for use in lithium batteries*, Ionics 7 (2001) 187–191.

[61] J. H. Lee, J. K. Hong, D. H. Jang, Y.-K. Sun, S. M. Oh, *Degradation mechanisms in doped spinels of $LiM_{0.05}Mn_{1.95}O_4$ (M=Li, B, Al, Co, and Ni) for Li secondary batteries*, Journal of Power Sources 89 (2000) 7–14.

[62] Y. Shao-Horn, R. L. Middaugh, *Redox reactions of cobalt, aluminum and titanium substituted lithium manganese spinel compounds in lithium cells*, Solid State Ionics 139 (2001) 13–25.

[63] C. Sigala, A. Verbaere, J. L. Mansot, D. Guyomard, Y. Piffard, M. Tournoux, *The Cr-Substituted Spinel Mn Oxides $LiCr_yMn_{2-y}O_4$($0 \leq y \leq 1$): Rietveld Analysis of*

the Structure Modifications Induced by the Electrochemical Lithium Deintercalation, Journal of Solid State Chemistry 132 (1997) 372–381.

[64] T. Ohzuku, K. Ariyoshi, S. Takeda, Y. Sakai, *Synthesis and characterization of 5 V insertion material of $Li[Fe_yMn_{2-y}]O_4$ for lithium-ion batteries*, Electrochim. Acta 46 (2001) 2327–2336.

[65] H. Kawai, M. Nagata, M. Tabuchi, H. Tukamoto, A. R. West, *Novel 5 V Spinel Cathode $Li_2FeMn_3O_8$ for Lithium Ion Batteries*, Chem. Mater. 10 (1998) 3266–3268.

[66] H. Shigemura, H. Sakaebe, H. Kageyama, H. Kobayashi, A. R. West, R. Kanno, S. Morimoto et al., *Structure and Electrochemical Properties of $LiFe_xMn_{2-x}O_4$ $(0 \leqslant x \leqslant 0.5)$ Spinel as 5 V Electrode Material for Lithium Batteries*, Journal of The Electrochemical Society 148 (2001) A730-A736.

[67] H. Kawai, M. Nagata, H. Tukamoto, A. R. West, *A novel cathode $Li_2CoMn_3O_8$ for lithium ion batteries operating over 5 volts*, J. Mater. Chem. 8 (1998) 837–839.

[68] H. Kawai, M. Nagata, H. Tukamoto, A. R. Westa, *A New Lithium Cathode $LiCoMnO_4$: Toward Practical 5 V Lithium Batteries*, Electrochemical and Solid-State Letters 1 (1998) 212–214.

[69] H.-J. Kim, B.-S. Jin, C.-H. Doh, D.-S. Bae, H.-S. Kim, *Improved electrochemical performance of doped-$LiNi_{0.5}Mn_{1.5}O_4$ cathode material for lithium-ion batteries*, Electron. Mater. Lett. 9 (2013) 851–854.

[70] C. Luo, M. Martin, *Stability and defect structure of spinels $Li_{1+x}Mn_{2-x}O_{4-\delta}$*, Journal of Materials Science 42 (2007) 1955–1964.

[71] A. Manthiram, K. Chemelewski, E.-S. Lee, *A perspective on the high-voltage $LiMn_{1.5}Ni_{0.5}O_4$ spinel cathode for lithium-ion batteries*, Energy Environ. Sci. 7 (2014) 1339–1350.

[72] A. V. Potapenko, S. A. Kirillov, *Lithium manganese spinel materials for high-rate electrochemical applications*, Journal of Energy Chemistry 23 (2014) 543–558.

[73] S. Tan, Y. J. Ji, Z. R. Zhang, Y. Yang, *Recent Progress in Research on High-Voltage Electrolytes for Lithium-Ion Batteries*, ChemPhysChem 15 (2014) 1956–1969.

[74] D. Liu, W. Zhu, J. Trottier, C. Gagnon, F. Barray, A. Guerfi, A. Mauger et al., *Spinel materials for high-voltage cathodes in Li-ion batteries*, RSC Adv 4 (2014) 154–167.

[75] Y. Gao, K. Myrtle, M. Zhang, J. Reimers, J. Dahn, *Valence band of $LiNi_xMn_{2-x}O_4$ and its effects on the voltage profiles of $LiNi_xMn_{2-x}O_4$/Li electrochemical cells*, Phys. Rev. B 54 (1996) 16670–16675.

[76] R. Santhanam, B. Rambabu, *Research progress in high voltage spinel $LiNi_{0.5}Mn_{1.5}O_4$ material*, J. Power Sources 195 (2010) 5442–5451.

[77] H. Kawai, *A New Lithium Cathode $LiCoMnO_4$: Toward Practical 5 V Lithium Batteries*, Electrochem. Solid-State Lett. 1 (1999) 212.

[78] A. Hasegawa, K. Yoshizawa, T. Yamabe, *Crystal Orbital Overlap Population Analysis of the Capacity Fading of Metal-Substituted Spinel Lithium Manganate $LiMn_2O_4$*, J. Electrochem. Soc. 147 (2000) 4052.

[79] R. Hoffmann, *Solids and surfaces: A chemist's view of bonding in extended structures*, Wiley-VCH, New York, NY [u.a.], 1999.

[80] G.-Q. Liu, L. Wen, Y.-M. Liu, *Spinel $LiNi_{0.5}Mn_{1.5}O_4$ and its derivatives as cathodes for high-voltage Li-ion batteries*, J. Solid State Electrochem. 14 (2010) 2191–2202.

[81] J.-H. Kim, S.-T. Myung, C. S. Yoon, S. G. Kang, Y.-K. Sun, *Comparative Study of $LiNi_{0.5}Mn_{1.5}O_{4-\delta}$ and $LiNi_{0.5}Mn_{1.5}O_4$ Cathodes Having Two Crystallo-graphic Structures: Fd-3m and $P4_332$*, Chem. Mater. 16 (2004) 906–914.

[82] D. Pasero, N. Reeves, V. Pralong, A. R. West, *Oxygen Nonstoichiometry and Phase Transitions in $LiMn_{1.5}Ni_{0.5}O_{4-\delta}$*, J. Electrochem. Soc. 155 (2008) A282.

[83] M. Lin, L. Ben, Y. Sun, H. Wang, Z. Yang, L. Gu, X. Yu et al., *Insight into the Atomic Structure of High-Voltage Spinel $LiNi_{0.5}Mn_{1.5}O_4$ Cathode Material in the First Cycle*, Chem. Mater. 27 (2015) 292–303.

[84] T.-F. Yi, Y. Xie, M.-F. Ye, L.-J. Jiang, R.-S. Zhu, Y.-R. Zhu, *Recent developments in the doping of $LiNi_{0.5}Mn_{1.5}O_4$ cathode material for 5 V lithium-ion batteries*, Ionics 17 (2011) 383–389.

[85] H. Wang, T. A. Tan, P. Yang, O. M. Lai, L. Lu, *High-Rate Performances of the Ru-Doped Spinel $LiNi_{0.5}Mn_{1.5}O_4$: Effects on Doping and Particle Size*, J. Phys. Chem. C. 13 (2011) 6102-6110.

[86] N. M. Hagh, G. G. Amatucci, *Effect of cation and anion doping on microstructure and electrochemical properties of the $LiMn_{1.5}Ni_{0.5}O_{4-\delta}$ spinel*, J. Power Sources 256 (2014) 457–469.

[87] G. G. Amatucci, N. Pereira, T. Zheng, J.-M. Tarascon, *Failure Mechanism and Improvement of the Elevated Temperature Cycling of $LiMn_2O_4$ Compounds Through the Use of the $LiAl_xMn_{2-x}O_{4-z}F_z$ Solid Solution*, Journal of The Electrochemical Society 148 (2001) A171-A182.

[88] W. Choi, A. Manthiram, *Superior Capacity Retention Spinel Oxyfluoride Cathodes for Lithium-Ion Batteries*, Electrochem. Solid State Lett. 9 (2006) A245-A248.

[89] H. Li, Y. Luo, J. Xie, Q. Zhang, L. Yan, *Effect of lithium and fluorine doping on the electrochemical and thermal stability of $LiNi_{0.5}Mn_{1.5}O_4$ spinel cathode material*, J. Alloy. Compd. 639 (2015) 346–351.

[90] A. Höweling, D. Stenzel, H. Gesswein, M. Kaus, S. Indris, T. Bergfeldt, J. R. Binder, *Variations in structure and electrochemistry of iron- and titanium-doped lithium nickel manganese oxyfluoride spinels*, J. Power Sources 315 (2016) 269–276.

[91] G. Du, Y. NuLi, J. Yang, J. Wang, *Fluorine-doped LiNi0.5Mn1.5O4 for 5V cathode materials of lithium-ion battery*, Mat. Res. Bull. 43 (2008) 3607–3613.

[92] T. Okumura, T. Fukutsuka, K. Matsumoto, Y. Orikasa, H. Arai, Z. Ogumi, Y. Uchimoto, *Role of Local and Electronic Structural Changes with Partially Anion substitution Lithium Manganese Spinel Oxides on Their Electrochemical Properties: X-ray Absorption Spectroscopy Study*, Dalton Trans 40 (2011) 9752–9764.

[93] A. Gutierrez, A. Manthiram, *Understanding the Effects of Cationic and Anionic Substitutions in Spinel Cathodes of Lithium-Ion Batteries*, J. Electrochem. Soc. 160 (2013) A901-A905.

[94] K. Matsumoto, T. Fukutsuka, T. Okumura, Y. Uchimoto, K. Amezawa, M. Inaba, A. Tasaka, *Electronic structures of partially fluorinated lithium manganese spinel oxides and their electrochemical properties*, Selected Papers presented at the 14th INTERNATIONAL MEETING ON LITHIUM BATTERIES (IMLB-2008) 189 (2009) 599–601.

[95] Q. Luo, A. Manthiram, *Effect of Low-Temperature Fluorine Doping on the Properties of Spinel $LiMn_{2-2y}Li_yM_yO_{4-\eta}F_\eta$ (M = Fe Co, and Zn) Cathodes*, Journal of The Electrochemical Society 156 (2009) A84-A88.

[96] Q. Luo, T. Muraliganth, A. Manthiram, *On the incorporation of fluorine into the manganese spinel cathode lattice*, Solid State Ion. 180 (2009) 703–707.

[97] S.-W. Oh, S.-H. Park, J.-H. Kim, Y. C. Bae, Y.-K. Sun, *Improvement of electrochemical properties of $LiNi_{0.5}Mn_{1.5}O_4$ spinel material by fluorine substitution*, J. Power Sources 157 (2006) 464–470.

[98] A. Eftekhari, *Electrochemical performance and cyclability of $LiFe_{0.5}Mn_{1.5}O_4$ as a 5 V cathode material for lithium batteries*, Journal of Power Sources 124 (2003) 182–190.

[99] T. Ohzuku, R.J. Brodd, *An overview of positive-electrode materials for advanced lithium-ion batteries*, J. Power Sources 174 (2007) 449–456.

[100] N. Reeves-McLaren, J. Sharp, H. Beltran-Mir, W. M. Rainforth, A. R. West, *Spinel-rock salt transformation in $LiCoMnO_{4-d}$*, Proc. R. Soc. A 472 (2016) 20140991.

[101] E. Zhecheva, R. Stoyanova, R. Alcántara, P. Lavela, J.L. Tirado, *EPR studies of Li deintercalation from $LiCoMnO_4$ spinel-type electrode active material*, J. Power Sources 159 (2006) 1389–1394.

[102] M. Hu, Y. Tian, J. Wei, D. Wang, Z. Zhou, *Porous hollow $LiCoMnO_4$ microspheres as cathode materials for 5 V lithium ion batteries,* J. Power Sources 247 (2014) 794–798.

[103] D. M. Cupid, A. Reif, H. J. Seifert, *Enthalpy of formation of $Li_{1+x}Mn_{2-x}O_4$ (0 < x < 0.1) spinel phases*, Thermochim. Acta 599 (2015) 35–41.

[104] J. M. Amarilla, R. M. Rojas, F. Pico, L. Pascual, K. Petrov, D. Kovacheva, M.G. Lazarraga et al., *Nanosized $LiM_YMn_{2-Y}O_4$ (M = Cr, Co and Ni) spinels synthesized by a sucrose-aided combustion method: Structural characterization and electrochemical properties*, 13th International Meeting on Lithium Batteries 174 (2007) 1212–1217.

[105] M. Hu, Y. Tian, L. Su, J. Wei, Z. Zhou, *Preparation and Ni-Doping Effect of Nanosized Truncated Octahedral $LiCoMnO_4$ As Cathode Materials for 5 V Li-Ion Batteries*, ACS Appl. Mater. Interfaces 5 (2013) 12185–12189.

[106] R. Alcantara, M. Jaraba, P. Lavela, J. L. Tirado, *Electrochemical, ^{6}Li MAS NMR, and X-ray and Neutron Diffraction Study of $LiCo_xFe_yMn2-(x+y)O_4$ Spinel Oxides for High-Voltage Cathode Materials*, Chem. Mater. 15 (2003) 1210–1216.

[107] C.-L. Tsai, E. Dashjav, E.-M. Hammer, M. Finsterbusch, F. Tietz, S. Uhlenbruck, H. P. Buchkremer, *High conductivity of mixed phase Al-substituted $Li_7La_3Zr_2O_{12}$*, J. Electroceram. 35 (2015) 25–32.

[108] A. Eftekhari, *Fabrication of 5 V lithium rechargeable micro-battery*, Journal of Power Sources 132 (2004) 240–243.

[109] S. Uhlenbruck, J. Dornseiffer, S. Lobe, C. Dellen, C.-L. Tsai, B. Gotzen, D. Sebold et al., *Cathode-electrolyte material interactions during manufacturing of inorganic solid-state lithium batteries*, J. Electroceram. (2016) 1–10.

[110] J. Li, C. Ma, M. Chi, C. Liang, N. J. Dudney, *Solid Electrolyte: the Key for High-Voltage Lithium Batteries*, Adv. Energy Mater. 5 (2015).

[111] T. Placke, R. Kloepsch, S. Dühnen, M. Winter, *Lithium ion, lithium metal, and alternative rechargeable battery technologies: the odyssey for high energy density*, Journal of Solid State Electrochemistry 21 (2017) 1939–1964.

[112] A. Mauger, M. Armand, C.M. Julien, K. Zaghib, *Challenges and issues facing lithium metal for solid-state rechargeable batteries*, Journal of Power Sources 353 (2017) 333–342.

[113] S. Lobe, C. Dellen, M. Finsterbusch, H.-G. Gehrke, D. Sebold, C.-L. Tsai, S. Uhlenbruck, et al., *Radio frequency magnetron sputtering of $Li_7La_3Zr_2O_{12}$ thin films for solid-state batteries*, Journal of Power Sources 307 (2016) 684–689.

[114] X. Yu, J. B Bates, G. E. Jellison, F. X. Hart, *A Stable Thin-Film Lithium Electrolyte: Lithium Phosphorus Oxynitride*, Journal of The Electrochemical Society 144 (1997) 524–532.

[115] M. Kotobuki, H. Munakata, K. Kanamura, Y. Sato, T. Yoshida, *Compatibility of $Li_7La_3Zr_2O_{12}$ Solid Electrolyte to All-Solid-State Battery Using Li Metal Anode*, Journal of The Electrochemical Society 157 (2010) A1076-A1079.

[116] T. Thompson, S. Yu, L. Williams, R. D. Schmidt, R. Garcia-Mendez, J. Wolfenstine, J. L. Allen, et al., *Electrochemical Window of the Li-Ion Solid Electrolyte $Li_7La_3Zr_2O_{12}$*, ACS Energy Lett 2 (2017) 462–468.

[117] H. Li, W. C. West, M. Motoyama, Y. Iriyama, *Deep-discharged $LiCoMnO_4$ Lithium-Ion cathodes with high rate capability and long cycle life*, Thin Solid Films 615 (2016) 210–214.

[118] N. Kuwata, S. Kudo, Y. Matsuda, J. Kawamura, *Fabrication of thin-film lithium batteries with 5-V-class $LiCoMnO_4$ cathodes*, Solid State Ion. 262 (2014) 165–169.

[119] P. M. Pechini, *Method of preparing lead and alkaline earth titanates and niobates and coating method using the same to form a capacitor*, Google Patents, 1967.

[120] A. M. Huízar-Félix, T. Hernández, S. de la Parra, J. Ibarra, B. Kharisov, *Sol–gel based Pechini method synthesis and characterization of $Sm_{1-x}Ca_xFeO_3$ perovskite $0.1 \leq x \leq 0.5$*, Powder Technology 229 (2012) 290–293.

[121] M. Kakihana, M. Yoshimura, *Synthesis and Characteristics of Complex Multicomponent Oxides Prepared by Polymer Complex Method*, Bulletin of the Chemical Society of Japan 72 (1999) 1427–1443.

[122] F. V. Motta, A. P. A. Marques, C. A. Paskocimas, M. R. D. Bomio, A. S. F. Santos, et al., *Synthesis of $Ba_{1-x}Ca_xTiO_3$ by Complex Polymerization Method (CPM)*, A. de Souza Gomes (Ed.), Polymerization, InTech, 2012.

[123] Bruker AXS, Topas V4: *General profile and structure analysis software for powder diffraction data*, Karlsruhe, Germany.

[124] W. A. Ranken, T. W. Bonner, J. H. McCrary, *Energy Dependence of F^{19}+p Reactions*, Phys. Rev. 109 (1958) 1646–1651.

[125] M. Mayer, *SIMNRA, a simulation program for the analysis of NRA, RBS and ERDA*, 2016.

[126] A. C. Larson and R. B. Von Dreele, *General Structure Analysis System (GSAS)*, Los Alamos National Laboratory Report LAUR 86-748, 1994.

[127] B. H. Toby, *EXPGUI, a graphical user interface for GSAS*, J. Appl. Cryst. (2001). 34, 210-213.

[128] A. Boulineau, L. Croguennec, C. Delmas, F. Weill, *Reinvestigation of Li_2MnO_3 Structure*, Chem. Mater. 21 (2009) 4216–4222.

[129] V. K. Pecharsky, P. Y. Zavalij, *Fundamentals of powder diffraction and structural characterization of materials*, Boston, MA, Springer, 2005.

[130] V. F. Sears, *Neutron scattering lengths and cross sections*, Neutron News 3 (1992) 26–37.

[131] C. M. Julien, M. Massot, *Lattice vibrations of materials for lithium rechargeable batteries I. Lithium manganese oxide spinel*, J. Mater. Sci. Eng. B 97 (2003) 217–230.

[132] R. D. Shannon, *Revised effective ionic radii and systematic studies of interatomic distances in halides and chalcogenides*, Acta Crystallogr., Sect. A 32 (1976) 751–767.

[133] C. M. Julien, F. Gendron, A. Amdouni, M. Massot, *Lattice vibrations of materials for lithium rechargeable batteries. VI: Ordered spinels*, J. Mater. Sci. Eng. B 130 (2006) 41–48.

[134] C. M. Julien, M. Massot, *Lattice vibrations of materials for lithium rechargeable batteries III. Lithium manganese oxides*, J. Mater. Sci. Eng. B 100 (2003) 69–78.

[135] J. M. Tarascon, E. Wang, F. K. Shokoohi, W. R. McKinnon, S. Colson, *The Spinel Phase of $LiMn_2O_4$ as a Cathode in Secondary Lithium Cells*, Journal of The Electrochemical Society 138 (1991) 2859–2864.

[136] R. Alcántara, M. Jaraba, P. Lavela, J. L. Tirado, *New $LiNi_yCo_{1-2y}Mn_{1+y}O_4$ Spinel Oxide Solid Solutions as 5 V Electrode Material for Li - Ion Batteries*, J. Electrochem. Soc. 151 (2004) A53-A58.

[137] Y. Gao, J. Reimers, J. Dahn, *Changes in the voltage profile of $Li/Li_{1+x}Mn_{2-x}O_4$ cells as a function of x*, Phys. Rev. B 54 (1996) 3878–3883.

[138] Y. Wang, W. Lai, *Phase transition in lithium garnet oxide ionic conductors $Li_7La_3Zr_2O_{12}$: The role of Ta substitution and H_2O/CO_2 exposure*, Journal of Power Sources 275 (2015) 612–620.

[139] M. Du Rubat Merac, I. E. Reimanis, H.-J. Kleebe, *Electrochemical Impedance Spectroscopy of Transparent Polycrystalline Magnesium Aluminate ($MgAl_2O_4$) Spinel*, J. Am. Ceram. Soc. 98 (2015) 2130–2138.

[140] I. E. Reimanis, H.-J. Kleebe, *Reactions in the sintering of $MgAl_2O_4$ spinel doped with LiF*, IJMR 98 (2007) 1273–1278.

[141] C.-L. Tsai, M. Kopczyk, R. J. Smith, V. H. Schmidt, *Low temperature sintering of $Ba(Zr_{0.8-x}Ce_xY_{0.2})O_{3-\delta}$ using lithium fluoride additive*, Solid State Ionics 181 (2010) 1083–1090.

[142] Z.-Y. Tian, N. Bahlawane, V. Vannier, K. Kohse-Höinghaus, *Structure sensitivity of propene oxidation over Co-Mn spinels*, Proceedings of the Combustion Institute 34 (2013) 2261–2268.

[143] J. Lee, H. Zhu, G. G. Yadav, J. Caruthers, Y. Wu, *Porous ternary complex metal oxide nanoparticles converted from core/shell nanoparticles*, Nano Res. 9 (2016) 996–1004.

[144] N. Padmanathan, S. Selladurai, *Mesoporous $MnCo_2O_4$ spinel oxide nanostructure synthesized by solvothermal technique for supercapacitor*, Ionics 20 (2014) 479–487.

[145] P. Zanello, *Voltammetric techniques*, in: *Inorganic Electrochemistry: Theory, Practice and Application*, The Royal Society of Chemistry, 2003, pp. 49–136.

[146] J. Bréger, M. Jiang, N. Dupré, Y. S. Meng, Y. Shao-Horn, G. Ceder, C. P. Grey, *High-resolution X-ray diffraction, DIFFaX, NMR and first principles study of disorder in the Li_2MnO_3–$Li[Ni_{1/2}Mn_{1/2}]O_2$ solid solution*, J. Solid State Chem. 178 (2005) 2575–2585.

[147] B. E. Warren, B. L. Averbach, *The Separation of Stacking Fault Broadening in Cold-Worked Metals*, J. Appl. Phys. 23 (1952) 1059.

[148] K. Dokko, N. Anzue, M. Mohamedi, T. Itoh, I. Uchida, *Raman spectro-electrochemistry of $LiCo_xMn_{2-x}O_4$ thin film electrodes for 5 V lithium batteries*, Electrochem. Commun. 6 (2004) 384–388.

[149] V. G. Hadjiev, M. N. Iliev, I. V. Vergilov, *The Raman spectra of Co_3O_4*, J. Phys. C: Solid State Phys. 21 (1988) L199.

[150] N. Amdouni, K. Zaghib, F. Gendron, A. Mauger, C. M. Julien, *Structure and insertion properties of disordered and ordered $LiNi_{0.5}Mn_{1.5}O_4$ spinels prepared by wet chemistry*, Ionics 12 (2006) 117–126.

[151] J. Yang, X. Han, X. Zhang, F. Cheng, J. Chen, *Spinel $LiNi_{0.5}Mn_{1.5}O_4$ cathode for rechargeable lithium ion batteries: Nano vs micro, ordered phase ($P4_332$) vs disordered phase (Fd-3m)*, Nano Res. 6 (2013) 679–687.

[152] R. Yamaguchi, H. Ikuta, M. Wakihara, *Heat of Formation for $LiM_yMn_{2-y}O_4$ (M=Co, Cr, Li, Mg, Ni) Spinel Solid Solution*, Journal of Thermal Analysis and Calorimetry 57 797–806.

[153] J. L. Narváez-Semanate, A. Rodrigues, *Microstructure and ionic conductivity of $Li_{1+x}Al_xTi_{2-x}(PO_4)_3$ NASICON glass-ceramics*, Solid State Ionics 181 (2010) 1197–1204.

[154] L. Miara, A. Windmüller, C.-L. Tsai, W. D. Richards, Q. Ma, S. Uhlenbruck, O. Guillon et al., *About the Compatibility between High Voltage Spinel Cathode Materials and Solid Oxide Electrolytes as a Function of Temperature*, ACS Appl. Mater. Interfaces 8 (2016) 26842–26850.

[155] D. R. Lide, *CRC Handbook of Chemistry and Physics*, CRC Press, Taylor & Francis, Boca Raton, FL 2005, 2005-2006.

[156] W. Choi, A. Manthiram, *Factors Controlling the Fluorine Content and the Electrochemical Performance of Spinel Oxyfluoride Cathodes*, Journal of The Electrochemical Society 154 (2007) A792-A797.

[157] J. M. Paulsen, J. R. Dahn, *Phase Diagram of Li−Mn−O Spinel in Air*, Chem. Mater. 11 (1999) 3065–3079.

[158] P. Strobel, F. Le Cras, L. Seguin, M. Anne, J. M. Tarascon, *Oxygen Non-stoichiometry in Li–Mn–O Spinel Oxides: A Powder Neutron Diffraction Study*, J. Solid State Chem. 135 (1998) 132–139.

[159] L. Xiao, J. Xiao, X. Yu, P. Yan, J. Zheng, M. Engelhard, P. Bhattacharya et al., *Effects of structural defects on the electrochemical activation of Li_2MnO_3*, Nano Energy 16 (2015) 143–151.

[160] J. Rana, M. Stan, R. Kloepsch, J. Li, G. Schumacher, E. Welter, I. Zizak et al., *Structural Changes in Li_2MnO_3 Cathode Material for Li-Ion Batteries*, Adv. Energy Mater. 4 (2014) 1300998.

[161] A. V. Virkar, J. Chen, C. W. Tanner, J.-W. Kim, *The role of electrode micro-structure on activation and concentration polarizations in solid oxide fuel cells*, Solid State Ionics 131 (2000) 189–198.

Abstract

High voltage cathodes, based on $Li(M,Mn)_2O_4$ spinels with M = Ni, Fe or Co that operate at voltages around 5 V vs. Li/Li^+, were discovered already more than 25 years ago. Yet, their high potentials have never been fully accessible in state of the art lithium-ion batteries, due to the instability of the used liquid electrolyte. However, ceramic electrolytes that offer an enhanced electrochemical stability, might allow for the application of high voltage spinel cathodes eventually, if suitable solid-state batteries can be designed.

The first choice to design a solid-state high voltage battery would be based on a cathode composite, consisting of the cathode active material and a lithium-ion conductor, and a lithium metal anode. Anode and cathode would be separated by a thin solid electrolyte. The composite cathode would need to be designed in a way that the active material and the lithium-ion conductor are sintered to close contact and provide diffusion of lithium-ions through a closed network of solid electrolyte and electronic diffusion through a closed network of the cathode active material. This kind of design requires the sinterability and compatibility of the active material and the electrolyte material at the processing/sintering temperature.

In this dissertation, three high voltage spinels, namely $LiNi_{0.5}Mn_{1.5}O_4$, $LiFe_{0.5}Mn_{1.5}O_4$, and $LiCoMnO_4$ were synthesized, characterized and investigated regarding their chemical compatibility with the solid electrolytes $Li_{1.5}Al_{0.5}Ti_{1.5}(PO_4)_3$ and $Li_{6.6}La_3Zr_{1.6}Ta_{0.4}O_{12}$. The results show that a sufficient chemical compatibility is not given at processing/sintering temperatures above 600 °C and either alternative processing routes, different solid electrolytes or different cell designs would need to be invented to realize high voltage solid-state batteries with spinel cathodes.

To target a proof of concept for high voltage solid state batteries, a cathode supported solid-state battery setup can be chosen alternatively, with a cathode consisting of the active spinel material only. For sufficient lithium-ion and electronic conduction this cathode would need to be thin and dense but still thick enough to support a thin film solid electrolyte. This configuration requires the sinterability of the spinel material to high relative densities.

However, the densification of lithium manganese spinels is problematic due to their thermal instability at elevated temperatures. Therefore, one of the synthesized spinels was selected to be investigated regarding its sinterability and to find processing routes that lead to high relative densities by using lithium fluoride as sintering additive. For this, $LiCoMnO_4$, the spinel with the highest energy density, was chosen. It will be shown that $LiCoMnO_4$ can be successfully densified and processed to dense pellets (> 90 % relative density) at 900 °C by using 1 wt.-% lithium fluoride as a sintering additive.

Since the fluorine anion most likely is incorporated into the $LiCoMnO_4$ spinel during this process, the important question arises, how fluorine within the spinel structure would affect the properties of the cathode. To answer this question, $LiCoMnO_4$ powders substituted with 0, 0.5, and 1 mol fluorine per formula unit (equals 0, ~0.5, and ~1 wt.-% fluorine), synthesized by a classical solid-state reaction at 800 °C, were investigated. It was found that incorporated fluorine has a stabilizing effect on the spinel lattice and improves its thermodynamic phase stability and its cycling stability during the electrochemical cycling. Furthermore, the capacity of the fluorinated $LiCoMnO_4$ is enhanced as a result of a higher phase purity and a higher availability of lithium-sites.

From the study of the fluorinated $LiCoMnO_4$ powders it can be concluded, that fluorine incorporation into the spinel lattice will not bring any drawbacks for the performance of $LiCoMnO_4$ cathodes sintered with lithium fluoride. Therefore, the dense fluorinated $LiCoMnO_4$ pellets that are introduced in this dissertation are promising candidates for self-supported cathodes to build up a high voltage solid state battery.

Kurzfassung

Bereits vor mehr als 25 Jahren wurden Hochvolt-Kathoden, basierend auf $Li(M,Mn)_2O_4$ Spinellen mit M = Ni, Fe oder Co, die bei Spannungen von ungefähr 5 V vs. Li/Li^+ arbeiten, entdeckt. Ihre hohen Spannungen waren jedoch aufgrund der Instabilität des flüssigen Elektrolyten, der in den gängigen Lithium-Ionen-Batterien zum Einsatz kommt, niemals vollständig zugänglich. Heutzutage könnten jedoch Keramik-Elektrolyte, die eine verbesserte elektrochemische Stabilität bieten, die Anwendung von Hochvolt-Spinellkathoden ermöglichen, falls geeignete Festkörperbatterien entwickelt werden können.

Um erfolgreich eine Hochvolt-Festkörperbatterie zu entwerfen, fiele die erste Wahl auf einen Aufbau aus einem Kathodenverbund, der aus dem aktiven Kathodenmaterial und einem Li-ionen Leiter bestünde, und einer Lithiummetallanode. Anode und Kathode wären außerdem durch einen dünnen Festelektrolyten getrennt. Der Kathodenverbundwerkstoff wäre idealerweise so aufgebaut, dass das Aktivmaterial und der Li-ionen Leiter zu einem dichten Verbund gesintert wären und darüber hinaus die Diffusion von Li-Ionen, durch ein geschlossenes Netzwerk des Li-ionen Leiters, und elektronische Diffusion, durch ein geschlossenes Netzwerk des aktiven Kathodenmaterials, ermöglichen würde. Dieses Konzept erfordert jedoch die Kompatibilität des aktiven Materials und des Li-ionen Leiters / Elektrolytmaterials bei der Verarbeitungs-/Sintertemperatur.

In dieser Dissertation wurden drei Hochvoltspinelle, nämlich $LiNi_{0.5}Mn_{1.5}O_4$, $LiFe_{0.5}Mn_{1.5}O_4$, und $LiCoMnO_4$ synthetisiert, charakterisiert und hinsichtlich ihrer chemischen Kompatibilität zu den Festkörperelektrolyten $Li_{1.5}Al_{0.5}Ti_{1.5}(PO_4)_3$ und $Li_{6.6}La_3Zr_{1.6}Ta_{0.4}O_{12}$ untersucht. Die Ergebnisse zeigen, dass bei Verarbeitungs-/Sintertemperaturen oberhalb von 600 °C keine ausreichende chemische Kompatibilität gegeben ist und entweder alternative Verarbeitungswege, unterschiedliche Festelektrolyte oder andere Zellkonzepte erfunden werden müssten, um Hochvolt-Festkörperbatterien zu realisieren.

Um einen konzeptionellen Beweis für die Funktionsfähigkeit von Hochvolt-Festkörperbatterien zu erzielen, bietet sich alternativ an, eine kathodengestützte Festkörperbatterie zu entwickeln, die keinen Kathodenverbundwerkstoff enthält. Anstelle des Kathodenverbundwerkstoffes bestünde die Kathode nur aus dem Ak-

tivmaterial. Um ausreichende ionische und elektronische Leitfähigkeiten zu erzielen, sollte diese Kathode zudem möglichst dünn und möglichst dicht sein – aber dick genug, um einen Dünnschichtelektrolyten zu stützen. Dieser Aufbau erfordert die Sinterfähigkeit des Aktivmaterials zu hohen relativen Dichten.

Da die Verdichtung von Lithium-Mangan Spinellen aufgrund ihrer thermischen Instabilität bei erhöhten Temperaturen problematisch ist, wird in dieser Dissertation die Sinterfähigkeit von einem der synthetisierten Spinelle untersucht und Verarbeitungswege die zu hohen relativen Dichten führen erforscht, indem Lithium-Fluorid als Sinteradditiv hinzugesetzt wird. Dafür wurde $LiCoMnO_4$, der Spinell mit der höchsten Energiedichte, ausgewählt. Es wird gezeigt, dass $LiCoMnO_4$, mit Hilfe von 1 gew.-% Lithiumfluorid als Sinteradditiv, erfolgreich zu dichten Pellets (> 90% relative Dichte) bei 900 °C verarbeitet werden kann.

Da das Fluoranion aus dem Lithiumfluorid-Additiv während dieses Vorgangs höchstwahrscheinlich in den Spinell eingebaut wird, ergibt sich die wichtige Frage, in wie weit in der Spinellstruktur enthaltenes Fluor die Eigenschaften der Kathode beeinflussen würde. Um diese Frage zu beantworten, werden $LiCoMnO_4$-Pulver, die mit 0, 0,5 und 1 mol Fluor pro Formeleinheit substituiert wurden (entsprich 0, 0,5 und 1 gew.-% Fluor), und mittels klassischer Festkörperreaktion bei 800 °C synthetisiert wurden, untersucht. Es kann gezeigt werden, dass eingebaute Fluoranionen stabilisierend auf das Spinellgitter wirken und so die thermodynamische Phasenstabilität und die Zyklenstabilität des Spinells während des elektrochemischen Zyklierens verbessern. Darüber hinaus ist die Kapazität der fluorierten $LiCoMnO_4$ Proben aufgrund einer höheren Phasenreinheit und einer höheren Verfügbarkeit von Lithium-Gitterpositionen erhöht.

Aus der Untersuchung der fluorierten $LiCoMnO_4$-Pulver kann geschlossen werden, dass der Einbau des Fluoranions in das Spinellgitter keine Nachteile für die Eigenschaften der mit Lithiumfluorid gesinterten $LiCoMnO_4$-Kathoden mit sich bringt. Daher sind die dichten fluorierten $LiCoMnO_4$-Pellets, die in dieser Dissertation vorgestellt werden, vielversprechende Kandidaten für selbsttragende Kathoden, um eine Hochvoltfestkörperbatterie aufzubauen.

Band / Volume 445
Cathode Stability and Processing in Inert Substrate-Supported Solid Oxide Fuel Cells
E. Matte (2018), viii, 178 pp
ISBN: 978-3-95806-373-0

Band / Volume 446
Aging and Degradation Behavior of Electrode Materials in Solid Oxide Fuel Cells (SOFCs)
X. Yin (2018), x, 103 pp
ISBN: 978-3-95806-374-7

Band / Volume 447
TRENDS 2017
Transition to Renewable Energy Devices and Systems
D. Stolten, R. Peters (Eds.) (2018), 206 pp
ISBN: 978-3-95806-376-1

Band / Volume 448
3D simulation of impurity transport in a fusion edge plasma using a massively parallel Monte-Carlo code
J. Romazanov (2018), xvi, 149 pp
ISBN: 978-3-95806-377-8

Band / Volume 449
Projektbericht Adelheid – aus dem Labor heraus in die Lüfte
R. Peters, J. Pasel, R. C. Samsun, A. Tschauder, C. Wiethege, F. Scharf, D. Stolten (2018), xxi, 321 pp
ISBN: 978-3-95806-378-5

Band / Volume 450
Microstructure and Thermomechanical Properties of $SrTi_{1-x}Fe_xO_{3-\delta}$ Oxygen Transport Membranes and Supports
R. Oliveira Silva (2019), vi, 148 pp
ISBN: 978-3-95806-381-5

Band / Volume 451
Sodium Ion Conducting Ceramics for Sodium Ion Batteries
S. Naqash (2019), vii, 134 pp
ISBN: 978-3-95806-382-2

Band / Volume 452
Quantitative Analyse der Trocknungsverläufe von Katalysatordispersionen
F. Scheepers (2019), VIII, 191 pp
ISBN: 978-3-95806-384-6

Band / Volume 453
Neue Optionen für einen wirtschaftlichen Betrieb von Wasserstoffzügen durch Nutzung der LOHC-Technologie?
P. Wasserscheid, T. Grube, D. Sternfeld, M. Essl, M. Robinius, D. Stolten
(2019), II, 88 pp
ISBN: 978-3-95806-386-0

Band / Volume 454
Reformierung von BtL-Kraftstoffen für die HT-PEFC in luftfahrttechnischen Systemen
C. Wilbrand (2019), IV, 312 pp
ISBN: 978-3-95806-387-7

Band / Volume 455
Entwicklung von thermischen Spritzprozessen für fortschrittliche Schutz- und Funktionsschichten
G. Mauer (2019), vi, 57 pp
ISBN: 978-3-95806-388-4

Band / Volume 456
Columnar Structured Thermal Barrier Coatings Deposited by Axial Suspension Plasma Spraying
D. Zhou (2019), VI, 126 pp
ISBN: 978-3-95806-391-4

Band / Volume 457
Modellierung zeitlich aufgelöster Ladeenergienachfragen von batterie-elektrischen Fahrzeugen und deren Abbildung in einem Energiesystemmodell
J. F. Linßen (2019), VIII, 189 pp
ISBN: 978-3-95806-395-2

Band / Volume 458
Synthesis and Analysis of Spinel Cathode Materials for High Voltage Solid-State Lithium Batteries
A. Windmüller (2019), iv, 141 pp
ISBN: 978-3-95806-396-9

Energie & Umwelt / Energy & Environment
Band / Volume 458
ISBN 978-3-95806-396-9

Mitglied der Helmholtz-Gemeinschaft

JÜLICH
Forschungszentrum